Understanding Divalent Cation Intercalation in Manganese Oxides

BY

GENE NOLIS
B.S., Binghamton University, 2012
M.S., Université de Picardie Jules Verne, 2014

THESIS

Submitted as partial fulfillment of the requirements for the degree of Doctor of Philosophy in Chemistry
in the Graduate College of the University of Illinois at Chicago, 2019

Chicago, Illinois

Defense Committee:
Professor Jordi Cabana, Chair and Advisor
Professor Donald Wink
Professor Neal Mankad
Professor Nan Jiang
Professor George Crabtree, physics department

ACKNOWLEDGEMENTS

CONTRIBUTION OF AUTHORS

This report could not have been completed without the support of expert advisors and motivated students. During my time at the University of Illinois at Chicago, I had the pleasure of mentoring three undergraduate research assistants, Abdullah Adil, Lisa Berkland and Jannie Bolotnikov. Adil and Berkland assisted with electrochemical and X-ray diffraction measurements in chapter 3. Bolotnikov assisted with colloidal synthesis of manganese oxide compounds in chapters 4 and 5, as well as counting individual nanocrystals to make histograms of particle size distribution. Additionally, Bolotnikov assisted in X-ray diffraction measurements in chapters 4 – 6 and electrochemical characterization in chapters 5 and 6. Hyun Deog Yoo provided expert advice on how to setup electrochemical measurements performed in chapters 3, 5, and 6. Linhua Hu and Patrick Phillips assisted with electron microscope images and energy dispersive spectroscopy measurements discussed in chapter 3. Saul Lapidus was the expert advisor on synchrotron X-ray diffraction studies. John Freeland was the expert advisor for soft X-ray diffraction studies. Robert Klie was the expert advisor on electron microscopy studies.

LIST OF TABLES

LIST OF FIGURES

LIST OF FIGURES CONTINUED

LIST OF ABBREVIATIONS

E Potential

PXRD Powder X-ray diffraction

SXRD Synchrotron X-ray diffraction

TEM Transmission electron microscopy

STEM Scanning transmission electron microscopy

EDX Energy dispersive X-ray spectroscopy

XAS X-ray absorption micropcy

TGA Thermogravimetric analysis

DSC Differential scanning calorimetry

TEY Total electron yield

TFY Total fluorescence yield

OAc Acetate

Acac Acetylacetonate

TFSI (bis(trifluoro-methane-sulfonyl)imide)

PYR14 1-Butyl-1-methylpyrrolidinium

LB Large batch

SB Small batch

LMO $LiMn_2O_4$

NMO $NaMn_2O_4$

LMO-iX Cation exchanged $LiMn_2O_4$

TMNO·2H$_2$O Trimethylamine N-oxide dihydrate

SUMMARY

The desire to improve the energy density of rechargeable batteries requires the discovery of different battery chemistries. One such class of batteries could use magnesium, calcium, or zinc metal counter electrodes paired with a transition metal oxide working electrode to achieve higher energy densities than lithium ion ones. However, divalent cations of these metals have sluggish kinetics of mobility in solids. Manganese oxides with the spinel and post-spinel crystal structures are predicted to have low energy barriers of divalent cation mobility. Additionally, shortened pathways are expected to improve ion transport in crystalline solids. So, in addition to structural effects, nanoscale electrode materials are predicted to overcome these barriers as well.

This work describes the synthesis of nanoscale spinel and microscale post-spinel manganese oxides, using colloidal and high-pressure methods, respectively. The electrochemical performance of these materials was assessed in nonaqueous electrolyte in order to determine their potential for use in magnesium batteries. Lastly, the electrochemical properties of micrometric spinel Mn_2O_4 under reductive conditions in aqueous calcium and zinc electrolytes were studied and reported.

1 INTRODUCTION

1.1 INTRODUCTION

Lithium-ion (Li-ion) batteries currently dominate the market of power sources for mobile devices; and they are currently being pursued at larger scales, such as in automotive and grid energy applications. However, while mass-produced, the charge storage capacities of these battery technologies are intrinsically limited by the fact that the transfer of monovalent Li^+ involves only one electron per site of working electrode materials.[1] Thus, new energy storage systems and materials that overcome this limitation are still vigorously being researched to meet these emerging demands in scalability.

1.2 BASICS OF RECHARGEABLE BATTERIES

Batteries convert chemical energy directly to electrical energy to power electrical devices such as flashlights and pacemakers. Batteries are composed of one or several electrochemical cells connected in series, where the potentials of the individual cells add to give the total voltage.[1] Each electrochemical cell is composed of a negative electrode (conventionally referred to as anode), a positive electrode (cathode), and an electrolyte. A schematic diagram of a typical lithium-ion battery is shown in figure 1. In this diagram the cell is composed of a solid anode (graphite), a solid cathode ($LiMn_2O_4$), and a liquid electrolyte (a mixture of 1 M $LiPF_6$ in a mixture of 1:1 ethylene carbonate and dimethyl carbonate).
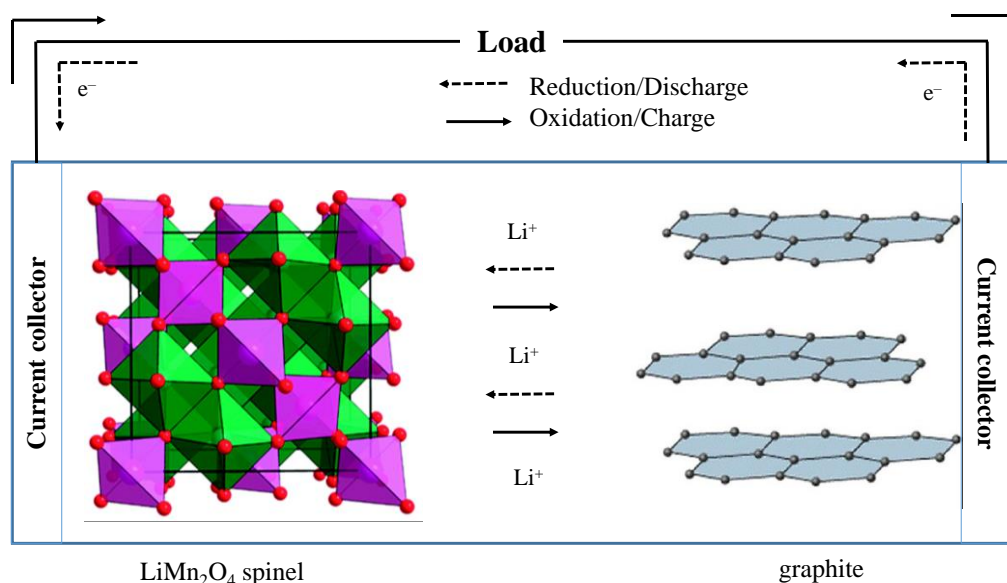
Figure 1. Diagram of typical electrochemical cell in commercialized Li-ion battery technologies using spinel type LiMn$_2$O$_4$ and graphite as cathode and anode, respectively. Spinel structure reprinted from "Understanding electrode materials of rechargeable lithium batteries via DFT calculations," with permission from Elsevier.[2]

The electrochemical oxidation—reduction half-reactions involved in the operation of the Li-ion battery system in figure 1 are described in equations 1.1 and 1.2. In equation 1.1, upon *discharge* the anode is oxidized, which generates electrons and Li$^+$ ions. According to equation 1.2, electrons pass through the electric circuit and end up reducing the cathode from Mn^{4+} to Mn$^{3.5+}$. And, at the same time, to compensate for the flow of negative charges, Li$^+$ ions from the electrolyte intercalate into the host structure of the spinel cathode. The electrolyte must have very low electronic conductivity to avoid short-circuiting the cell, with an associated loss of function. Current Li-ion batteries are built in the discharged state (right-hand side of Equation 1.3), and, thus, must be *charged* prior to its first use. When equations

1.1 and 1.2 are added together, the electrons and ions cancel out and we are left with the overall chemical reaction of 1.3. In a rechargeable battery, the discharge—reduction processes must be reversible while maintaining the integrity of the electrodes and electrolyte.

$$LiC_6 \rightarrow C_6 + Li^+ + e^- \tag{1.1}$$

$$Mn_2O_4 + Li^+ + e^- \rightarrow LiMn_2O_4 \tag{1.2}$$

$$LiC_6 + Mn_2O_4 \rightarrow C_6 + LiMn_2O_4 \tag{1.3}$$

The total amount of energy that can be stored in a battery depends on two principles.[3] The first is the amount of electric charge (q), measured in Coulombs (C), that is reversibly transferred between electrodes during electrochemical cycling. The magnitude of the charge of a single electron is 1.602×10^{-19} C. So a mole of electrons has a charge of $(1.602 \times 10^{-19}$ C$)(6.022 \times 10^{23}$ mol$^{-1}) = 96485$ C/mol, which is called the Faraday constant (F). Equation 1.4 shows the relationship between charge and moles (n).

$$q = n \times F \tag{1.4}$$

The quantity of charge flowing each second through a circuit is called the current. The unit of current is the Ampere (A). So a current of 1 A corresponds to a charge of 1 C per second flowing past a point in a circuit. In a completely efficient system, in faradaic terms, the total number of electrons that are transferred between electrodes is equal to the number of Li^+ ions that are reversibly intercalated. This quantity is often known as capacity and is expressed as mAh, or specific capacity, mAh/g.

The difference in electrode potentials is measured in volts (V) and this difference is the work needed (or that can be done) when moving an electric charge from one point to the other. The greater the potential difference between two points, the stronger the push will be on a charged particle traveling between those two points. When a charge (q) moves through a potential difference (E), the work done is

$$Work = E \times q \qquad\qquad (1.5)$$

Work has the dimensions of energy, joules (J).

The change in free energy, ΔG, for an electrochemical reaction, conducted reversibly at constant temperature and pressure, equals the maximum possible electrical work that can be done by the reaction

$$Work = -\Delta G \qquad\qquad (1.6)$$

The negative sign in equation 1.6 indicates that the free energy of a system decreases when work is done.

The fundamental principle relating electrochemical reaction potential (E) to the change in Gibbs free energy (ΔG) is equation 1.7. It defines a spontaneous and thermodynamically driven electrochemical reaction as the decrease in Gibbs free energy

$$\Delta G = -nFE = -Eq \qquad\qquad (1.7)$$

It is therefore intuitive to realize that to increase the magnitude of ΔG, we can increase the number of moles of electrons moved per mole of redox active species and/or increase the potential of the reaction.

1.3 DEVELOPING COMPONENTS FOR DIVALENT BATTERIES

1.3.1 ELECTROLYTES.

Extensive research is being done on the salts and solvents that compose electrolytes for divalent battery. Characteristics of an effective electrolyte are that it should be chemically stable, electrochemically stable at high and low voltage, able to insulate electrons and conduct metal ions, safe, and cheap to produce. A major challenge for rechargeable multivalent batteries is the presence of water, even trace amounts, in the electrolyte. According to table I, both Ca^{2+} and Mg^{2+} have relatively low reduction potentials compared to Zn^{2+}.

Table I Comparison of standard reduction potentials versus standard hydrogen electrode.

Cation	Electrode potential versus standard hydrogen electrode, V
Li^+	-3.04
Mg^{2+}	-2.37
Ca^{2+}	-2.87
Zn^{2+}	-0.76

The standard reduction potential of the electrolysis of water into hydrogen gas (equation 1.8) occurs at – 0.83 V vs. standard hydrogen electrode.

$$2 \ H_2O \ (l) + 2 \ e^- \rightarrow H_2 \ (g) + 2 \ OH^- \qquad\qquad (1.8)$$

If water was present in the electrolyte, it would electrolyze at more positive reduction potentials than Ca^{2+} and Mg^{2+}. This side reaction is considered parasitic because it contributes to the overall capacity but effectively reduces the coulombic efficiency of the battery. Therefore, for Ca and Mg batteries, non-aqueous electrolytes with high cathodic stability are preferred. Recently, reversible Ca metal stripping and deposition has been observed in non-aqueous, aprotic electrolytes.[4] However, due to slow kinetics, temperatures of 75 $^\circ$ C and higher were needed to promote higher rates of reaction. For Zn batteries, both aqueous and aprotic electrolytes have been researched, but the field is still in its infancy.[5,6] For instance, it is still not well understood how water, or more specifically protons, facilitate the electrochemical reactions. Also, aqueous Zn-based electrolytes have been reported to dissolve the Mn-based electrode materials which decays the cell's capacity.[7–9]

Another major challenge of electrolyte development for rechargeable divalent batteries is the chemical instability at the interface of electrodes and electrolyte. For example, in Mg battery research, conventional Mg salts, such as $[ClO_4]^-$, $[BF_4]^-$, and polar aprotic solvents, such as nitriles and carbonates, were found to decompose on the metal surface.[10,11] The surface species that form on Mg electrodes are

electronically insulating and lead to electrode surface passivation. Passivation impedes the migration of

Mg^{2+} to the electrode surface and prevents proper function of the battery. Another salt of Mg, MgTFSI$_2$

(bis(trifluoro-methane-sulfonyl)imide), is reported to be more chemically stable than conventional Mg

salts, has high anodic stability, and can facilitate reversible Mg deposition and dissolution.[12–14] When

LiTFSI is mixed with 1-Butyl-1-methylpyrrolidinium (PYR14), they form an ionic liquid electrolyte that

has high ionic conductivity and thermal stability. It is expected that the same is true for ionic liquid

Mg(TFSI)$_2$:PYR14, which will be used as the nonaqueous Mg electrolyte in Mg intercalation studies in

chapters 5 and 6.

1.3.2 ANODES

For Mg, Ca, and Zn batteries, the pure metal is preferred as the counter electrode material in order

to achieve the largest potential difference. As an example of the complexity of using metallic counter

electrodes, Mg metal suffers from high impedance in existing electrolytes due to the formation of an

electronically and ionically insulting passivation layer upon reduction.[15–18] Alloys of Mg with Bi, Sb, In,

Sn, and Pb have been investigated as alternative anode materials.[19–23] Despite their high specific capacity,

alloys have poor cycle performance. Insertion hosts like $Li_4Ti_5O_{12}$ have been investigated as well.[24] And

despite having excellent mechanical stability, $Li_4Ti_5O_{12}$ suffers from low specific capacity. Due to the

need for thermal energy to reversibly deposit and strip Ca metal in aprotic solvents, research efforts are

currently aimed at electrolyte mixtures that allow it to take place at room temperature.[4] Sn foil has

reportedly been used to develop a Ca battery that operates with capacity retention of 95 % after 350

cycles at room temperature.[25] This work has motivated theoretical studies to identify promising anode

materials for Ca batteries.[26] Lastly, Zn metal can be dissolved and deposited much more easily than Mg

and Ca, which makes it squarely the only anode of viable choice in a divalent battery. However, today,

the rechargeability of batteries based on Zn anodes remains below technological expectations because of

side reactions of corrosion or formation of an electrochemically inactive passivation layers, and the

formation of Zn dendrites and protrusions due to uneven electrostripping/electroplating.[5] Porous textiles

of carbon are being investigated as anode materials in flexible devices. They are electronically conductive

as well as chemically and mechanically stable. And due to their porosity, they exhibit fast kinetics of ion mobility.[27,28] Activated carbon cloth anodes will be used to characterize Mg^{2+} mobility in nonaqueous electrolytic environments in chapters 5 and 6.

1.3.3 CATHODES

To get a high energy density Mg battery, cathodes must have a high reduction potential versus the metal, large specific capacity for charge storage ($mAhg^{-1}$ or $mAhcm^{-3}$), low capacity fade during cycling (reversible oxidation and reduction), chemical stability with other battery components (electrolyte, electrode binder, conductive additives, current collector, and separator), and contain earth-abundant materials.[29,30] Identification of divalent battery cathode materials has followed a course that was used to identify promising cathode materials for lithium-based technologies. A large portion of published reports on Mg battery cathodes involve identification of materials with the ability to reversibly intercalate Mg^{2+}, while fewer studies exist on conversion or other types of cathodes because their reversibility is inherently lower. Conversion type cathodes have the potential to deliver higher capacities than intercalation cathodes[15] because magnesiation leads to a complete chemical rearrangement, forming new products with new structures and chemistries, through mechanisms that are not entirely understood. In the case of oxygen-containing conversion type electrodes (i.e. air or MnO_2), a significant drawback is the formation of MgO as a discharge product; which is generally considered an electrochemically irreversible reaction and lowers coulombic efficiency.[31] Organic-based cathode materials are also being investigated for use in Mg battery systems, such as the Prussian blue compound and quinones.[32,33] These materials are often described as intercalation electrodes in that their operation typically involves reduction without complete rearrangement of the original structure of the material rather than a conversion reaction involving the formation of a discreet Mg species. The two main drawbacks from organic-based cathode materials are the relatively small capacities and low cycle life. Over fifteen years ago, a reversible intercalation-based Mg battery prototype was developed after the seminal discovery of the Chevrel phase Mo_6S_8 as a cathode material.[17] While the Chevrel phase remains a benchmark for Mg batteries, its poor mobility of Mg^{2+} demands thermal activation, and its potential of operation is too low for any technological impact.

Theoretically speaking, comparable energy densities to Li-ion technologies may be achieved at lower levels of intercalation, thereby alleviating the severity of the structural changes needed to accommodate ions in the structure. Theoretical predictions using DFT calculations have targeted sulfides with the spinel crystal structure (also known as thiospinels) with promising Mg^{2+} mobilities.[34] Sun et al. identified reversible Mg^{2+} intercalation was possible in Ti_2S_4, but overall cell performance was marred by sluggish kinetics of Mg^{2+} mobility in the solid-state cathode and poor cycle life.[35] Despite their promising properties according to theoretical predictions, thiospinels as cathodes in Mg batteries have significantly lower reduction potentials compared to their oxide analogues. Because of their higher potentials of intercalation, divalent batteries with oxides cathodes will have the capacity to store more energy (equation 1.7). This fact makes oxide cathodes the object of research with the highest value proposition.

1.4 OXIDES AS INTERCALATION CATHODES FOR A DIVALENT BATTERY

A major challenge still remains when integrating high voltage oxide cathode materials with current metal anode-electrolyte systems of interest. Their high reactivity remains a double-edged sword. On one hand, it allows an electrochemical cell with the desired true high voltage. But on the other hand, it casts restrictions on the selection of the electrolyte. V_2O_5 is predicted to be a high voltage and chemically stable cathode in a DFT study.[36] In a recent experimental report, Yoo et al. identified that α-V_2O_5 is capable of reversibly intercalating one Mg^{2+} per formula unit in a Mg cell using an ionic liquid Mg electrolyte and activated carbon cloth as the counter electrode.[37] Electrochemical experiments were completed at 110 °C as it was required to improve the kinetics of Mg^{2+} mobility in V_2O_5. But this is still the first study of its kind to identify exclusive Mg^{2+} intercalation, without co-intercalation with protons;[38] which is in part related to the chemical and high anodic stability of the ionic liquid Mg electrolyte. Unfortunately, the electrolyte used is not compatible with Mg anodes. Other oxides, such as polyanion $MgXSiO_4$ (X = Mn, Co, Fe), have been tested as intercalation-type cathodes for Mg batteries.[39] MnO_2 is particularly attractive as a cathode because of its relative abundance and higher potential vs Mg compared to corresponding sulfides. It has a large theoretical specific capacity of 250 or 270 mAh/g, which would

lead to a battery with high energy if it could be paired with a Ca or Mg anode. Computational scientists predict that Mn_2O_4 with the spinel or post-spinel crystal structure is a promising cathode candidate for Mg, Ca and Zn battery.[40,41]

1.5 ION MOBILITY IN SOLIDS

In transport phenomena, flux (j) is defined as the rate of flow of a property per unit area (A)

$$j = \frac{I}{A} \tag{1.9}$$

Where I corresponds to the change in quantity (q) over time (t)

$$I = \lim_{\Delta t \to 0} \frac{\Delta q}{\Delta t} = \frac{\partial q}{\partial t} \tag{1.10}$$

Flux has units of [quantity][time]$^{-1}$[area]$^{-1}$. Diffusion is a process by which matter is transported to another area as a result of concentration gradient.[42] In isotropic substances, the rate of transfer (flux) of diffusing substance through a unit area of section is proportional to the concentration gradient measured normal to the section. This is known as Fick's First Law

$$j = \frac{-D \partial C}{\partial x} \tag{1.11}$$

Where F is the flux, or rate of transfer per unit area of section, C is the concentration of diffusing substance [mol $\cdot$ m^{-3}], x is the space coordinate measured normal to the section and D is the diffusion coefficient with units of [m^2 $\cdot$ s^{-1}]. Chemical diffusion has the units of [mol $\cdot$ m^{-2} $\cdot$ s^{-1}]. The negative sign arises because diffusion occurs in the direction opposite to that of increased concentration. For anisotropic media, diffusion properties will depend on the direction which is measured.

Ion conduction in crystalline solids is caused by the movement of charged ions that hop from their lattice site to an empty site under the influence of an electric field. The atomic structure of spinel-

type $LiMn_2O_4$ contains a cubic-close packed array of oxygen anions. The interstitial space consists of interconnected octahedral and tetrahedral sites. Mn occupy half of the octahedral sites and Li occupy a quarter of the tetrahedral ones. These sites connect through common faces and edges and provide a 3D diffusion pathway for cation diffusion. High Li^+ mobility has been realized in this structure. [43–45] In order to hop between lattice sites, Li^+ must overcome a energy barrier to move to a site with a vacancy.

Diffusion in solids varies with temperature and is governed by an Arrhenius relationship

$$D = D_o exp\left[-\left(\frac{E_A}{k_B T}\right)\right] \tag{1.12}$$

Where k_B is the Boltsman constant, T is the temperature in Kelvin, E_A is the activation energy for the ion to hop from an occupied site to a vacant one, and D_o is the pre-exponential factor that depends on the vibrational frequency of the atoms and some structural parameters. From this relationship, it is clear to see that the rate of ion diffusion in solids will be higher in hopping directions with the lowest energy barrier for ion mobility.

1.6 STRUCTURES WITH ADVANTAGEOUS ION MOBILITY

The spinel crystal structure can describe a class of minerals with the general formula AB_2X_4. The X anions are arranged in a cubic-close packed array (as shown in figure 2). In a normal (or ordered) spinel, A occupies AX_4 tetrahedral sites and the B occupies BX_6 octahedral sites. The tetrahedral sites form a network of 3D tunnels along the three dimensions. So, if the A cation is sufficiently small, ion mobility is facile in these solids. This unique quality has allowed spinel $LiMn_2O_4$ to command a portion of the commercial market in Li-ion batteries.[29]
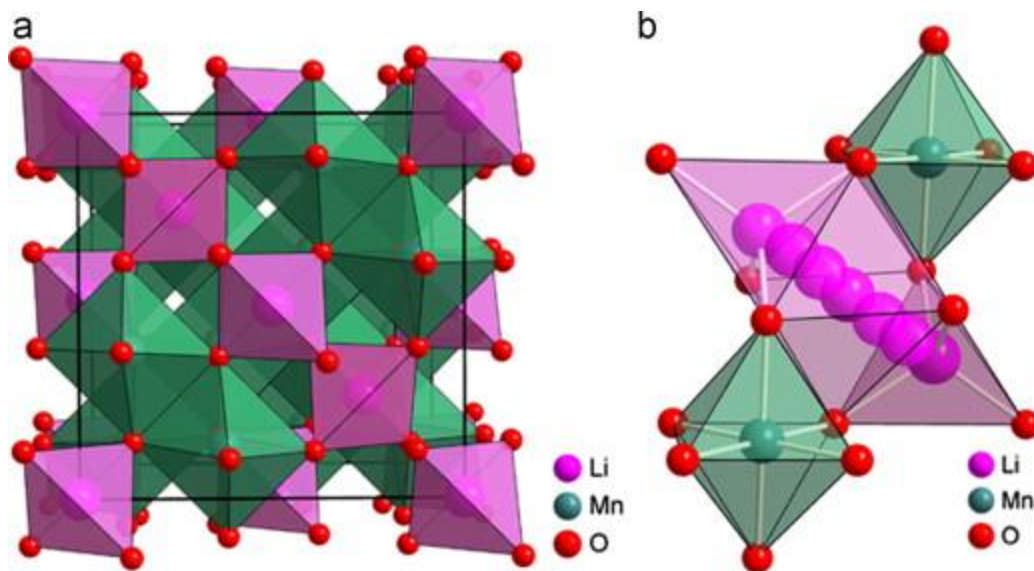
Figure 2. Visualization of the LiMn$_2$O$_4$ spinel structure. Reprinted from "Understanding electrode materials of rechargeable lithium batteries via DFT calculations," with permission from Elsevier.[2]

According to the plot in figure 3, the cell potential of spinel LiMn$_2$O$_4$ cathode paired with a Li counter electrode is 4.1 V vs. Li with a capacity of about 140 mAh/g. Recent first principles calculations have predicted Mn-based spinel structures as promising cathodes for Ca and Mg batteries.[40] The plot in figure 3 shows that the intercalation potentials of spinel Mn$_2$O$_4$ systems are 3.2 and 2.9 V vs Ca and Mg batteries, respectively. Despite lowered cell potentials, the gravimetric capacities increase to 250 and 270 mAh/g, respectively. Even though cell potentials and capacity results for divalent cathode materials show potential to go beyond lithium-ion systems, overcoming slow diffusion of multivalent cations in solids remains a major challenge. Nudged elastic band calculations were used to predict the energy barriers of Mg^{2+}, Ca^{2+}, and Zn^{2+} migration between tetrahedral sites in the Mn$_2$O$_4$ spinel structure.[40] Mg^{2+} and Zn^{2+} have the highest barriers, while those for Ca^{2+} are low enough to be comparable to Li$^+$. The energy barriers for Ca^{2+} and Mg^{2+} mobility in spinel type Mn$_2$O$_4$ are predicted to be low enough to enable a functional electrode. Fundamental investigations of divalent ion intercalation have often utilized

11

conventional aqueous cells.[46] There is experimental evidence of Mg^{2+} intercalating into spinel-type

Mn_2O_4, thus forming $MgMn_2O_4$, in aqueous environments, which is reversible but hindered by sluggish

kinetics of Mg^{2+} ion insertion into micron-sized crystalline particles.[47] The possibility of intercalating

other divalent cations, such as Zn^{2+} and Ca^{2+}, is less explored, but spinel Mn_2O_4 is being investigated as a

cathode material in aqueous Zn battery systems. However, the material suffers from capacity decay

during cycling due to low electronic and ionic conductivity of the material, structural transformation and

Mn dissolution caused by disproportionation during cycling.[5]
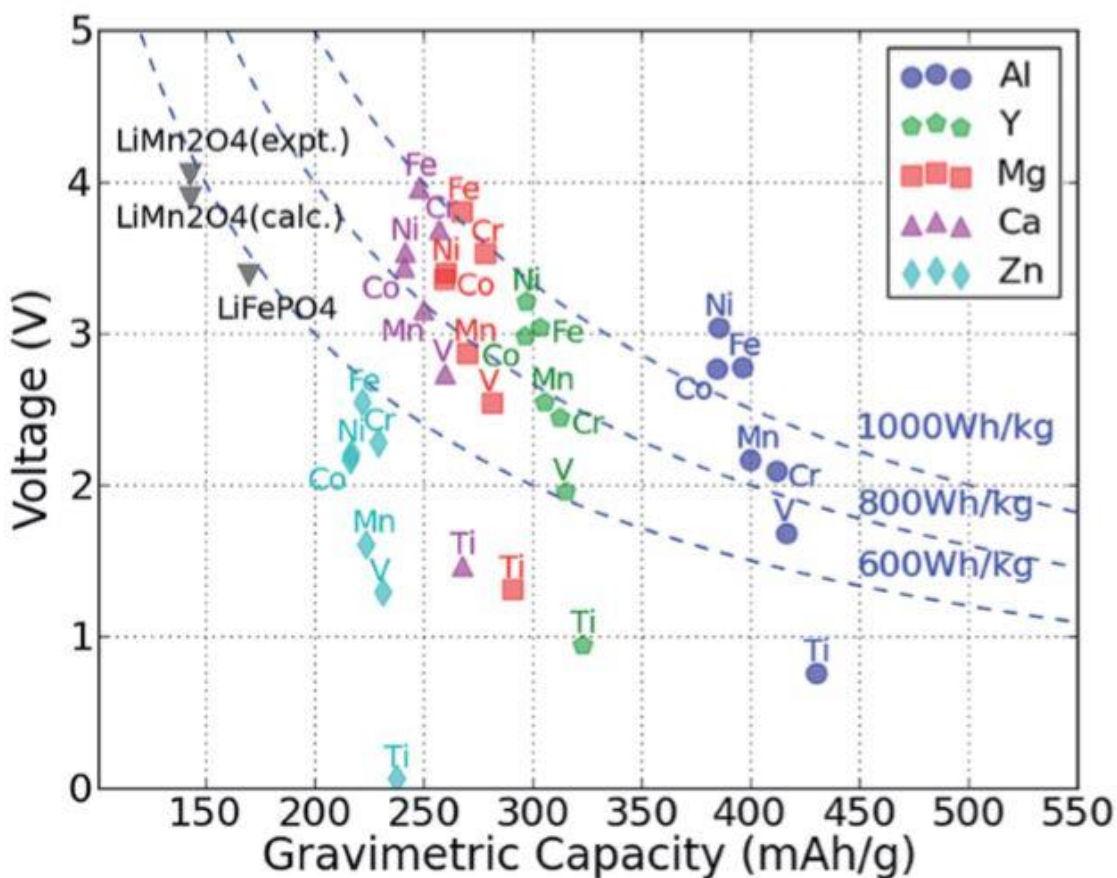
Figure 3. Plot comparing the energy densities of various metal oxides with the spinel crystal structure paired with Mg, Al, Ca, Zn and Y metal counter electrodes. Reprinted from "Spinel compounds as multivalent battery cathodes: a systematic evaluation based on ab initio calculations," with permission from Royal Society of Chemistry.[40]

Post-spinel. At high pressures, spinel compounds can transform to one of three denser structures, represented by the compounds $CaMn_2O_4$, $CaFe_2O_4$, and $CaTi_2O_4$.[41] These phases are often referred to as post-spinel phases. Ling and Mizuno note that the structures of post-spinel CaM_2O_4 (M = Mn, Fe, Ti) are related to one another with distorted MO_6 octahedra making "double-rutile chains" (figure 4), and Ca is coordinated by 8 oxygen. In $CaMn_2O_4$ and $CaTi_2O_4$ structure types, each chain of double rutile MO_6 octahedra is partnered to two neighboring chains through oxygen that share edges and also to two additional chains via oxygen that share corners. On the other hand, in $CaFe_2O_4$-type structures, the double-rutile chains are interconnected through oxygen that share apexes.[41] Due to their similar crystal structures, accurate identification of phases is challenging, but can be accomplished with high-quality X-ray diffraction data. An attractive characteristic of post-spinel materials is the potentially rapid transport of cations through the particle. 1D channels run parallel to the b axis in $CaFe_2O_4$ structure type and parallel to the c axis in $CaMn_2O_4$ and $CaTi_2O_4$ types. This property makes them potentially suitable for intercalation reactions driven by an electrochemical force. The activation energy barriers for the migration of Li^+, Na^+, and Mg^{2+} in the three post-spinel phases is shown in figure 5. Despite the similarity in the structures, the lowest energy barriers for cation migration were found in the $CaFe_2O_4$ phase. The calculations indicate that the Mg^{2+} mobility in $CaFe_2O_4$-type Mn_2O_4 is comparable to Li^+ mobility in spinel Mn_2O_4 in commercial Li-ion batteries, making them promising candidates for Mg battery cathodes.[41] Nevertheless, $MgMn_2O_4$ with the $CaFe_2O_4$ structure type cannot be obtained by high-pressure

methods because the $CaMn_2O_4$ polymorph is more stable. In contrast, single step high-pressure methods have been used to prepare $LiMn_2O_4$ and $NaMn_2O_4$ with the $CaFe_2O_4$ crystal structure, as will be discussed in chapter 6. Therefore, chemical or electrochemical ion exchange methods could be performed on these materials to offer an opportunity to investigate the possibility of reversible Mg^{2+} intercalation.
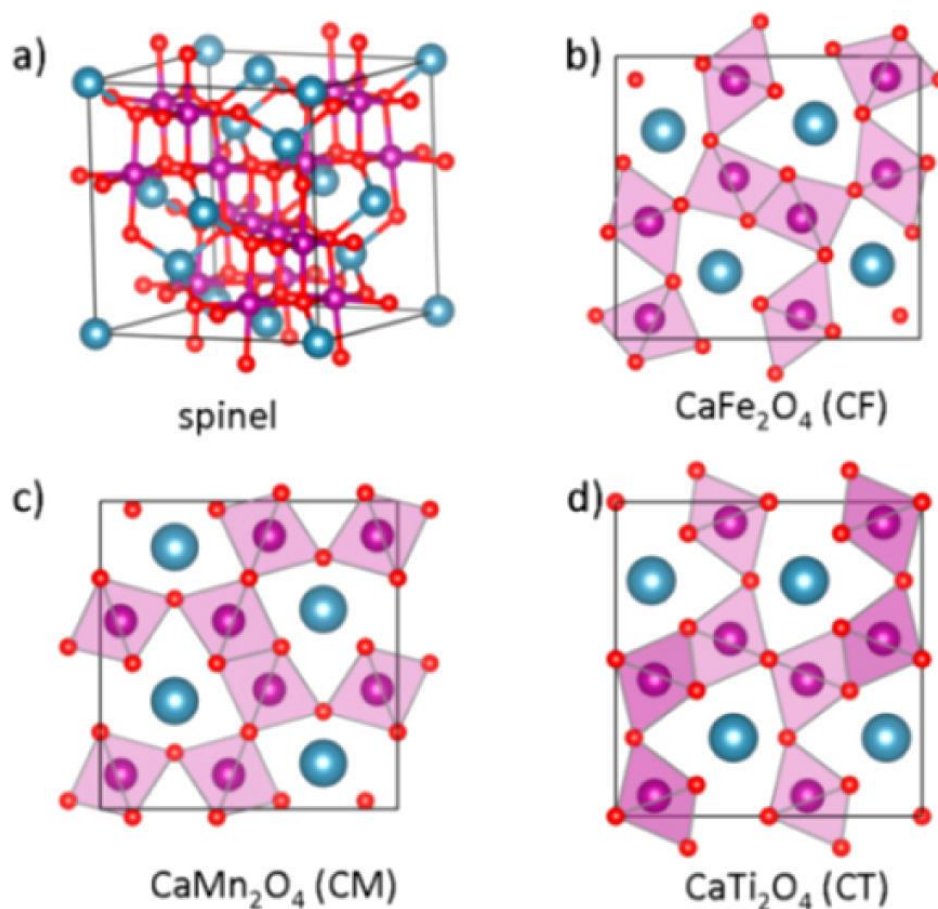
Figure 4. Visualization and comparison of the spinel-type Mn_2O_4 structure to the three polymorphs of the post-spinel Mn_2O_4. Reprinted from "Phase stability of post-spinel compound AMn_2O_4 (A = Li, Na, or Mg) and its application as a rechargeable battery cathode," with permission from the American Chemical Society.[41]
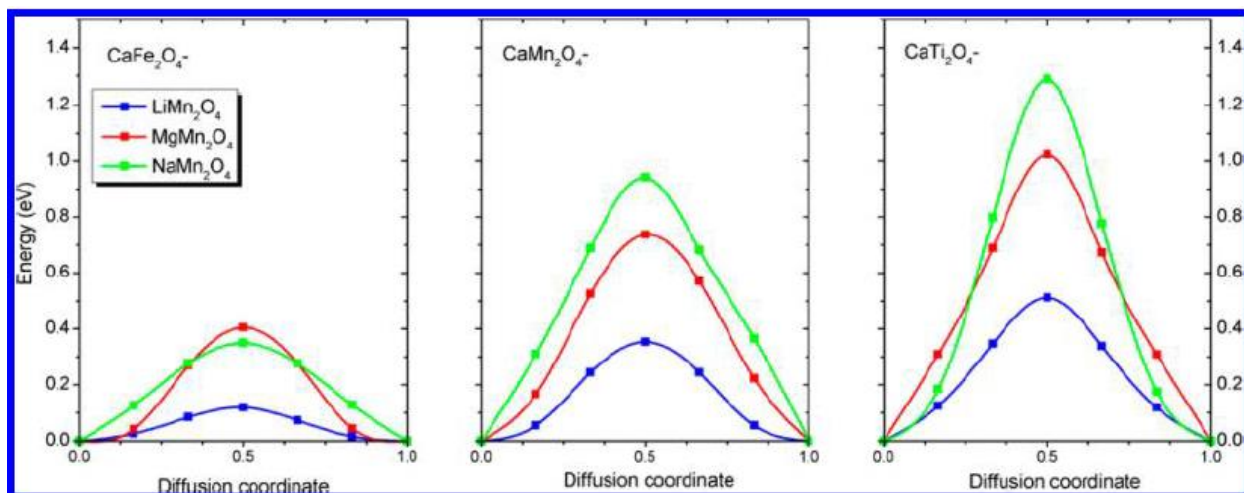
Figure 5. Plots of calculated activation energies of Li_+, Na^+, and Mg^{2+} ion mobility in three post-spinel polymorphs of Mn_2O_4 with $CaFe_2O_4$, $CaMn_2O_4$, or $CaTi_2O_4$ crystal structures. Reprinted from "Phase stability of post-spinel compound AMn_2O_4 (A = Li, Na, or Mg) and its application as a rechargeable battery cathode," with permission from the American Chemical Society.[41]

1.7 METHODS OF SYNTHESIS OF NANOPARTICLES

Evidence of humans' use of colloidal nanoparticles dates back to earliest records of civilization, such as paintings in the Lascaux caves of France (figure 3) were produced with stable colloidal pigments.[48] For an old-world concept, colloidal nanoparticles have many modern applications in catalysis, batteries, color pigments, electrochromics, photovoltaics, fuel cells, electronic, cosmetic, coating technology, gas sensors and medical science.[49] Other techniques exist to make nanomaterials. For example, gas phase techniques (such as chemical vapor deposition) are often used to make nanopowders and thin films.[50] Other methods such as co-precipitation, hydrolytic and nonhydrolityic sol-gel processes,

hydrothermal, solvothermal, template synthesis and biomimetic methods often involve not just one but many of these methods to make nanomaterials; which prevents any subtle control over crystal size and shape. The true advantage of colloidal synthetic methods in the liquid phase is that they provide a single-step pathway to consistently control the particle size, shape and size distribution of nanocrystals. Progress in our understanding of the forces that govern colloidal interactions provides new basis for scientific advancement.

The basics of colloidal synthesis to make nanoparticles of manganese oxide is presented in chapter 2. Motivated by computational studies suggesting that divalent cations could migrate sufficiently well in spinel lattices to sustain reversible electrochemical reactions at very small crystal sizes,[51] our group synthesized $Mg_{0.5}Mn_{2.5}O_4$ nanocrystals below 20 nm.[52] The materials were electrochemically active, but the existence of both Mg^{2+} and Mn^{2+} induced site exchange between both cations, resulting in the intercalation of both Mg^{2+} and Mn^{2+}. It was hypothesized that exclusive intercalation of Mg^{2+} could be achieved in stoichiometric, ordered $MgMn_2O_4$, where all of the Mn is in the +3 oxidation state. However, direct synthesis of less-than-20 nm nanocrystals of ordered stoichiometric $MgMn_2O_4$ with the spinel crystal structure has never been reported and leaves room for scientific discovery.

Figure 6. The cave-art paintings of the Lascaux caves in France. Reprinted from "Lascaux: movement, space and time," with permission from H. N. Abrams.[53]

1.8 RESEARCH GOALS

The research presented in this thesis explores the ability of spinel and post-spinel-type Mn_2O_4 to intercalate divalent cations, a previously understudied area in electrochemistry. Since electrochemical Mg^{2+} intercalation in aqueous electrolyte has been previously reported in micron-sized spinel Mn_2O_4 particles, this work will investigate the possibility of intercalating Ca^{2+} and Zn^{2+} in similar structures and water-based electrolytes (chapter 3). Due to the sluggish kinetics of Mg^{2+} in micron-sized particles, researchers predict that exclusive intercalation of Mg^{2+} could be achieved in stoichiometric, ordered nanocrystals of $MgMn_2O_4$. Follow-up work on colloidal synthesis methods, in chapter 4, sought to evaluate the level of control over Mn oxidation state in colloidal conditions, as the ordered form of spinel requires controlling it to be strictly 3+. The effects of temperature and oxidizing conditions on products

following the thermal decomposition of $Mn(acetate)_2$ and $Mn(acetylacetonate)_3$ in oleylamine during a one-step heat-up colloidal method are discussed. Following the finding that nanocrystals containing only Mn^{3+} cannot be achieved in the most common colloidal conditions, a procedure was subsequently developed to calcine colloidal nanocrystals of MnO with $Mg(acetate)_2$ to form crystalline ordered $MgMn_2O_4$ with particle sizes less than 20 nm. Their ability to reversibly intercalate Mg^{2+} cations in anhydrous electrolytes is discussed in chapter 5. Lastly, the $CaFe_2O_4$-type $LiMn_2O_4$ was prepared via both Na/Li ion exchange from $CaFe_2O_4$-type $NaMn_2O_4$ and high-pressure synthesis methods. The ability of $CF-Mn_2O_4$ to reversibly intercalate Li^+ and Mg^{2+} cations in anhydrous electrolytes is discussed in chapter 6.

2 EXPERIMENTAL METHODS

2.1 INTRODUCTION

Two synthetic procedures were chosen to make promising materials as electrodes for multivalent batteries: heat-up colloidal chemistry to form small nanocrystals with the spinel crystal structure and high-pressure synthesis for micron-sized $CaFe_2O_4$-type (i.e., post-spinel) crystals. In order to characterize the physical and chemical properties of the products, and their functionality as cathode materials, a number of electrochemical and physico-chemical characterization techniques were used. Product purity and crystallinity will be investigated with PXRD. Physical characteristics of particles will be observed with electron microscopy. Electroanalytical techniques will be used to test the performance of these materials as cathodes in multivalent batteries. X-ray absorption spectroscopy will be used to assess the difference in chemical states between the surface and bulk following electrochemical testing. Additionally, thermal analysis will be conducted to understand how materials behave under heat.

2.2 SYNTHETIC PROCEDURES

2.2.1 COLLOIDAL SYNTHESIS

Distances for transport of charge carrier are shorter in nanocrystals. It is important to target a synthesis method where control over particle size and shape is possible and products have high levels of crystallinity. Colloidal synthesis gives one control over these parameters.[54] Within this broad category, the heat-up method is a simple one-pot procedure that has the potential to be scaled up to commercial levels. This synthetic technique requires using Schlenk lines, so O_2 and H_2O levels can be down to ppb range.

Colloidal syntheses involve the precipitation of nanocrystals following thermal decomposition of precursor salts in high-boiling point solvents. This effectively entails three stages: nucleation, normal growth and competitive growth.[55] When the solvent (e.g. oleylamine) possesses a polar head group (amine) and a non-polar tail group, micelles are formed that act as nanometer-sized reactors. As the

precursor dissolves into the solvent, its concentration rises above supersaturation and a burst occurs where a large number of nuclei form. These nuclei grow rapidly and lower the concentration of the precursor while allowing the particle to grow further at a rate determined by the slowest step. It is postulated that ripening processes (competitive growth) would favor the formation of larger particles at the expense of smaller ones because smaller nanocrystals have more reactive surfaces. The micelles not only suppress uncontrolled growth but can further direct growth to certain physical dimensions. Also, using Schlenk line techniques, one can quickly reduce O_2 and H_2O levels down to ppb range. Water and other lower boiling point impurities may be removed by heating and creating a vacuum.

All colloidal synthesis experiments were carried out using standard Schlenk techniques under nitrogen atmosphere. $Mn(OAc)_2$ (98 %), $Mn(acac)_3$ (technical grade), and trimethylamine N-oxide dihydrate (TMNO·$2H_2O$, 98 %) were purchased from Sigma-Aldrich and used without further purification. Oleylamine (Sigma-Aldrich, 70 % pure) was also used without additional purification. In a typical heat-up synthesis, a mixture of either $Mn(OAc)_2$ or $Mn(acac)_3$ and oleylamine in a molar ratio of 1:12 Mn to oleylamine was prepared in a three-neck round bottom flask (figure 7). For each Mn salt, reactions were completed either under inert atmosphere or in air. In the former case, reactions were conducted with and without a mild oxidizer, TMNO·$2H_2O$. To ensure inert conditions, the reaction flask was capped in the Schlenk line, and evacuated under constant stirring at room temperature until bumping ceased. The reaction slurry was then heated to 100 ºC; whereupon the flask was degassed at least twice until bubbling ceased. Longer times were needed to degas the reactions with TMNO·$2H_2O$ because the salt contained crystalline H_2O. To carry out the synthesis in air, the reaction mixture was left under constant magnetic stirring and exposed to laboratory atmosphere. Following the proper pre-reaction setup for each type of reaction, the flask was rapidly heated to the desired temperature, followed by a dwell period and cooling to room temperature. After the synthesis was complete, 30 mL of a polar organic solvent were added, the product was centrifuged and the supernatant was separated off (figure 8). The process was repeated twice with 10 mL of hexane and 20 mL of non-polar solvent to remove the remaining unreacted surfactant. The resulting powder was dried overnight at 60 ºC.
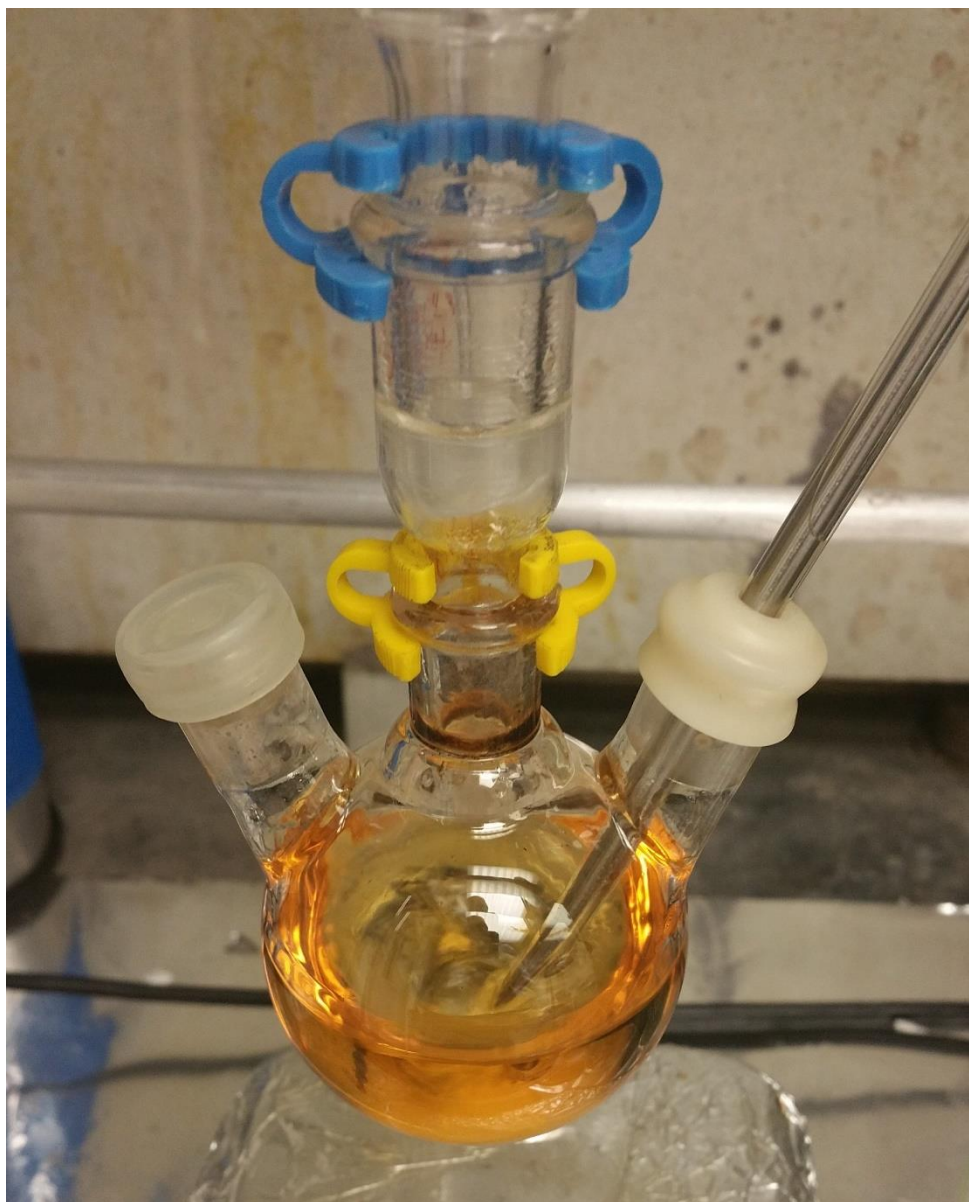
Figure 7. Image of an example colloidal reaction where Mn(OAc)$_2$ has solubilized and been properly

degassed in oleylamine in a round-bottom flask.
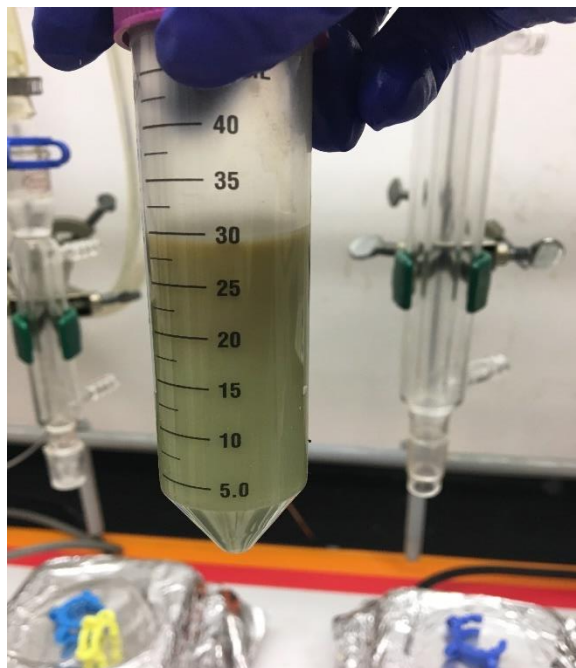
Figure 8. Precipitated nanocrystals of MnO prior to being centrifuged.

2.2.2 HIGH-PRESSURE SYNTHESIS

This spinel to post-spinel transformation is known to occur at high pressures, above 6 GPa.[56] Products from high-pressure syntheses tend to have higher tap densities and unexpected electrochemical properties. The quest for phases in this structural space is motivated by predictions of facile mobility of cations (Li^+, Na^+, and Mg^{2+}) in Mn_2O_4 with the $CaFe_2O_4$-type crystal structure.[41] High-pressure synthesis reactions can provide access to solid-state compounds that cannot be formed with traditional methods. $LiMn_2O_4$ with $CaFe_2O_4$ structure type was as made by using a Belt Press (shown in figure 9). Precursors of Li_2O_2, Mn_2O_3 and MnO_2 were mixed in molar ratios of 1:2:1 of Li to Mn^{3+} to Mn^{4+}. The final nominal composition is $Li_{0.8}Mn_2O_4$. Then, this mixture was put into a platinum capsule (figure 14), pressurized to 70 kbar (7.0 GPa) and then annealed at 1200 ˚C for 15 min. Product yields were between 70 – 80 mg (80 % efficient) when using the Belt Press. $NaMn_2O_4$ with $CaFe_2O_4$ structure type was made using the Conac Press (figure 11) and yields may be as large as 1 – 2 g of product. In the synthesis of $NaMn_2O_4$, Na_2O_2

and Mn_2O_3 were mixed in a molar ratio of 1:2 of Na to Mn. This mixture was then placed in a gold capsule, pressurized to 50 kbar (5.0 GPa) and calcined at 1000 ˚C for 60 min.

Figure 9. High-pressure Belt Press at Universidad Complutense in Madrid, Spain.
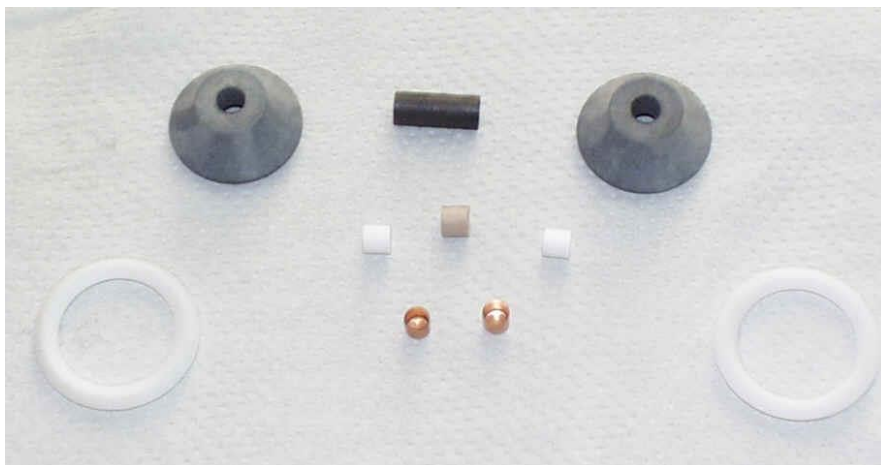
Figure 10. Components to high-pressure synthesis reactor. Gold capsule shown.

Figure 11. High-pressure Conac Press at Universidad Complutense in Madrid, Spain.

2.3 ELECTROANALYTICAL CHEMISTRY

Electroanalytical methods are concerned with the interplay between electricity and chemistry; namely, the measurements of electrical quantities, such as current, potential, or charge, which are used to induced chemical redox reactions.[3] These methods have a certain advantage over other types of analytical techniques. First off, electrochemical measurements are often specific for a particular oxidation state of an element. Second is that instrumentation is relatively inexpensive compared to other methods. When exploring materials for battery applications, electrochemical testing is vital to determining the functionality of the cell components. In this work, electrodes will be characterized using current-controlled methods.

Galvanostatic methods involve the application of a constant current, I, and the potential, E, response is measured as a function of time.[57] These methods may also generally be called chronopotentiometric, because E is determined as a function of time. We know that current is the quantity of charge transferred past a point per unit of time. Since a constant and controlled current is applied, based on the time that has elapsed, one can know how much charge has been transferred in a galvanostatic experiment. Such knowledge can be used to estimate compositional changes in the electrode, such as the amount of a cation (e.g., Mg^{2+}) that may be intercalated into its crystalline structure (e.g., Mn_2O_4).

2.3.1 PREPARATION OF WORKING ELECTRODE

Oxide powder was first thoroughly mixed with acetylene black as a conductive agent using a mortar; then the solution of polymeric binder was added and mixed to get the slurry. The binder solution was 6 wt.% polyvinylidene fluoride (PVDF, Solvay) dissolved in 1-methyl-2-pyrrolidinone (NMP, Sigma Aldrich, >99%) solvent. The ratio of active material, conductive agent, and polymeric binder was adjusted to 6:2:2. The slurry was coated on stainless steel or aluminum foil substrates, followed by drying under infrared (IR)-lamp for 30 min. The area of electrodes was 1.27 cm^2 with mass loading of ca. 1.7 mg. The electrodes were dried under vacuum at 80 °C overnight before usage.

2.3.2 AQUEOUS ELECTROCHEMISTRY

Electrochemical analysis was performed in a three-electrode, beaker cell setup. The working, counter, and reference electrodes were delithiated spinel Mn_2O_4, platinum mesh, and saturated calomel electrode (SCE), respectively. The electrolytes were composed of either $Ca(NO_3)_2 \cdot 4H_2O$ or $Zn(NO_3)_2 \cdot 6H_2O$ (Sigma Aldrich) dissolved in deionized water at a concentration of 1 M. The pH values of acidic Ca^{2+} electrolyte and Zn^{2+} electrolyte were 5.45 and 5.13, respectively. In order to minimize dissolution of Mn during the reactions, experiments were carried out were droplets of a 1 M aqueous KOH solution was titrated into the electrolytes.[13] A few drops of 1 M KOH (aq) solution increased the pH of the Ca^{2+} electrolyte to 9.18, prior to precipitation of a solid, likely $Ca(OH)_2$. Experiments were carried out at both pH values for comparison purposes. In turn, the pH of the Zn^{2+} electrolyte rose to only 5.3 before an insoluble solid (likely, ZnO) formed, preventing a further change in pH. Experiments were carried out in the near-saturated state, before solid formation.

2.3.3 NONAQUEOUS ELECTROCHEMISTRY

Two types of general electrochemical experiments in non-aqueous were used in this thesis. In the first type, a Li coin cell is used to investigate Li^+ intercalation/deintercalation. This cell also serves a double-feature. Electrolytes of Mg batteries are not optimized yet and not stable against high voltage oxide cathodes, so Mg^{2+} deintercalation upon oxidation could be studied in a Li^+ electrolyte, which, in this case, only acts to provide an ionically conductive medium that closes the circuit. Upon electrochemical oxidation, it is impossible for Li^+ to intercalate into the working electrode due to the potential bias of the electrochemical cell. The working electrode and a piece of lithium foil (Alfa Co., 99.9%, 0.75 mm thick) was separated by a glass fiber filter (VWR Co., grade 691, 210 □m thick, USA catalog # 28297-289, EU Cat# 516-0036) soaked with Li^+ electrolyte (Selectilyte LP57, BASF Co., 1.0 M $LiPF_6$ in EC/EMC (3:7 w/w)). The stack was placed in a 2032 coin cell. A multi-channel battery cycler (BCS-805, Bio-Logic) was used for the electrochemical tests at room temperature. A multi-channel potentiostat (VMP-3, Bio-Logic) was used for the electrochemical tests at 50 °C.

The second type of cell targeted electrochemical reactions of intercalation of magnesium. These 2032 coin cells contained a Kynol® activated carbon cloth as a counter electrode (American Technical Trading INC.), a microfiber glass fiber separator and 0.5 M $Mg[N(SO_2)_2(CF_3)_2)_2$-$(C_9H_{20}N)(N(SO_2)_2(CF_3)_2]$ ionic liquid electrolyte (abbreviated as $MgTFSI_2$-$PY_{14}TFSI$) with low H_2O content (~43 ppm) as electrolyte. Electrolyte was made in-house by

mixing $MgTFSI_2$ (M1208c, Solvionic) and $PY_{14}TFSI$ (Pyr0408a, Solvionic) for 1 hour at 60°C in Ar-filled glovebox then dried under vacuum for 48 hours at 110°C. For Mg cells, the potential of working electrode was calibrated by considering the ACC counter electrode's potential, which was originally 2.2 V vs Mg/Mg^{2+} and linearly proportional to the state-of-charge. All cells were fabricated or opened in a glove box (MBraun) under inert atmosphere filled with Ar gas, where water and oxygen levels were less than 0.1 ppm.
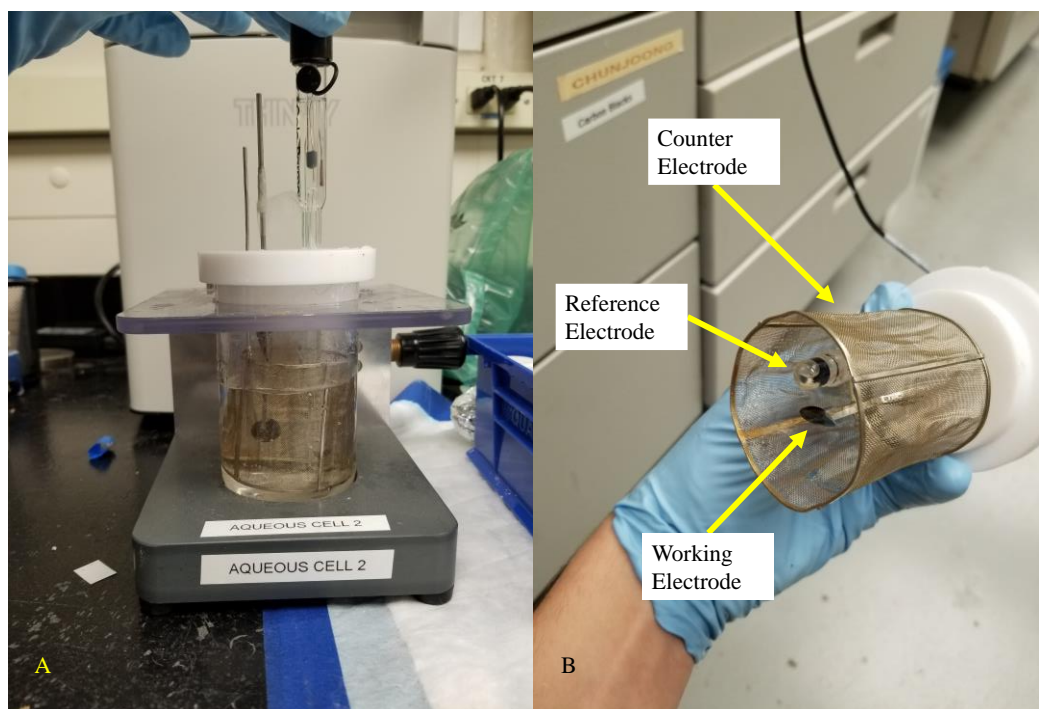
Figure 12. Aqueous beaker cell with (a) full-frontal and (b) inside views. The reference and counter

electrodes were Pt mesh and saturated calomel electrodes, respectively.

Figure 13. Typical Li-ion coin cells with binder clip for size estimation purposes.

2.4 POWDER X-RAY DIFFRACTION

The energy density and long-term stability of a battery system is dependent on the crystal structure of the working electrode. Intercalation reactions involve change in composition that should be reflected, with very few exceptions, in a change in the atomic structure of the host, leading to a measurable structural change in the crystal lattice. Probing and understanding the changes can help determine the identity of the reaction and its prospects of reversibility, which will critically affect function and capability of the electrode.

In order to observe phenomena of structure with dimensions $10^{-8} – 10^{-10}$ m, we need to use radiation with wavelengths comparable to or smaller than the distance between the atoms. X-rays are ideal candidate for characterizing solids. In a solid, each point can be regarded as a coherent point scatterer and the strength which radiation is scattered by is proportional to atomic number. When atoms are arranged periodically, as in a crystal, the scattering of X-rays from lattice planes produce interference patterns as the waves combine constructively or destructively (figure 15).[58] This interference pattern is known as the diffraction pattern or diffractogram. A diffraction pattern contains structural information about the periodicity and symmetry of atomic arrangement in a crystal.
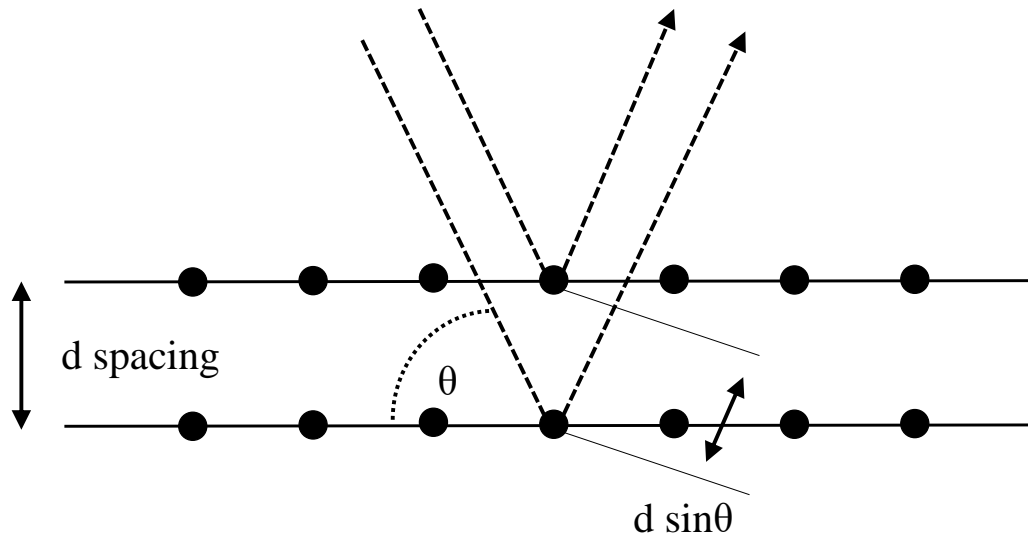
Figure 14. The schematic geometric derivation of the Bragg Law where constructive interference occurs when the delay between scattered waves from adjacent lattices are integral multiples of the radiation wavelength (nλ).

The Bragg condition for observation of reflections is as follows:

$$n\lambda = 2d \sin \theta \qquad\qquad (2.2)$$

To understand the Bragg condition (equation 2.2), waves scattered from adjacent crystal lattice planes will be just in phase (the difference in the path traveled by these waves will be an integral nλ), only for certain angles of scattering. The observed peaks of scattered intensity may also be called reflections. In the Bragg condition, λ is the wavelength of radiation used, n is an integer, nλ is the total path difference between waves scattered from adjacent crystal lattice planes, d is the perpendicular spacing between

30

lattice planes in the crystal, θ is the complementary (90 – 0º) of the angle of incidence of the X-ray beam (and thus the complement of angle of scattering or reflection).

In-house powder X-ray diffraction was performed on a Bruker D8 Advance using Cu Kα (λ_{avg} = 1.5418 Å) radiation. Scan rates were 0.04° s^{-1} from 10° to 80° (2θ). The XRD patterns of harvested electrodes were aligned by linearly shifting them based on the position of the (220) peak of stainless steel (JCPDS card number: 33–397, austenitic Fe 0.70 Cr 0.19 Ni0.11), which was used as an internal standard.

Because of the similar crystal structures in the post-spinel family, precise phase identification can be challenging. Additionally, peak broadening due to nanocrystallite sizes impedes precise identification of multiple phases present. Furthermore, the limit of detection is lower for synchtrotron XRD. Therefore, high resolution synchrotron radiation was used. Synchrotron X-ray powder diffraction (S-XRD) Samples were loaded in Kapton capillaries (0.9 mm diameter) and mounted on bases provided by the Advanced Photon Source, Argonne National Laboratory. High resolution synchrotron powder diffraction data were collected using beamline 11-BM-B with an average wavelength of 0.414 Å for all compounds. Two platinum-striped collimating mirrors and a double-crystal Si(111) monochromator are used for the X-ray optics. The data points were collected at room temperature with a step size of 0.001° 2θ and scan speed of 0.01 °/sec. Data are collected while continually scanning the diffractometer 2θ arm. High resolution and short collection time is obtained by using a unique 12-element Si (111) crystal analyzer/detector.

Analysis of the diffraction data may be performed in three different ways: the Le Bail, Pawley and Rietveld methods of structural refinement. A common function between each method is that the experimental data is compared to a calculated, theoretical pattern in order to determine which crystalline phases are present, their symmetries (i.e., space group) and lattice constants, average particle sizes, or microstrain. A simple series of direction for the Pawley method is presented in a blog.[59,60] Pawley and Le Bail refinements are faster and less computationally demanding than Rietveld refinements, providing information on lattice dimensions and structural phases in material. Rietveld refinements also account for thermal parameters, individual atomic positions, and site occupancies of elements with the highest quality data. In this work, both Pawley and Rietveld methods will be used to calculate crystallographic

information from experimental diffraction data. For samples characterized by in-house XRD ($\lambda = 1.54$ Å) or poor quality synchrotron ($\lambda = 0.41$ Å) data, Pawley refinements were performed since the observed reflections did not have enough intensity to perform Rietveld refinements on. GSAS-II was used exclusively to perform Pawley refinements. For high-quality synchrotron diffraction data, FullProf was used to perform Rietveld refinements.

2.5 ELECTRON MICROSCOPY

The naked eye cannot examine particles in the micrometric to nanometric scale. It is important to observe actual shape, morphology and particle sizes of samples. Especially for papers on synthesis of nanomaterials with high quality, statistics are important to accurately report average particle sizes.[61] Electron microscopy techniques like scanning and transmission electron (SEM and TEM) are routinely used study objects in this range.[62] In the early 20th century, physicists discovered that electrons possess both particle and wavelike characteristics and proposed that the wavelength of an electron is given by

$$\lambda = \frac{h}{p} = \frac{h}{mv} \tag{2.3}$$

Where h = 6.626 x 10^{-34} Js is the Planck constant; p, m, and v represent the momentum, mass and speed of the electron. Momentum is the product of mass and velocity. The velocity of an electron is determined by the accelerating voltage, or electron potential (eV)

$$eV = \frac{1}{2}mv^2 \tag{2.4}$$

Therefore, the wavelength of propagating electrons at a given accelerating voltage can be determined by

$$\lambda = \frac{h}{\sqrt{2meV}} \qquad\qquad (2.5)$$

For electrons (m = 9.1 x 10 $^{-39}$ kg) emitted into a vacuum from a heated filament and accelerated through a potential difference of 300 keV, their wavelength is 2.24 x 10^{-3} nm.

In transmission electron microscopy, electrons penetrate through a thin specimen and are imaged by appropriate lenses. In this work, a 300 keV transmission electron microscope is used. Electrons accelerated at this voltage are easily scattered or absorbed in thick regions; which is the main limitation of TEM. As a result, sample preparation must ensure a high dispersion of small particles onto an ultrathin membrane as substrate

Scanning electron microscopy was developed to overcome limitations of penetration so that thick specimens may be examined. SEM operates by focusing an incoming beam of primary electrons and scanning across a sample in 2 directions to create a raster. The primary electrons are scattered by the sample and generate secondary electrons. The raster of secondary electrons is then collected and converted into an image point-by-point, rather than simultaneously like in transmission mode. TEM and SEM provide info on physical structure of the sample. Often there is a need for chemical information, such as local chemical composition. As atomic number increases, the nuclear charge increases, drawing electrons closer to the nucleus and changing their energy. Inner shell electrons are the most insightful because they do not participate in bonding so their energies are unaffected by surrounding atoms but remain indicative of nuclear charge and therefore atomic number. When an inner shell electron makes a transition from a higher to a lower energy level, the subsequent relaxation emits a characteristic X-ray photon whose energy is equal to the difference of two quantum levels.

Transmission electron microscopy (TEM) was completed using a JEM 3010 (JEOL) operated at 300 kV. The samples were prepared by taking a small aliquot of powder sample and sonicating in chloroform for at least 30 minutes. Then, using a pipette, the sample was drop-casted onto a 200 x 200 mesh copper TEM grid with an amorphous carbon layer. At least three drops were casted. Energy

dispersive X-ray spectroscopy is an analytical tool for elemental analysis to be completed while analyzing a sample with an electron beam microscope. It relies on the fact that each element has a unique atomic structure allow0ing a unique set of peaks in its emission spectra. Emission is when an atom makes transition from a higher state to a lower state while emitting electromagnetic radiation.

Atomic resolution STEM imaging was completed at 200 kV using an aberration-corrected JEM-ARM200CF (JEOL). In STEM, the incident beam is converged to a focal point (< 2nm diameter) and rastered across the sample. Because the beam is rastered across sample, we can perform analytical techniques like EDS and get spatial mapping with atomic resolution. 300 kV is the conventional voltage, but 200 kV was used because sample damage occurred at higher voltages.

2.6 X-RAY ABSORPTION SPECTROSCOPY

Core level spectroscopy is a powerful tool for the study of electronic states in solids.[63] X-ray radiation is sufficiently high enough in energy to excite core electrons. A direct implication is that information from core level spectroscopy is element specific. X-ray fluorescence, transmission, and absorption methods are widely used for the qualitative and quantitative determination of all elements in the periodic table having atomic numbers greater than 4, as well as, in some cases, their oxidation states. Identifying how the electronic structure of the electrode is affected by electrochemical cycling is critical for determining any possible mechanism for intercalation. This is because intercalation is defined in part by redox reactions of a transition metal. And when a metal undergoes redox, the Fermi energy changes in the band structure, which is observable given the right radiation.

X-ray absorption spectroscopy uses X-ray photons to directly probe the unoccupied valence states of an element. A photon that enters a solid can be scattered or it can be consumed in the photoelectric effect. All other photons will be transmitted and will leave the sample without change in forward direction. In XAS, the absorption of X-rays by a sample can be measured by comparing the intensity of the beam before the sample and after being transmitted through. When X-rays interact with matter at

sufficiently high energies, it will be absorbed causing a transition in the electronic structure. In XAS, a

core electron is excited near the threshold by the incident xray radiation to empty states at high energy

and, ultimately, to the continuum. As a result, the xray absorption spectra is essentially an observation of

the density of empty states in a compound, as well as the binding energy of the core electron, as in X-ray

photoelectron spectroscopy. The X-ray selection rules are based on electric dipoles, so that if the orbital

quantum number of the final state of an excited core electron differs by 1 from the initial state ($\Delta L = \pm 1$,

i.e. s → p, p → s or d, etc.) and the spin is conserved ($\Delta S = 0$) then an absorption event is observed.

Electrons may be promoted from different core orbitals depending on the incident energy of radiation.

The nomenclature of XAS recognizes the original core level. Excitation from n = 1 core level are called

K-edges (figure 16). Promotions from n = 2 core level are called L-edges.
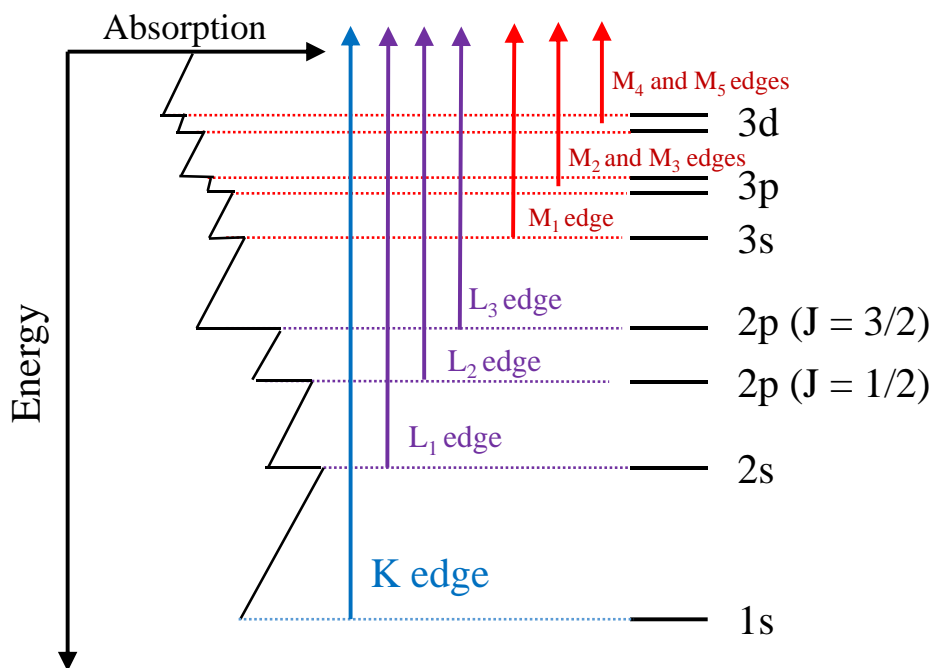
Figure 15. Core electron transitions that contribute to XAS spectra.

Soft X-ray absorption spectroscopy measurements were completed at beamlines 6 and 8 at the Advanced Light Source at Lawrence Berkeley National Laboratory and at 4-ID-C at Argonne National Laboratory's Advanced Photon Source beamline. Data was collected in both the total-electron-yield (TEY) and total-fluorescence yield (TFY) mode utilizing photocurrent for the TEY and a silicon drift diode detector for the TFY. Data were obtained at a spectral resolution of ~0.2 eV, with a 2 sec dwell time. 3 scans were performed on each sample, at each absorption edge, and scans were averaged in order to maximize the signal to noise ratio. Mn $L_{2,3}$- and O K-edges were scanned from 670 – 630 and 560 – 520 eV, respectively.

Hard X-ray absorption spectroscopy measurements of Mn K-edge were scanned from 6520 – 6660 eV at the University of Washington with a laboratory-based spectrometer[64] based on the design of Seidler et al.[65] and the Advanced Photon Source at Argonne National Laboratory beamline 10-BM. All samples were measured in transmission mode. The instrument at the University of Washington was configured with a X-ray tube source (Varex VF80 Pd anode) operated at 35 kV and 100 W total tube power, a Si(440) spherically bent crystal analyzer (XRSTech) aligned according to the method of Mortensen et al.,[66] and a silicon drift detector (Amptek SDD-X123) which rejected background counts and harmonics. The ion exchanged $CaFe_2O_4$-type $LiMn_2O_4$ laminate was prepared by spreading the material onto a thin aluminum current collector, while the as-made $CaFe_2O_4$-type $LiMn_2O_4$ and $NaMn_2O_4$ materials were pelletized using a cellulose binder. Data were collected over several hundred eV to allow proper pre- and post-edge correction in Athena.[67] The other manganese oxide compounds were measured at beamline 10-BM and included as empirical standards. Excellent agreement between the spectra of multiple cathodes collected at the University of Washington and at beamline 10-BM facilitated the establishment of a common energy scale. At beamline 10-BM, an Oxford Si (111) monochromator, consisting of a water-cooled first crystal, designed by the IIT Center for Synchrotron Radiation Research and Instrumentation, and a 50mm long second crystal, which provides an energy range of 4.0keV to 32keV from the fundamental reflection. Both crystals have been chemically polished and have been

measured to deliver the theoretical photon flux to the experimental station. The second crystal has Bragg parallel and normal motions and is run at 50% detuning for removal of harmonics. The experimental station is 25m from the source which provides a relatively high photon flux density without the need of focusing optics. The monochromator is exceptionally easy to set through the use of a GUI which allows the user to select an element to be measured. Beamline 10-BM is operated by the Materials Research Collaborative Access Team and is currently equipped with 22cm long aluminum spectroscopy ion chambers for use in transmission mode X-ray absorption spectroscopy and 6 smaller Cornell-type ion chambers which may be mounted on the spectroscopy rail for special purposes. Three Lytle-type fluorescence detectors are also available. Data collection is through a standard instrument chain of Keithley electrometers, V-F converters and a 32 channel multichannel scaler. The multichannel scaler permits continuous of the energy and the goniometer detector motors.

An electron that relaxes into a core hole gives rise to an avalanche of electron, photons and ion escaping from the surface. The excited core electron can relieve its excess energy either radiatively, through the emission of a fluorescent photon, or non radiatively through the emission of an Auger electron. So two types of detection can be available in certain XAS beamlines. The photons created in fluorescent decay have a mean free path of the same magnitude as the incoming X-ray, at least, over 100 nm deep into the sample. Silicone drift diode detectors were used to determine fluorescing spectral events as a function of beam energy. With the total electron yield method, all electron that eject from the sample surface are detected. The interaction of electrons with solids is much larger than the interaction of xrays, which implies that the electrons that escape from the surface must originate close to the surface. It is common that electron yields are detected using devices such as pico-ampere meters and channeltrons to amplify emitted electrons to a detectable level. The advantage of using both detection modes for ejected electrons and fluorescing photons is the simultaneous contrast of surface- to bulk-sensitive information, respectively. This allows one to compare the differences in electronic structure at the surface compared to the bulk.

2.7 THERMOGRAVIMETRIC AND DIFFERENTIAL SCANNING CALORIMETRY ANALYSIS

It is useful to understand how materials behave at elevated temperature. The study of the effect of heat can be traced back to mankind's first attempts at pottery, extracting metals (~8,000 BC), and forming glass (~3,400 BC). When a single pure substance is heated, there is an increase in molecular, atomic, or ionic motion that may lead to changes in crystal structure, sintering, melting or sublimation. Phase changes in materials are usually accompanied by measurable changes in heat and sometimes by gains or losses in mass.[3] Due to the technological advancements in balances, small amounts of sample (< 20 mg) are needed for accurate studies.

In TGA, measurements of changes in mass with temperature are performed on a substance according to controlled heating/cooling program.[68] In DSC, sample and reference are maintained at the same temperature throughout the controlled program and changes in enthalpy (i.e., heat) measured. Thermal events correspond to phase changes and appear as deviations from the baseline, either in endothermic (down) or exothermic (up) directions. Depending on whether more or less energy has been supplied to the sample relative to the reference.

Thermogravimetric analysis (TGA) and differential scanning calorimetry (DSC) experiments were completed using a TA Instruments SDT Q600. Powder precursors were heated to 320 °C at a heating rate of 5 °C per minute, following a 30-minute isotherm at 50 °C. A 30-minute isothermal step at 50 °C was added to promote complete saturation of the reaction chamber with the gas used. Separate experiments were completed using either synthetic air or N_2 (Praxair). Upon reaching 320 °C, the temperature was maintained for two hours before cooling.

3 ELECTROCHEMICAL REDUCTION OF A SPINEL-TYPE MANGANESE OXIDE CATHODE IN AQUEOUS ELECTROLYTES WITH Ca^{2+} OR Zn^{2+}

3.1 INTRODUCTION

Energy storage devices that couple intercalation hosts at the cathode with a metal counter electrode have the potential to store energy at low cost and volume. Oxides with the spinel structure are among the best performing hosts for intercalation of Li, both in terms of reversibility and kinetics, primarily due to their 3-dimensional channels for ion diffusion.[3] Recent first principles calculations have predicted manganese-based spinel structures (Mn_2O_4) as promising cathodes for multivalent batteries.[4] Due to the well-known difficulty to use non-aqueous electrolytes with sufficiently high anodic stability to pair with oxides, fundamental investigations of divalent ion intercalation have been focused on conventional aqueous cells.[5] There is experimental evidence of Mg^{2+} intercalating into spinel-type Mn_2O_4, thus forming $MgMn_2O_4$, in aqueous environments, which is both extensive and reversible.[6,7] The possibility of intercalating other divalent cations, such as Zn^{2+} and Ca^{2+}, is less explored. To date, successful intercalation of Ca^{2+} into a cubic spinel Mn_2O_4 host has not been reported. Reversible Ca^{2+} intercalation was claimed in V_2O_5, FeS_2, Mo_3Se_4, as well as into the Prussian blue (manganese hexacyanoferrate) structure.[8,9] On the other hand, previous reports have claimed reversible intercalation of Zn^{2+} into Mn_2O_4.[10-12] In a report by Xu *et al.*, the mechanism of reaction remained unclear, as the active material was composed of 4 nm spheres and poorly crystalline; the amorphous characters significantly complicate the analysis by powder X-ray diffraction, which is critical to establish the structural transitions.[10] Additionally, reversible Zn^{2+} intercalation has been claimed in a composite cathode consisting of a Mn-defected spinel $ZnMn_{2−x}\square_xO_4$ ($\square$=vacancy) and carbon, using 3 M aqueous $Zn(CF_3SO_3)_2$ electrolyte.[11] Initial discharge capacities were at least 160 mAh $g^{−1}$, depending on current

densities. The improved electrochemical performance of this system is attributed to Zn^{2+} migration through vacant octahedral sites. Interestingly, Alfaruqi et al. reported the formation of spinel-type $ZnMn_2O_4$ during the reduction of □-MnO_2, with a tunnel structure, in the presence of an aqueous electrolyte containing 1 M $ZnSO_4$.[12] Despite these reports, there is still a need to investigate the Ca^{2+} and Zn^{2+} divalent ions intercalation into crystalline, defect-free spinel manganese oxide host materials. Aside from generalizing our knowledge of intercalation electrochemistry from the cases of Li^+ and Mg^{2+}, it would justify further efforts to design oxide hosts that can pair with Ca and Zn metal counter electrodes in compatible nonaqueous electrolytes.

In this chapter, the electrochemical reactivity of crystalline spinel-type Mn_2O_4 in the presence of 1 M aqueous electrolytes, with $Ca(NO_3)_2$ or $Zn(NO_3)_2$, was investigated using diffraction, microscopic imaging and X-ray absorption spectroscopy (XAS). The results provide evidence that, unlike Mg^{2+}, reversible intercalation does not seem viable in these conditions. The electrochemical reactions were found to be complex. In the case of Ca^{2+}, partial transformation of cubic spinel Mn_2O_4 to tetragonally distorted spinel Mn_3O_4 was found. In the case of Zn^{2+}, the parent Mn_2O_4 host structure was preserved and accompanied by the formation of minor Mn_3O_4, ZnO, and $Zn_2Mn_3O_8$ phases. Furthermore, XAS analysis indicates the reduction of Mn^{4+} to Mn^{3+} and Mn^{2+} in conjunction with the formation of a tetragonal spinel Mn_3O_4.

3.2 METHODS

Preparation of electrochemically delithiated spinel Mn_2O_4, acidic and basic Ca^{2+} electrolyte and Zn^{2+} electrolytes, and reduction of the spinel host in those electrolytes is detailed in chapter 2. Materials characterization:

Details about the methods of characterization can be found in chapter 2. Galvanostatic cycling in Li and beaker cells was completed at 25 °C. Structural characterization was completed using powder X-ray diffraction using both $\lambda_{avg} = 0.412647$ and 1.5418 Å radiation. Scanning, transmission and scanning transmission electron microscopes were used to characterize particle size and morphology. X-ray absorption spectroscopy was used to characterize Mn $L_{2,3}$- and O K-edges.

3.3 RESULTS

Spinel-type $LiMn_2O_4$ was first electrochemically delithiated according to methods detailed in the chapter 2. Powder X-ray diffraction of the precursor and oxidized product confirms their purity and the preservation of the initial cubic unit cell symmetry upon delithiation (Figure 16). Pawley fitting of diffraction peaks produced lattice parameters (a) of $LiMn_2O_4$ and $Li_xMn_2O_4$ to be equal to 8.229 and 8.043 Å, respectively. Assuming that Li^+ cations are removed while Mn^{3+} species are oxidized to Mn^{4+}, the composition of the delithiated spinel is $Li_{0.15}Mn_2O_4$ when comparing lattice parameters to literature values.[14] Additionally, a charging capacity of 123 mAh g^{-1} was observed, indicating that the majority of Li had been deintercalated (Figure 17). For brevity, this delithiated working electrode will now be referred to as Mn_2O_4 throughout the chapter. Scanning electron microscopy revealed particle sizes were between 100 – 1000 nm with irregular morphologies (Figure 18).
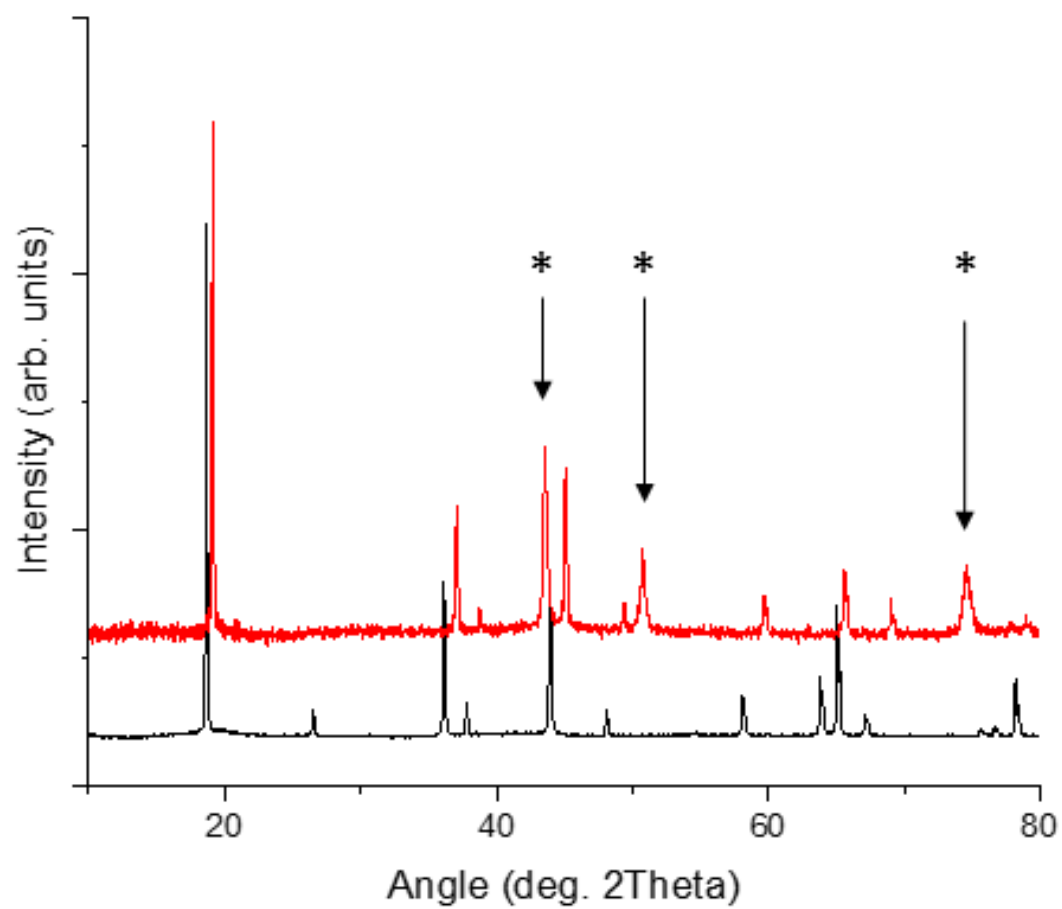
Figure 16. Powder X-ray diffraction (PXRD) of cubic spinel $LiMn_2O_4$ (black) and Mn_2O_4 (red). Asterisks (*) mark diffraction peaks of stainless steel mesh current collector.
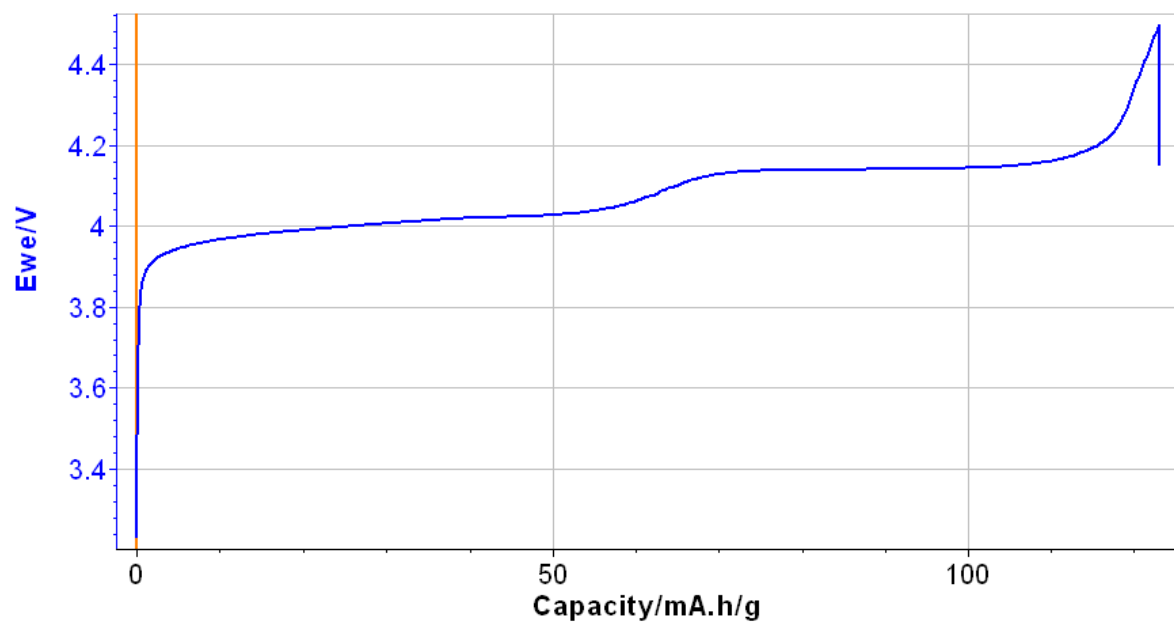
Figure 17. Galvanostatic charging of cubic spinel LiMn$_2$O$_4$ to completely remove Li from the structure.
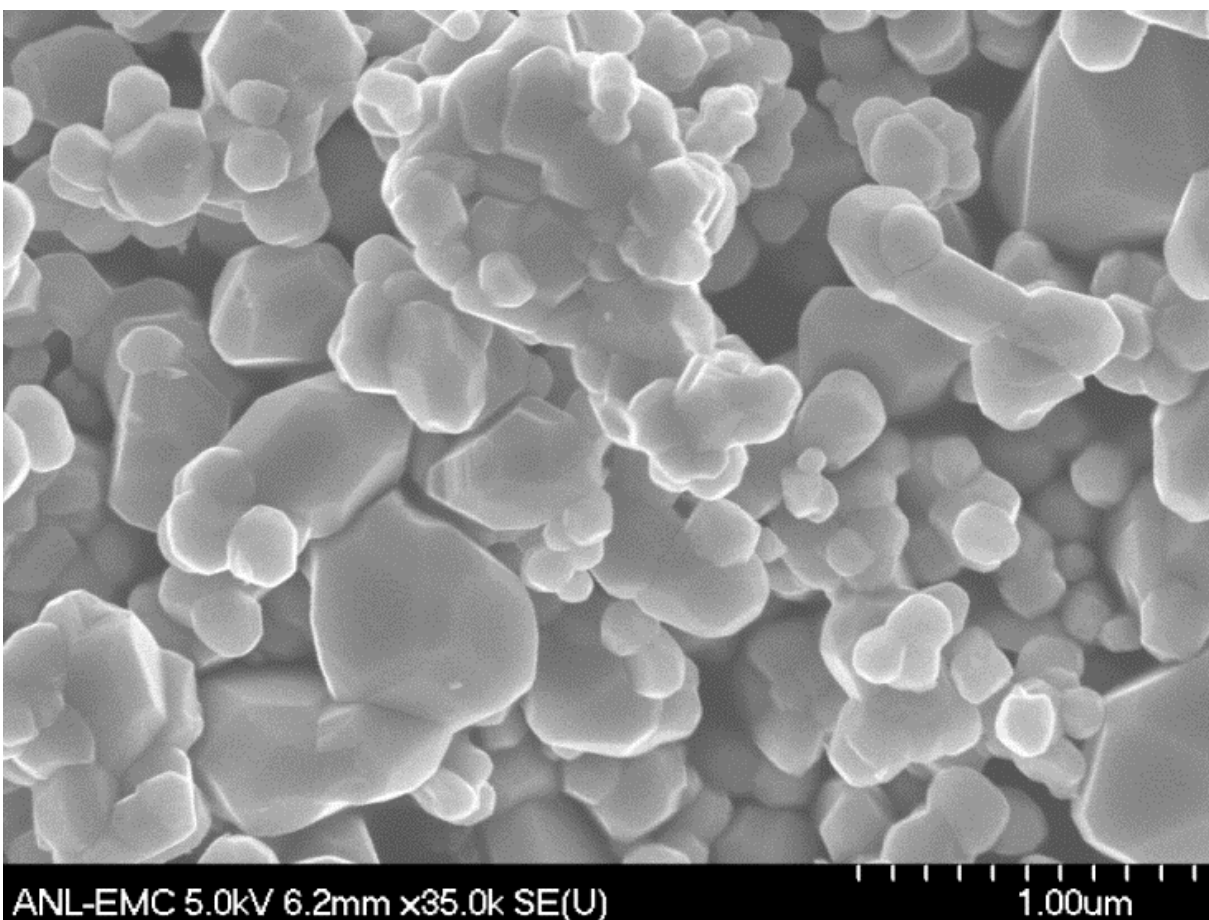
Figure 18. SEM image of parent spinel LiMn$_2$O$_4$ purchased from NEI Co.

It is worth noting that the choice of pH of the electrochemical experiments is driven by the need to have free hydrated M^{2+} ions in solution in order to favor intercalation. The presence of oxoanions that form, for instance, when Zn^{2+} solutions are taken to pH above 10, as in traditional alkaline batteries, would require stripping strongly bound O^{2-} or (OH)$^-$ anions to produce free cations, a process that would introduce a significant and unnecessary barrier. Electrochemical reactions in aqueous Ca^{2+} electrolyte were performed in three-electrode beaker cells. Spinel Mn$_2$O$_4$ powder was cast onto stainless steel mesh. The electrodes were first charged/oxidized to 1.0 V vs. SCE (4.3 V vs. Li$^+$/Li^0) at a charge rate of C/20 to completely remove residual cations prior to reductions. Then, the spinel host was galvanostatically

44

reduced in basic Ca^{2+} electrolyte (pH = 9.17) at a slower current rate of C/40 to improve cation insertion, as shown in Figure 19a. Between -0.1 and -0.4 V *vs*. SCE, a discharge capacity of 597 mAh g^{-1} was observed. Nearly half of the observed reduction occurred at -0.1 V *vs*. SCE (~ 3 V *vs*. Ca^{2+}/Ca^0). On the other hand, in slightly acidic Ca^{2+} electrolyte (pH = 5.45), an unending cathodic event was observed at approximately ~ 0 V *vs*. SCE (~ 3.1 V *vs*. Ca^{2+}/Ca^0), which was manually terminated (Figure 20a) after capacity of 350 mAh g^{-1} was reached. Cubic spinel Mn_2O_4 hosts were also reduced in Zn^{2+} electrolytes (pH = 5.3) to -0.4 V *vs*. SCE at discharge rate of C/40. During this experiment, reduction showed a sloping voltage region between 0.2 and -0.4 V *vs*. SCE (average voltage -0.2 V *vs*. SCE or 0.9 V *vs*. Zn^{2+}/Zn^0) accompanied by a specific capacity of 25 mAh g^{-1} (Figure 19b). The cell was kept at -0.4 V *vs*. SCE (0.7 V *vs*. Zn^{2+}/Zn^0) until 90 mAh/g was observed. Experiments conducted without addition of KOH produced similar capacities, but at slightly higher potentials (Figure 20b).
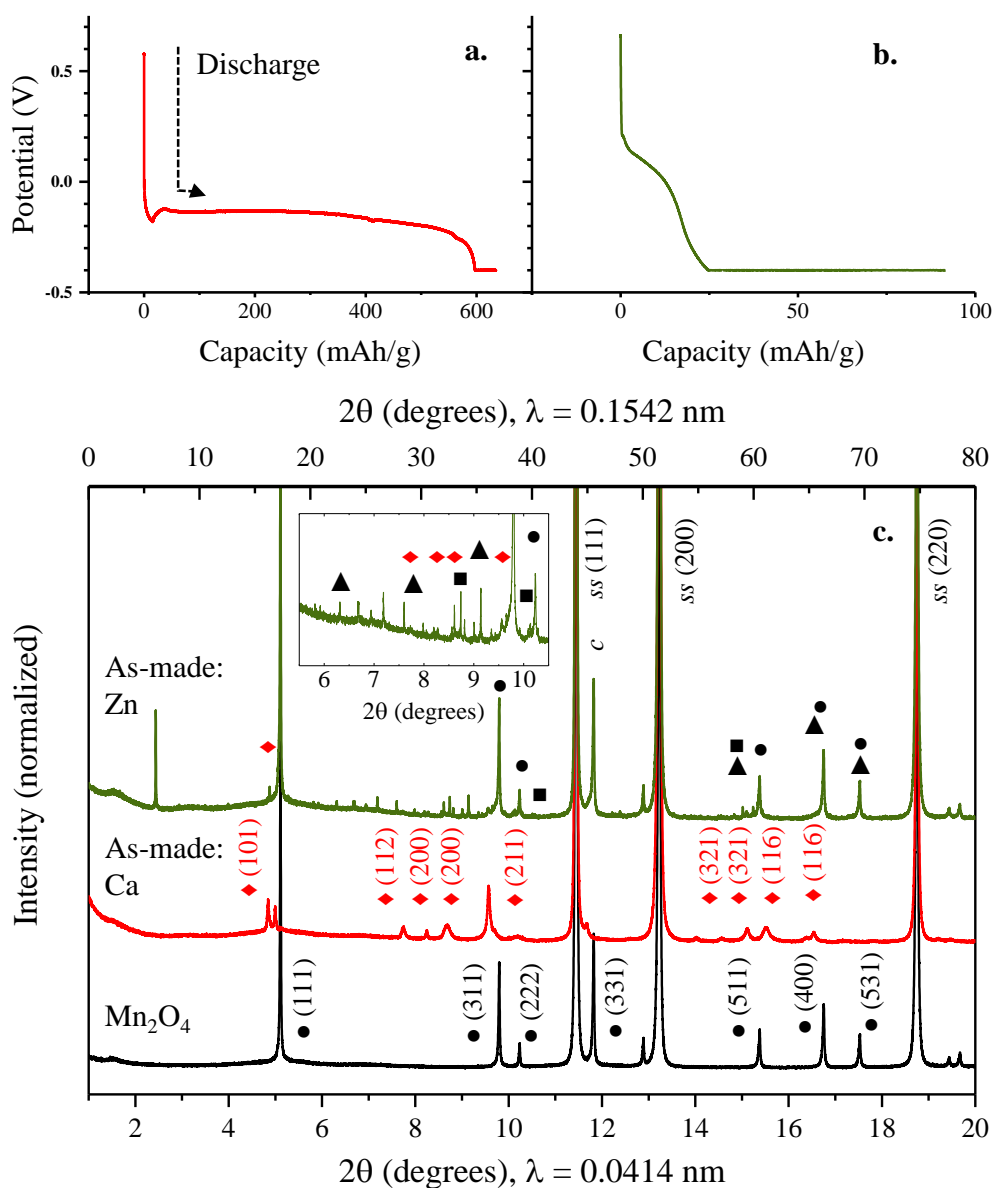
Figure 19. Voltage profiles for the electrochemical reduction of Mn_2O_4 in KOH-titrated (a) Ca^{2+} and (b) Zn^{2+} aqueous electrolytes at rate of C/40. (c) Synchrotron powder X-ray diffraction of spinel Mn_2O_4: pristine (black), reduced to -0.4 V *vs.* SCE in either Ca^{2+} (red) or Zn^{2+} (green) electrolyte. An upper *x*-axis is shown to illustrate the corresponding 2θ values with respect to an X-ray with average wavelength ($λ_{avg}$) of 0.1542 nm (Cu Kα). Circles (●) correspond to cubic spinel Mn_2O_4, diamonds (♦) correspond to tetragonal spinel Mn_3O_4, *s.s.* represents the stainless-steel substrate, squares (■) correspond to ZnO and triangles (▲) correspond to $Zn_2Mn_3O_8$. The inset represents a zoomed view of the host reduced in Zn^{2+} electrolyte between 5 – 10 degrees (λ = 0.0414 nm).

46
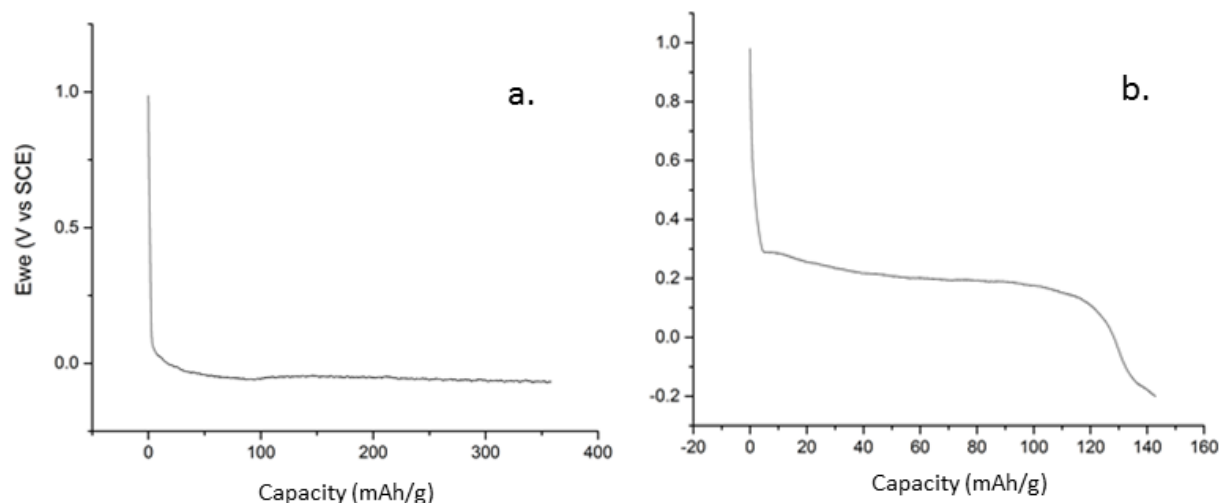
Figure 20. Voltage profiles for the electrochemical reduction of Mn_2O_4 in slightly acidic Ca (a) or Zn (b) electrolytes.

Synchrotron powder X-ray diffraction was used to probe the structural changes of the working electrode upon reduction. A sample collected after a reduction to -0.4 V vs. SCE in basic Ca^{2+} electrolyte showed a significant loss of crystallinity, with the development of new crystallographic planes associated with a tetragonal spinel (Figure 19c). The peak positions were close, but did not exactly match Mn_3O_4 (PDF 01-080-0382). This new phase appeared to replace peaks of the parent cubic spinel, although a peak that could be associated with the (111) reflection, below 18°, 2θ (λ = 1.542 Å), remained. A similar cubic-to-tetragonal structural transformation was observed in the case of electrochemical reduction in slightly acidic Ca^{2+} electrolyte (Figure 21). A significantly more complex array of phases emerge upon reduction of the Mn_2O_4 in a Zn^{2+} electrolyte (Figure 19c and Figure 21). The parent cubic spinel structure was identified as major phase. Minor phases were identified as well, including ZnO (PDF 01-077-9355),

Zn$_2$Mn$_3$O$_8$ (PDF 00-032-1472), and a tetragonal spinel, which could not be resolved between Mn$_3$O$_4$ (04-007-4366) and ZnMn$_2$O$_4$ (PDF 01-071-2499). Some unidentified peaks remained. The appearance of a low angle diffraction peak (approx. 6°, λ = 1.542 Å) was especially significant. This peak corresponds to a *d*-spacing of 14.7 Å. While this peak could not be associated with a specific phase, it was likely the result of a transformation of the cubic spinel into a layered phase, which was accompanied with the incorporation of water between (MnO$_6$)$_\infty$ sheets to lead to large interlayer spacings.
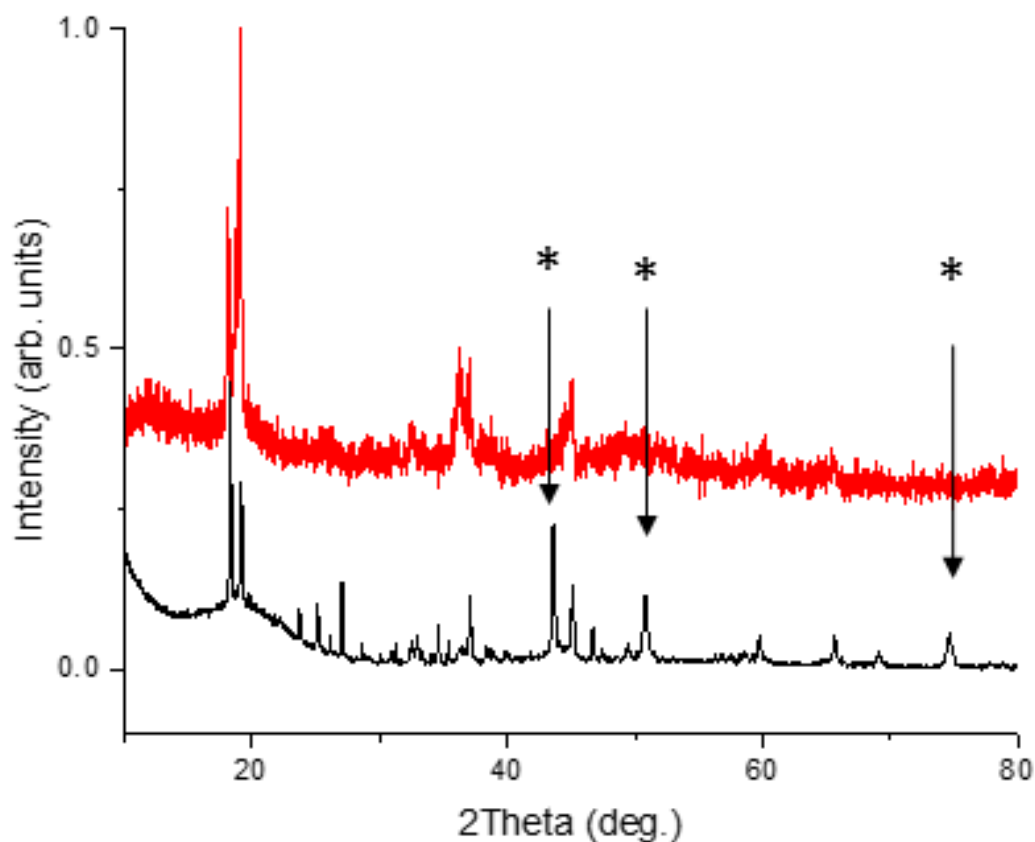
Figure 21. Powder X-ray diffraction of Mn_2O_4 host: pristine (black line) and electrochemically reduced in acidic Ca (red) and Zn (black) aqueous. * denotes stainless steel diffraction peaks from the current collector.

Low magnification TEM images revealed a generalized, yet slight, decrease in particle size, in some cases, to 100 – 500 nm in the longest dimension upon reduction in all electrolytes (Figures 22 and 23), compared to the as-delithiated state. Energy-dispersive X-ray spectroscopy (EDX) was used to determine the presence of divalent species from the electrolyte in the structure. After reduction in basic

Ca^{2+} electrolyte, the EDX map in Figure 22b showed a sparse distribution of Ca in the spinel particle, with a Ca/Mn ratio of less than 1/100 detected (Figure 22e and Table I). The Ca/Mn ratio for pure CaMn$_2$O$_4$ should be 1/2, far higher than the value detected. However, atomic resolution imaging revealed occupancy of the tetrahedral sites of the spinel structure (Figure 24). In turn, TEM-EDX images of Mn$_2$O$_4$ hosts reduced in a Zn electrolyte supported the formation Zn-containing solid species (Figure 22d). Quantification of the EDX signals in Figure 22f resulted in Zn/Mn = 0.17 (Table I), compared to a ratio of 0.5 expected for ZnMn$_2$O$_4$. Furthermore, there were many instances in which Zn and Mn were not located in the same particle. Instead, small domains containing Zn phases were found to form adjacent to the Mn-rich, Zn-free particles.
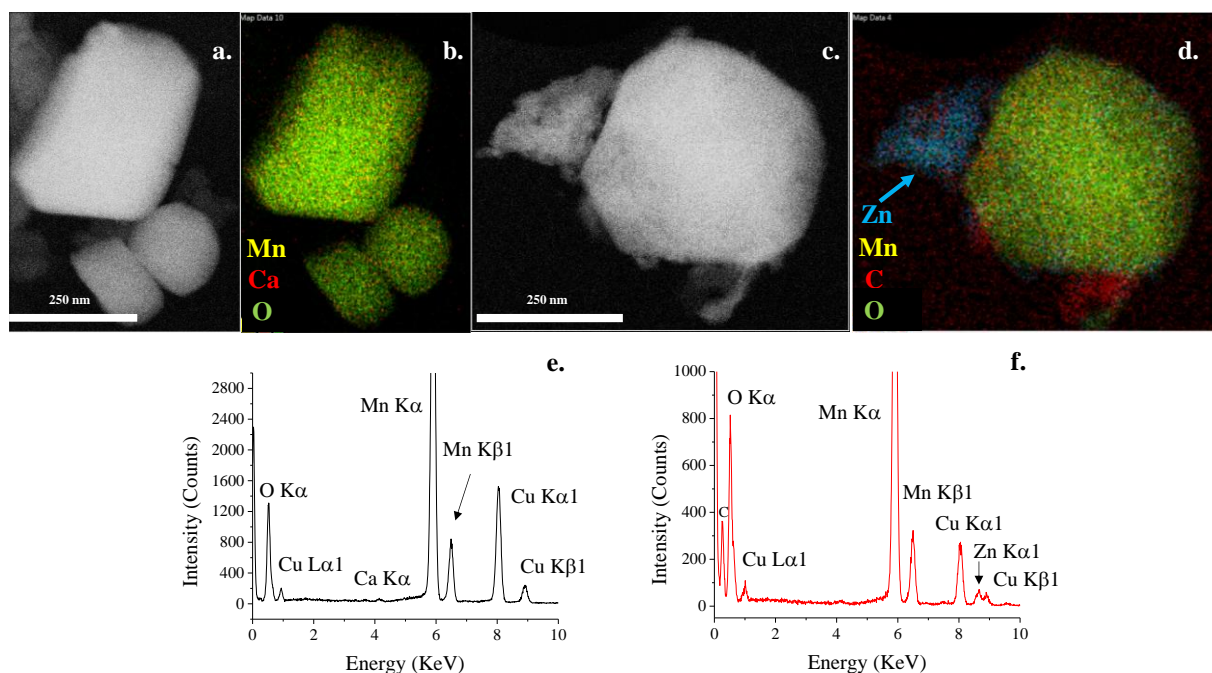
Figure 22. TEM image (a, c) with elemental map by EDX (b, d) of Mn$_2$O$_4$ reduced in KOH-titrated (a, b) Ca^{2+} or (c, d) Zn^{2+} electrolyte, respectively. EDX spectra of Mn$_2$O$_4$ reduced in acidic (e) Ca^{2+} or (f) Zn^{2+} electrolyte; corresponding TEM images are shown in Figure 23.
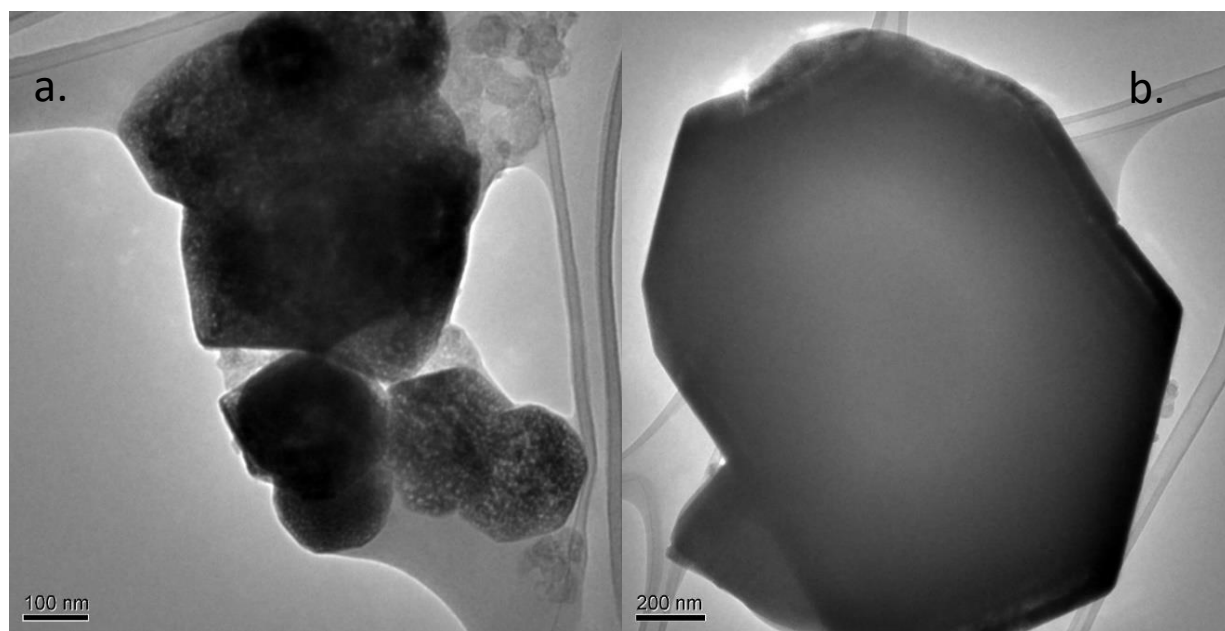
Figure 23. TEM image of reduced spinel Mn_2O_4 (a) in acidic 1 M $Ca(NO_3)_2$ and (b) 1 M $Zn(NO_3)_2$ aqueous electrolytes.
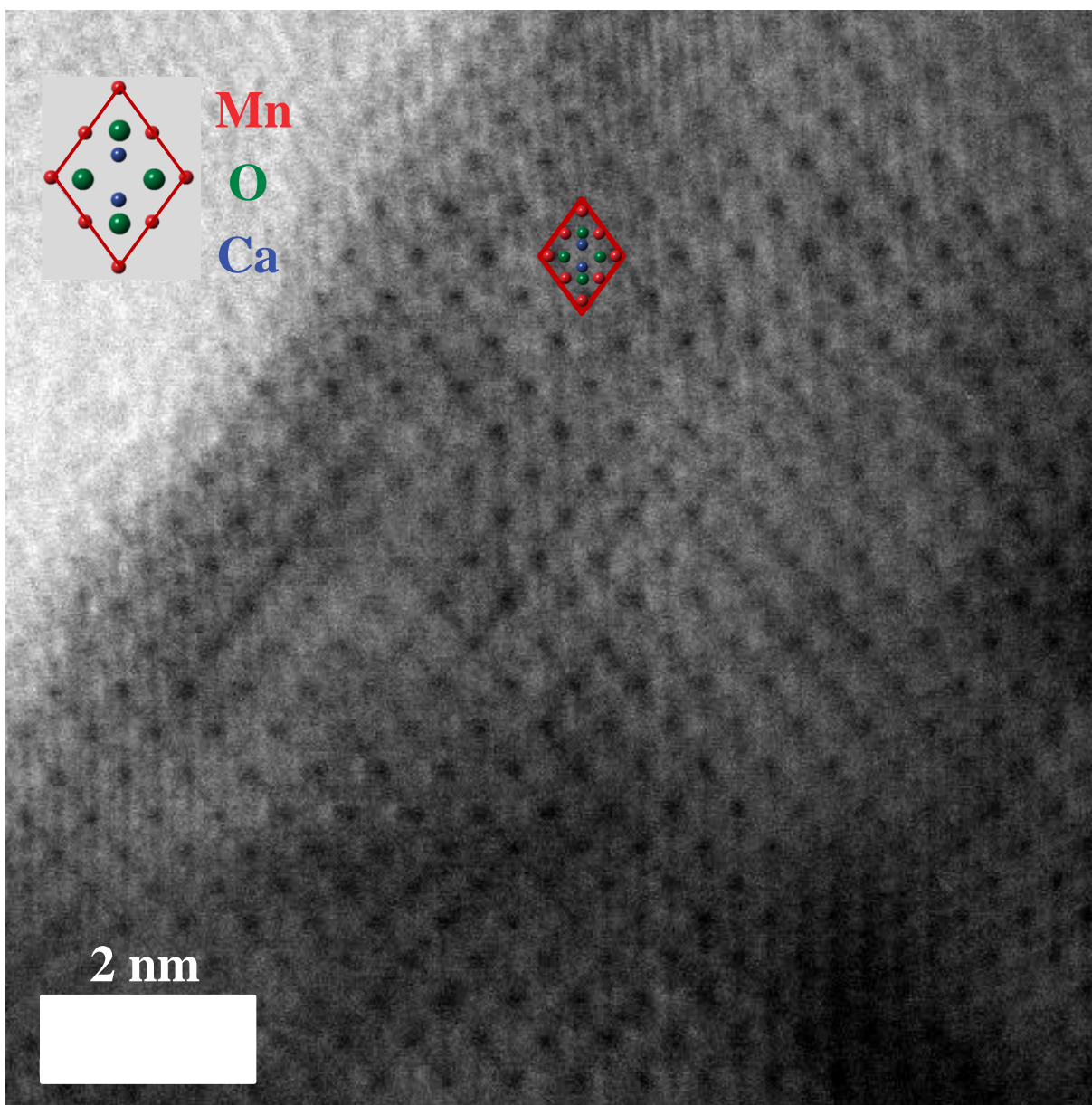
Figure 24. Representative image of Mn_2O_4 reduced in basic Ca^{2+} electrolyte collected with high resolution annular bright field scanning transmission microscopy.

Table II. Results of the EDX analysis of spinel Mn_2O_4 reduced in Ca or Zn electrolytes, leading to the spectra shown in Figure 22. The values correspond to the % of each atom compared to the total atomic content.

	At% Mn	At% Ca	At% Zn
Discharged in Ca electrolyte	17.55	0.16	--
Discharged in Zn electrolyte	16.78	--	2.77

X-ray absorption spectroscopy at the Mn L-edge surveys the chemical state of Mn over a large sample size and depth by characterizing $2p$ electron transitions to unfilled $3d$ orbitals. Both electron (Figure 25a) and fluorescence (Figure 26a) yields were detected. Electron yield corresponds to chemical states within the first few nanometers below the surface of the particle. On the other hand, chemical states within further depths of the particle (so-called "bulk") are detected from fluorescence yield. Mn L-edge spectra of spinel-type Mn_2O_4 and Mn_3O_4 (Figure 25a) showed characteristic L_2 and L_3 absorption events.[15-17] Mn_2O_4 showed two strong absorption features at 641 and 643.7 eV in the L_3 region and a large L_2 absorption event with a peak center of gravity around 654 eV, typical of a Mn^{4+} state.[16,17] In the case of Mn_3O_4, a small feature at 638 eV was followed by a series of five absorption lines at the L_3 edge, accompanied by a large L_2 peak with a shoulder at 651 eV and a center of gravity near 654 eV. The strong feature at 640.3 eV is due to the presence of Mn^{2+} in the compound.[16,17] Reduced Mn_2O_4 hosts in either basic Ca^{2+} or Zn^{2+} electrolytes showed five L_3 absorption features between 640 and 645 eV, with a small shoulder at low energies (638.8 eV), followed by a large L_2 peak with a center of gravity near 653 eV, and a shoulder near 652 eV. Comparison with Mn_3O_4 revealed significant similarities in the distribution of peaks, but the corresponding distribution of intensities differed. The highest intensity was centered at 542.5 eV, which is typical of Mn^{3+} states. Nonetheless, the Mn^{2+} feature at 640.3 eV was significantly stronger compared to what would be expected for a compound solely with Mn^{3+}, such as AMn_2O_4 (A=Ca, Zn).[16,17] The similarities between the X-ray absorption spectra of reduced host and spinel Mn_3O_4 indicate

that the chemical states of Mn are related in the surface region. The fact that the spectra do not perfectly overlay could also partly be due to the presence of unreacted Mn_2O_4 and, in the case of Zn, the formation of other Mn-containing phases (e.g., $Zn_2Mn_3O_8$). Compared to the electron yield spectra, the features in the Mn *L*-edge XAS measured with a fluorescence yield detector (Figure 26a) were significantly washed out due to self-absorption, especially at the L_3 edge, which showed rather low intensity. Nonetheless, the center of gravity of both reduced Mn_2O_4 in basic Ca^{2+} or Zn^{2+} electrolytes and Mn_3O_4 show L_3 and L_2 peaks with centers of gravity near 642 and 652 eV, respectively, indicating that the chemical similarity extended to the bulk of the materials.
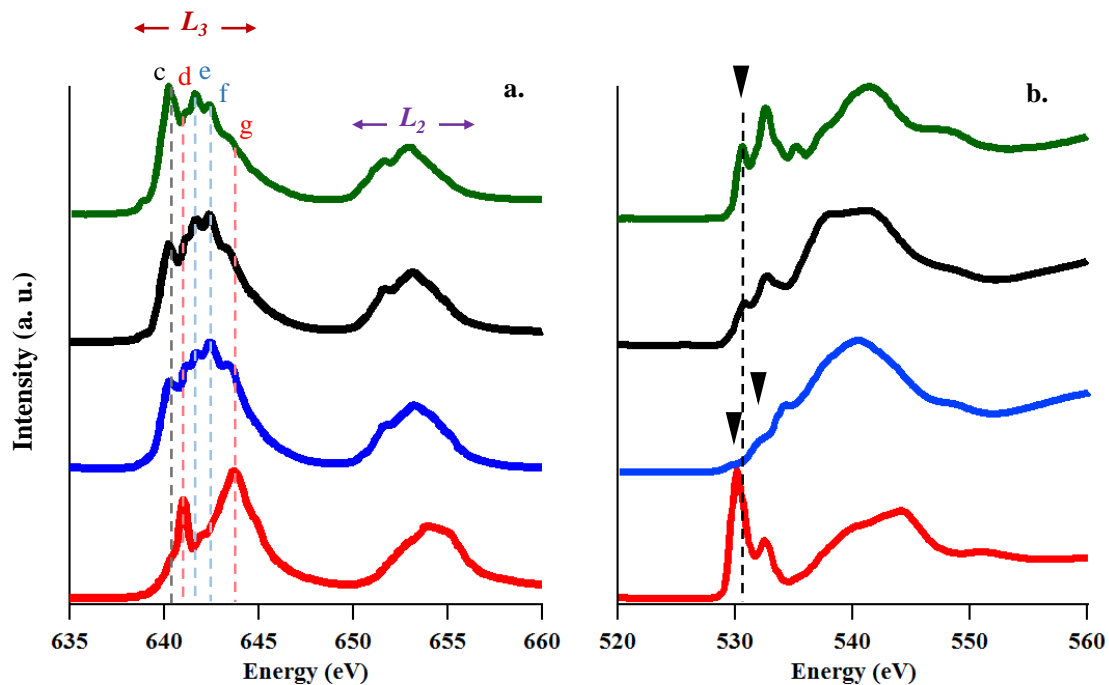
Figure 25. (a) Mn $L_{2,3}$-edge and (b) O K-edge XAS spectra, determined from total electron yields, of spinel Mn_2O_4 host (red), the host reduced in KOH-titrated Ca^{2+} (blue) and Zn^{2+} (black) electrolytes and tetragonal spinel Mn_3O_4 (green). Absorption events characteristic of Mn oxidation states of 2+ (c), 3+ (e, f) and 4+ (d, g) have been labeled. Spectra are shown after multiple loss events and background has been subtracted.
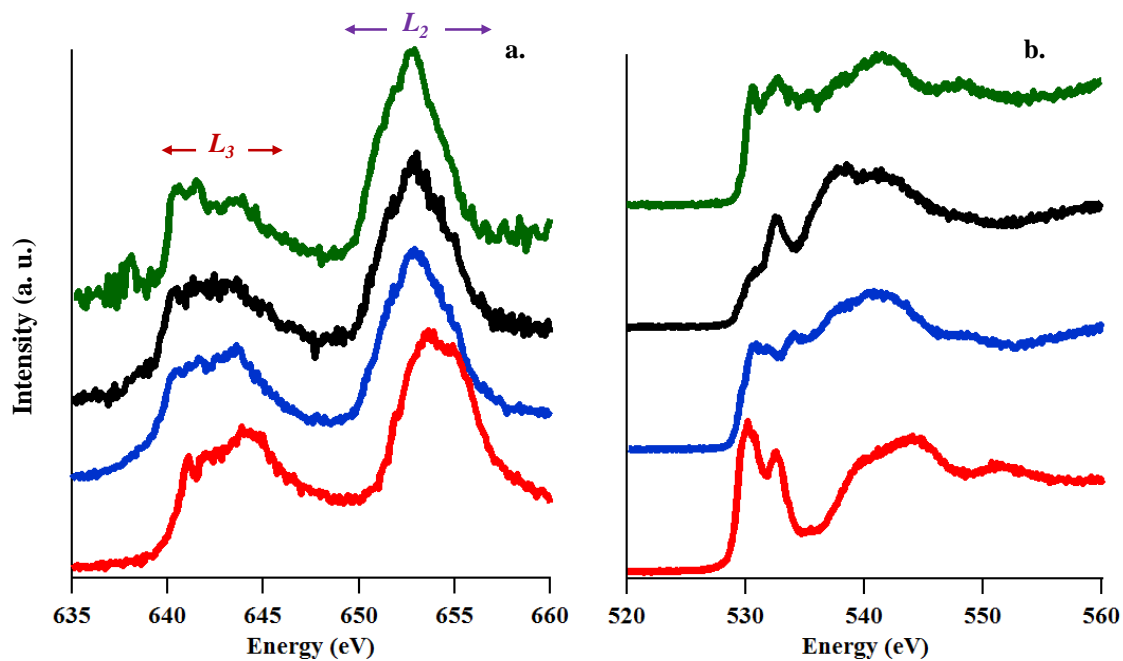
Figure 26. (a) Mn $L_{2,3}$-edge and (b) O K-edge XAS spectra, determined from total fluorescence yields, of spinel Mn_2O_4 host (red), the host reduced in KOH-titrated Ca^{2+} (blue) and Zn^{2+} (black) electrolytes and tetragonal spinel Mn_3O_4 (green).

X-ray absorption at the O K-edge was also detected by electron (Figure 25b) and fluorescence (Figure 26b) yields. According to Figure 25b, pre-edge absorption events, as marked with triangles, occurring below 535 eV result from electronic transitions from O $1s$ core states to $2p$ states hybridized with Mn $3d$ orbitals, the splitting of which is induced by the ligand field and exchange energy. Two typical pre-edge peaks were observed for the spinel Mn_2O_4 host at 530.2 and 532.7 eV; resulting from the high content of octahedral Mn^{4+}.[17,18] However, three pre-edge peaks were observed for Mn_3O_4 at 530.8, 532.8, and 535.6 eV. This splitting is attributed to the excitation transitions to electron t_{2g}-down, e_g-up, and e_g-down states for Mn^{3+}. The main absorption edge is defined by transitions from O $1s$ core states to

56

2p states hybridized with Mn 4s/p orbitals. It was found at higher energy for Mn_2O_4 than Mn_3O_4, consistent with the increase in oxidation state.[17] When accounting for self-absorption, the spectra collected through fluorescence yield were very similar (Figure 26b), indicating good chemical correspondence between surface and bulk.

The Mn_2O_4 electrode reduced in basic Ca^{2+} electrolyte showed a splitting of the pre-edge region into three features, but their intensities were very low, especially compared to Mn_3O_4 (Figure 25b). The pre-edge states overlapped with the main absorption edge, which also appeared at lower energy than Mn_3O_4, leading to a rather broad spectrum overall. In contrast, three reasonably well resolved features were clearly visible in the pre-edge of the fluorescence yield spectrum (Figure 26b). While the increased pre-edge intensity was not distributed among the three features exactly like in Mn_3O_4, the main absorption edge of the reduced sample appeared at energy close to the tetragonal spinel oxide. The significant differences in the O K-edge spectra between surface and bulk clearly indicate that the reduction was not homogeneous throughout the material. In the case of the spinel working electrode reduced in a Zn^{2+} electrolyte, the spectrum collected with the electron yield detector showed a pre-edge region split into 2 peaks (Figure 25b), with the second peak being higher than the first. The intensity of the pre-edge region and the position of the main absorption edge were both lower than in Mn_3O_4. These differences remained in the spectrum collected through fluorescence yield (Figure 26b), indicative of chemical continuity between surface and bulk for the Mn_2O_4 working electrode reduced in Zn^{2+} electrolyte.

3.4 DISCUSSION

No differences were observed in the reactions based on whether KOH was added to the electrolyte to minimize Mn dissolution. Only the results with addition of small amounts of KOH are discussed. In theory, electrochemical intercalation of Ca^{2+} into Mn_2O_4, to form spinel $CaMn_2O_4$, would result in a capacity of 250 mAh g^{-1} with average voltages of approx. 3.2 V $vs.$ Ca^{2+}/Ca^0.[4] During electrochemical reduction of Mn_2O_4 with Ca^{2+} electrolytes resulted in unusually large capacities with cathodic events occurring at approximately 3 V $vs.$ Ca^{2+}/Ca^0. While the operating voltages are close to the theoretically correct potential, the larger capacities than theoretically expected are indicative of competing side

57

reactions. The reduction reaction resulted in a loss of crystallinity of the Mn_2O_4 host and a conversion to a tetragonal spinel, consistent with the formation of Mn^{3+}, a Jahn-Teller active (d^4, high spin) ion that cooperatively elongates of the $3d_z^2$ orbitals in the octahedral coordination. Tetrahedral site occupancy in a hypothetical spinel oxide ($A^{tet}B_2^{oct}O_4$) was confirmed by atomic resolution imaging of the working electrode reduced in basic Ca^{2+} electrolyte. However, EDX revealed that practically no Ca^{2+} cations were inserted present in the material. Furthermore, the formation of both Mn^{3+} and Mn^{2+} species revealed by XAS would not be consistent with the formation of $CaMn_2O_4$, which should only contain Mn^{3+}. Neither the cell parameters nor the Mn^{2+}/Mn^{3+} ratio quite matched the tetragonal spinel Mn_3O_4. More specifically, the reduced phase was richer in Mn^{3+} than Mn_3O_4. The theoretical reduction from Mn_2O_4 to Mn_3O_4 implies the formation of O vacancies, which likely suffer from slow kinetics at room temperature. Consequently, it is possible that the reaction was not completed to form Mn_2O_{4-x}, with ($x < 4/3$). In this scenario, reduction of Mn was not complete, giving rise to a defective structure, which may incidentally have interesting physical properties. The difference in extent of reduction between bulk and surface revealed by spectroscopy is consistent with a process with kinetics limited by solid state diffusion.

Theoretical predictions suggest that intercalation of Zn^{2+} into Mn_2O_4 to form $ZnMn_2O_4$ would result in a capacity of 225 mAh g^{-1} with an average voltage of approx. 1.7 V $vs.$ Zn^{2+}/Zn^0.[4] Small capacities were observed for the reduction of Mn_2O_4 in Zn^{2+} electrolytes at potentials below 1 V $vs.$ Zn^{2+}/Zn^0. However, in addition to the parent cubic spinel phase, additional minor phases, ZnO, $Zn_2Mn_3O_8$ and a tetragonally distorted spinel, were identified. The XRD data was also indicative of other phases that could not be matched to any patterns in the existing databases. A low angle diffraction peak was also identified that corresponds to a d-spacing of 14.7 Å, likely indicative of a hydrated layered phase. The existence of particles containing only either Zn or Mn, is clear indication that reduction of Mn_2O_4 in Zn electrolytes, while possible according to the XAS results, does not proceed through intercalation reactions in the conditions attempted. The presence of larger amounts of Zn compared to Ca systems is consistent with the formation of a variety of phases containing the transition metal. It is important to note that the situation presented here differs notably from when Mn_2O_4 is reduced in Mg^{2+} in otherwise the same

conditions, where evidence of Mg^{2+} incorporation into the spinel structure was convincing.[7] While the intercalation of Ca^{2+} into a tetrahedral site could be considered unlikely given its large size of 1 Å, Zn^{2+} (0.74 Å)and Mg^{2+} (0.71 Å) show very similar ionic radii.[69] The origin of their different behavior remains to be ascertained. Reversible Zn^{2+} deintercalation has been claimed in spinel-type $ZnMn_{2-x}\square_xO_4$ ($\square$ = octahedral site vacancy) in 3 M aqueous $Zn(CF_3SO_3)_2$ electrolyte.[12] However, it is worth noting that this claim is based on a very small decrease in the cell parameter of the spinel structure, which maintains the tetragonal distortion. This observation indicates that significant amounts of Mn^{3+} remained in the structure, which is supported by the small changes in Mn L-edge XAS, especially when compared with the Mn^{4+} spectrum of Mn_2O_4 reported here. Therefore, the hypothetical levels of reversible Zn deintercalation were small and inconsistent with large specific capacities. However, it is possible that the aqueous electrolytes used in that report, which contain a different salt at a much higher concentration, prevent Mn dissolution reactions that create reactions conditions that favor intercalation.

Nudged elastic band calculations predicted that the energy barriers of Ca^{2+} migration between tetrahedral sites in the Mn_2O_4 spinel structure are low enough to be comparable to Li^+.[40] However, experimental observations in this chapter contradict this expectation. Unlike Li^+, Ca^{2+} does not intercalate into the spinel structure. This could be related to the fact that the ionic radius of Ca^{2+} (1 Å) is larger than Li^+ (0.73 Å) and that the lowest coordination number of Ca^{2+} is 6.[69] Furthermore, Mg^{2+} and Zn^{2+} were predicted to have higher energy barriers of cation migration compared to Ca^{2+},[40] with Zn^{2+} being higher than Mg^{2+}. In this case, both divalent ions are stable in the tetrahedral site. The predicted trend for these two ions is consistent with experimental observations, as Mg^{2+} has been observed to intercalate electrochemically, but, as presented in this chapter, the same reaction is not possible for Zn^{2+} in the same conditions.[47] The origins for this trend are unclear, since they have the same oxidation state and similar ionic radii, so they are worthy of further investigation.

3.5 CONCLUSIONS

The reduction of cubic spinel Mn_2O_4 was evaluated in 1 M aqueous Ca^{2+} or Zn^{2+} electrolytes. The addition of basic solutions had no influence on the outcomes. Electrochemical reduction in Ca^{2+} electrolytes was proved by spectroscopy. While it resulted in the complete transformation from a cubic to a tetragonal spinel lattice, there was no simultaneous incorporation of Ca^{2+}. Similar experiments conducted in Zn^{2+} electrolyte showed a partial structural transformation to a tetragonal spinel, along with ZnO and $Zn_2Mn_3O_8$ phases, inferring Zn^{2+} insertion, with new Zn-only phases preferentially formed adjacent to Mn-rich particles. In both cases, the results were different from previous experimental work in similar Mg^{2+} electrolytes, suggesting that its intercalation into the spinel oxide is more favorable than Ca^{2+} and Zn^{2+}. This work highlights the importance of properly characterizing the results of reactions when exploring multivalent chemistries, preferably with a combination of structural and electronic probes in order to accurately define the identity of the products.

4 CONTROL OF SIZE AND COMPOSITION OF COLLOIDAL NANOCRYSTALS OF MANGANESE OXIDE

4.1 INTRODUCTION

With the turn of the century, nanocrystals of manganese oxide have been touted for a variety of applications, such as wastewater treatment, magnetic imaging, catalysis, sensors, supercapacitors and rechargeable batteries, justified by the unique properties triggered at small sizes.[49,70–72] Specifically, in the case of batteries, the short lengths for diffusion of charge carriers enable faster kinetics of reactions in high capacity electrodes.[73,74] Such short lengths could be critical to enable battery concepts based on the intercalation of multivalent ions, such as Mg^{2+}, because of the high activation barriers and, thus, low coefficients for diffusion of these highly charged species. As a representative example, reversible, yet sluggish, intercalation of Mg^{2+} into spinel-type Mn_2O_4 was observed in micron-sized particles.[47] Motivated by computational studies suggesting that divalent cations could migrate sufficiently well in spinel lattices to sustain reversible electrochemical reactions at very small crystal sizes,[51] our group synthesized $Mg_{0.5}Mn_{2.5}O_4$ nanocrystals below 20 nm.[52] The materials were electrochemically active, but the existence of both Mg^{2+} and Mn^{2+} induced site exchange between both cations, resulting in the intercalation of both Mg^{2+} and Mn^{2+}. It was hypothesized that exclusive intercalation of Mg^{2+} could be achieved in stoichiometric, ordered $MgMn_2O_4$, where all of the Mn is in the +3 oxidation state.

Colloidal synthetic methods in the liquid phase provide a pathway to consistently control the particle size, shape and size distribution of nanocrystals.[49,75] In a typical colloidal synthesis, salts of metals are decomposed in high-boiling point surfactant/solvent to yield crystalline dispersions of nanoparticles. However, Mn_3O_4 is the oxide with the highest average oxidation state of Mn (+2.66) reportedly made under colloidal conditions, even in the presence of soft oxidizing agents, such as TMNO·$2H_2O$.[76–80] Given that targeting compounds such as ordered nanoscale $MgMn_2O_4$ clearly

challenges current synthetic capabilities, a comprehensive understanding is required of the effect and limits of chemical parameters on the specific Mn-O phase forming in a colloidal environment.

Several reports exist where formate, acetate, acetylacetonate salts of Mn^{2+} were thermally decomposed in oleylamine or oleylamine-based solvents to obtain nanocrystals of MnO or Mn_3O_4.[77–81] Jiao et $al.$ observed that thermolytic decomposition of Mn^{2+} acetylacetonate $[Mn(acac)_2]$ in oleylamine at 210 °C, while exposed to normal atmosphere, resulted in nanocrystals of Mn_3O_4 capped with an Mn^{4+} shell.[77] The shell of Mn^{4+} was ascribed by the authors to the presence of O_2 in the atmosphere. In contrast, other groups conducted reactions protected from unwanted O_2 and H_2O by flowing a blanket of inert gas (N_2 or Ar) over the ongoing reaction, enhanced by evacuating the reaction vessel. Nanocrystals of pure Mn_3O_4 are reportedly favored when annealing carboxylate precursors of Mn^{2+} under O_2- and H_2O-free conditions at temperatures from 100 to 250 °C, for up to 10 hours.[78–80] It has been hypothesized that MnO forms initially but is later oxidized by CO_2 to form Mn_3O_4. As a contrast, Seo et $al.$ described the formation of nanocrystals of pure MnO at annealing temperatures of 220 – 250 °C. In this case, the reactions were conducted with the controlled addition of H_2O within the same general conditions.[78] The authors argued that the presence of H_2O prohibits oxidation of MnO to Mn_3O_4. In yet a separate study, Zhang et $al.$ reported that annealing Mn^{2+} acetate $[Mn(OAc)_2]$ at 250 °C, without H_2O, could result in the formation of nanocrystals of either mixed phase Mn_3O_4/MnO or pure MnO, depending on the specific heating protocol.[79] In contrast, during the thermolytic decomposition of Mn^{2+} formate at 340 °C, Ould-Ely et $al.$ determined that nanocrystals of pure MnO formed with and without H_2O, generating a seeming contradiction in the literature.[81] This observation is consistent with other studies where formation of crystalline nanocrystals of MnO was found following the thermal decomposition of $Mn(OAc)_2$ in the presence of oleic acid, rather than oleylamine, at 320 °C.[76,82] Most importantly, despite the expected generation of CO_2 upon thermolysis of the carboxylate precursor, these nanocrystals of MnO could only be oxidized to Mn_3O_4 by adding a mild oxidizer, TMNO·2H_2O.[76] This oxidative method was adapted from the seminal work by Hyeon et $al.$ where colloidally prepared nanoparticles of Fe were uniformly transformed to monodisperse Fe_2O_3 by controlled oxidation using the same reagent.[83] Despite this broad

synthetic effort, to date, there has been no systematic study of the decomposition of Mn^{3+} precursors in oleylamine, so the possibility of synthesizing Mn_2O_3 instead of Mn_3O_4 has not be fully probed. Lastly, no report exists of a surfactant-assisted colloidal reaction that produces nanoscale MnO_2 (Mn^{4+}).

With the dual goal of providing a resolution to the conflicting results in the literature described above, and, broadly, evaluate the level of control over Mn oxidation state in colloidal conditions, this report evaluates effects of temperature and oxidizing conditions on products following the thermal decomposition of $Mn(OAc)_2$ and $Mn(acac)_3$ in oleylamine during a one-step heat-up colloidal method. The results provide important insights into the redox activity of transition metals in colloidal synthesis of crystalline metal oxide nanoparticles.

4.2 EXPERIMENTAL METHODS

Details of the synthesis of MnO_x nanocrystals and the methods of characterization are detailed in chapter 2. Materials were characterized by thermogravimetric analysis, differential scanning calorimetry, powder X-ray diffraction and transmission electron microscopy.

4.3 THERMAL DECOMPOSITION OF Mn^{2+} ACETATE

While being heated in a TGA/DSC apparatus in synthetic air, dry powder of Mn^{2+} acetate [$Mn(OAc)_2$] showed a prominent exothermic (-55.5 J) decomposition event at 250 °C (Figure 27a). PXRD was used to determine the crystal structure and quality of the decomposition products. Pawley fits were used to correlate experimental PXRD data to standard crystal structures and determine unit cell parameters. According to the diffraction pattern in Figure 27b, the product of decomposition in synthetic air was pure Mn_3O_4 (space group *I41/amd*, $a = 5.75$ Å and $c = 9.42$ Å) and showed a 56 % reduction in mass (theoretical loss, 56 %). On the other hand, while being heated in N_2 atmosphere, $Mn(OAc)_2$ underwent an endothermic (11.0 J) phase change at 280 °C (Figure 27c). In an inert atmosphere, referring to Figure 27d, pure MnO (space group *Fm-3m*, $a = 4.43$ Å) was produced and was accompanied by an mass reduction of 60 % (theoretical loss, 60 %). Since MnO formed under inert conditions, CO_2 formed from decomposition of the ligand does not oxidize Mn^{2+} to Mn^{3+}, as previously claimed.[80] On the other

hand, in the presence of O_2 in air, decomposition of $Mn(OAc)_2$ will occur through partial oxidation of Mn^{2+} to Mn^{3+} to form Mn_3O_4.
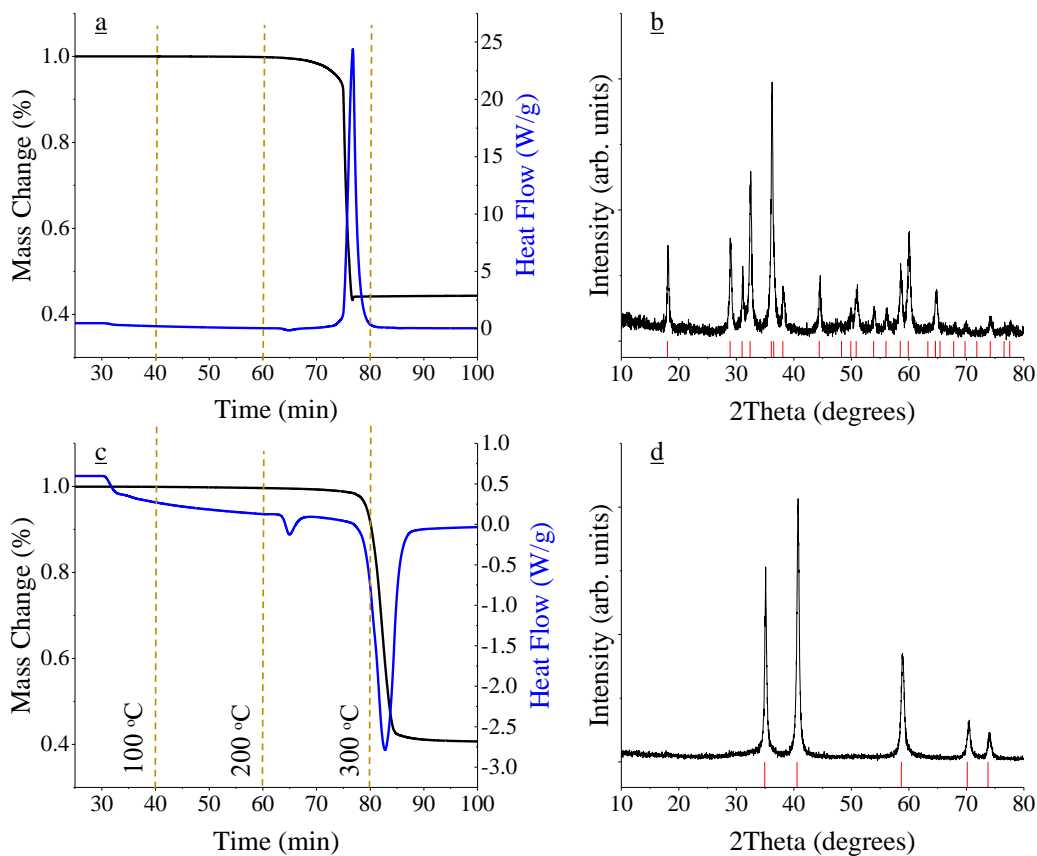
Figure 27. Thermal gravimetric analysis (black line) and differential scanning calorimetry (blue line, exo up) plots following heating of $Mn(OAc)_2$ powder in synthetic air (a) or N_2 (c) atmospheres. Powder X-ray diffraction patterns of the corresponding products of decomposition in synthetic air (b) and N_2 (d) atmospheres are also shown, respectively. Red tick marks correspond to reflections of spinel Mn_3O_4 (b) and cubic MnO (d). Orange dashed lines correspond time of experiment to temperature, where 40, 60, 80 and 84 min are equivalent to 100, 200, 300 and 320 °C.

Manganese oxide nanocrystals were prepared by thermally decomposing $Mn(OAc)_2$ in oleylamine, as described in chapter 2. During a series of "control" thermolysis reactions, the round-bottom flasks (reaction vessels) were purged with N_2 gas and kept air-tight, completely free of O_2 and H_2O, in a Schlenk line. Usually, the reaction solution was transparent with a slight yellow color after a successful degas regimen, which later turned green (sometimes grey). PXRD patterns of the products of the thermal decomposition of $Mn(OAc)_2$ in oleylamine from 200 – 300 °C (Figure 28a) revealed the formation of crystalline MnO, consistent with color changes. MnO is commonly found in nature as the green mineral manganosite. The large peak widths are indicative of the production of nanocrystals. These results indicate that the $Mn(OAc)_2$ preferentially decomposes to form MnO in the absence of O_2 and H_2O, supporting TGA results. No product formed after 1 h of decomposition at 150 °C under inert conditions. Longer reaction times, 6-12 h, were needed to produce crystalline MnO (Figures 28a and 29). The reaction time to form MnO nanocrystals could be reduced to 3 h if the temperature of decomposition was raised by 25 °C to 175 °C (Figure 30a). Zhang *et al.* reported need to decompose $Mn(OAc)_2$ for 10 hours at 100 °C to form highly crystalline nanoparticles of Mn_3O_4.[79] These annealing temperatures are much lower than 280 °C (endothermic event associated with MnO formation in Figure 27c) inferring that colloidal reaction thermodynamics were different than in solvent-free environments, possibly due to the formation of different Mn^{2+} complexes involving oleylamine prior to thermolysis. In turn, long reaction times (slow rates) are likely the result of slow kinetics of decomposition of the precursor, $Mn(OAc)_2$, at temperatures close to the thermodynamic value in these conditions. The results were unexpected since other reports indicate when decomposing Mn^{2+} precursor salts under O_2- and H_2O-free conditions in oleylamine at temperatures of 100 - 250 °C nanocrystals of Mn_3O_4 are produced.[78–80] These reports claim that CO_2, a byproduct of ligand decomposition, acts as the main oxidizing source. The results presented here suggest that CO_2 is insufficiently oxidizing and that inert conditions successfully preserve Mn^{2+} during thermolysis. More than likely, O_2 contaminated these reactions in the literature, favoring the formation of Mn_3O_4.
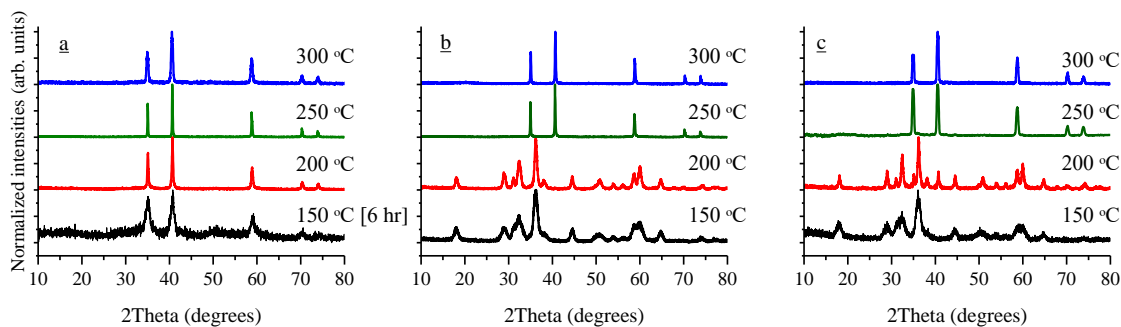
Figure 28. Powder X-ray diffraction of as-prepared nanocrystals following thermal decomposition of $Mn(OAc)_2$ in oleylamine as a function of temperature in, (a) N_2, (b) air or (c) N_2 with TMNO·$2H_2O$. Diffraction peak intensities were normalized. All reactions were carried out for 1 hour, unless otherwise noted.
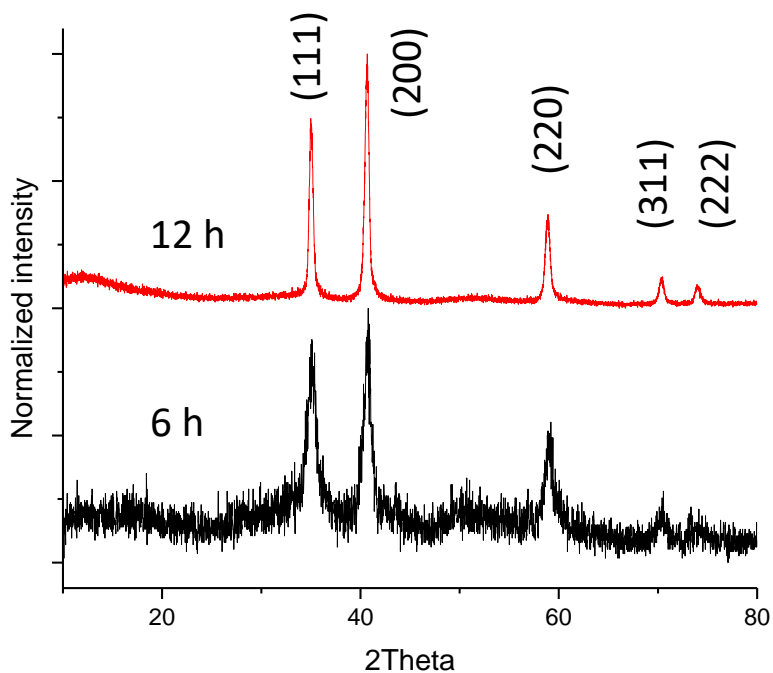
Figure 29. Powder X-ray diffraction pattern of the material produced after thermally decomposing $Mn(OAc)_2$ for six or twelve hours at 150 °C in oleylamine under inert conditions.
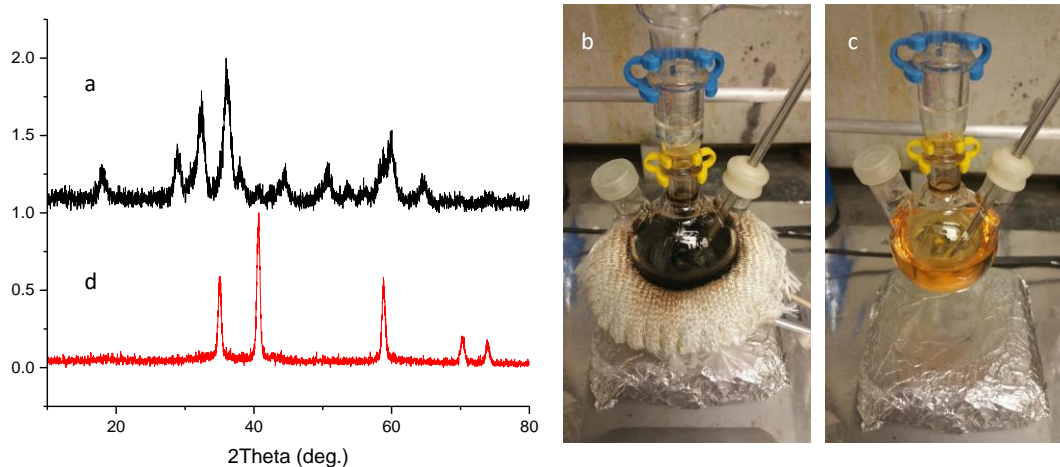
Figure 30. Powder X-ray diffraction pattern (a, d) of the material produced after thermally decomposing Mn(OAc)$_2$ for three hours at 175 °C in oleylamine under inert conditions. The reactions were different in that in (a, b) corresponds to a setup where the reaction was degassed only after reaching 100 °C, the image was taken at 100 °C after Mn(OAc)$_2$ dissolved into oleylamine. The brown colored solution always produced Mn$_3$O$_4$ upon completing annealing at 175 °C. On the other hand, (c, d) the precursor salt was added to oleylamine where the vessel was degassed once at room temperature then heated to 100 °C for regular degassing. Once Mn(OAc)$_2$ dissolved into solution (c), it was transparent and yellow, and annealing at 175 °C resulted in nanocrystals of pure MnO.

The decomposition of Mn(OAc)$_2$ for 3 h at 175 °C under inert conditions was exemplary of the need to carefully control synthetic conditions to produce the desired compound. It was found to be extremely sensitive to the order in which the reaction mixture was prepared in the round bottom flask. Mn$_3$O$_4$ formed when Mn(OAc)$_2$ was first added to the reaction vessel followed by oleylamine and a series of generic thirty-minute degas steps (Figure 30a); the solution turned brown instead of green. Even if a protective N$_2$ blanket was employed, the solution always turned brown by the time Mn(OAc)$_2$, a pink

powder, had dissolved into oleylamine (Figure 30b). The dramatic change of the color of the solution from transparent to an opaque brown at room temperature suggests that the Mn-O-oleylamine complex is sensitive to oxidizing impurities in the vessel, and likely reacted prior to degassing and heating. Zhang *et al.* also observed this phenomenon when they dissolved $Mn(OAc)_2$ into oleylamine.[79] More than likely, O_2 trapped in the salt and under the oleylamine contaminates the reaction and oxidizes the Mn^{2+}-oleylamine complex. Throughout our experiments, we found that adding the precursor salt to the reaction vessel already filled with oleylamine, and under a nitrogen blanket, reduced the presence of Mn_3O_4 in the end-product. Still, the solution would turn brown in some cases, compromising control of the reaction. Therefore, a single degas step at room temperature was added to the synthetic procedure in order to quantitatively remove O_2 and H_2O prior to heating. The degas was considered complete after bumping of the volatile impurities from the reaction mixture stopped; whereupon the solution would turn transparent with a slight yellow color by the time the system reached 100 °C (Figure 30c). Then, crystalline MnO nanoparticles were reproducibly obtained when all these steps were implemented, which were adapted for all other reactions under inert N_2 and N_2 with $TMNO·2H_2O$ (Figures 27a,c and 30d).

A dramatic change in the decomposition of $Mn(OAc)_2$ was observed when the reaction was conducted in air, in the laboratory atmosphere, Mn_3O_4 readily and consistently formed after one hour of decomposition at 150 and 200 °C (Figure 28b). During these experiments, as the precursor salts dissolved into the surfactant, the solution turned brown, as expected from Mn_3O_4. Mn_3O_4 is commonly found in nature as a brown mineral hausmannite. Jiao *et al.* also found that decomposing $Mn(acac)_2$ in oleylamine at 210 °C in air yielded nanocrystals of Mn_3O_4.[77] Oxidation of Mn^{2+} to Mn^{3+}, and subsequent formation of Mn_3O_4, is expected since this product formed after heating $Mn(OAc)_2$ in air in the TGA apparatus (Figure 27b). However, referring back to Figure 28b, MnO was formed when the colloidal reaction was performed in air at 250 and 300 °C. These results indicate Mn^{3+} is only stable at annealing temperatures lower than 250 °C, probably because it oxidizes oleylamine at higher temperature. The critical role of oxidizing agents in the formation of Mn_3O_4 over MnO was further confirmed by decomposing $Mn(OAc)_2$ in oleylamine under N_2 in the presence of $TMNO·2H_2O$, a mild oxidizing agent. In accordance to the

diffraction patterns in Figure 28c, pure Mn_3O_4 formed after annealing for 1 h at 150 °C. A product with

mixed MnO/Mn_3O_4 phases formed after the reaction completed at 200 °C. Finally, pure MnO resulted

from the decomposition at 250 and 300 °C. Exposure to TMNO·$2H_2O$ (Figure 28c) and atmospheric

sources of O_2 (Figure 28b) favor the formation of pure Mn_3O_4 nanocrystals during pyrolysis of $Mn(OAc)_2$

in oleylamine at 150 °C. These results support the notion that Mn^{3+} is stable in the presence of an oxidizer

only at reaction temperatures of 200 °C or less. Oleylamine is known to act as reducing agent at elevated

temperatures.[84] This surfactant contains an anime head that is liable to facilitate a redox event at extreme

conditions. The presence of both phases of MnO and Mn_3O_4 at 200 °C suggests it is the temperature

where a transition to reducing conditions occurs.

The large peak widths observed in the PXRD patterns (Figure 28) allude to the nanocrystalline

nature of the samples, which was confirmed by transition electron microscopy (TEM, Figure 31). At least

300 particles from each colloidal synthesis reaction were measured from the TEM images (Figure 32) to

build histograms (Figure 33) of particle size distributions. From the histograms, average particle sizes and

error (taken as one standard deviation) were calculated, listed in Table II, and plotted in Figure 31a. TEM

images in Figure 31b-e correspond to nanocrystalline products formed after annealing $Mn(OAc)_2$ in

oleylamine in air (see Figure 28b for PXRD). They are representative of all the materials made in the

study (Figure 32).

Figure 31. (a) Size distribution of nanoparticles produced after thermally decomposing $Mn(OAc)_2$ in oleylamine. Squares, diamonds and circles correspond to reactions in N_2, N_2 with $TMNO·2H_2O$ and air. Representative transmission electron microscopy images of products of the reactions under air, at (b) 150, (c) 200, (d 250, and (e) 300 ^{o}C. White scale bars correspond to 50 nm.

300 °C

250 °C

200 °C

150 °C

inert   TMNO   air

Figure 32. Transmission electron microscopy images following thermal decomposition of Mn(OAc)$_2$ in oleylamine for one hour at 150, 200, 250 and 300 °C under inert conditions or oxidized by TMNO·2H$_2$O or air. Scale bars correspond to 50 nm.

Figure 33. Histograms of particle size distribution following thermal decomposition of $Mn(OAc)_2$ in oleylamine for one hour at 150, 200, 250 and 300 °C under inert conditions or oxidized by TMNO ·$2H_2O$ or air. Red, green and black correspond to products' phase identified as pure Mn_3O_4, pure MnO and mixed Mn_3O_4/MnO, respectively.

During the colloidal reactions, temperature had a measurable impact on particle size. While no particles could be collected annealing at 150 °C for 1 h under simply N_2, quasi-cubes of 8 ± 1 and rice-shaped 10 ± 2 nm nanocrystals of Mn_3O_4 were produced in the presence of TMNO·$2H_2O$ and air, respectively (Figure 31a and Table II). Decomposition of $Mn(OAc)_2$ in oleylamine at 150 °C for 6 h resulted in 7 ± 2 nm particles of MnO with quasi-cubic morphology (Figure 34a,b). Similarly, when thermolyzed to 175 °C for 3 h, 8 ± 3 nm particles of MnO formed (Figure 34c,d). Increasing the reaction

72

temperature generally resulted in larger nanocrystals for each heat-up synthesis. Rice-shaped nanocrystals of Mn_3O_4 of 20 ± 6 and 10 ± 5 nm were produced after annealing $Mn(OAc)_2$ at 200 °C in N_2 with TMNO·$2H_2O$ and air, respectively. During the control experiments, 40 ± 8 nm truncated cubes of MnO were formed after one hour of thermolysis of $Mn(OAc)_2$ at 200 °C. Annealing for one hour at 250 °C under inert, TMNO·$2H_2O$ or air-oxidizing conditions resulted in 100 ± 30, 100 ± 100, and 70 ± 60 nm truncated cubes of MnO, respectively. Furthermore, annealing $Mn(OAc)_2$ for one hour at 300 °C under inert, TMNO·$2H_2O$ or air-oxidizing conditions resulted in 70 ± 20, 300 ± 80, and 100 ± 20 nm truncated cubes of MnO, respectively. Large standard deviations from the mean particle size at reactions completed at 250 °C, with TMNO·$2H_2O$ or air, are associated with bimodal size distributions (Figure 33). These bimodal distributions in particle size growth are due to coarsening and/or Otswald ripening where larger nanoparticles grow at the expense of smaller ones. The particle size distributions in this report are all larger than ±5 % of the mean size, which does not satisfy the condition to claim monodispersity.[61] To improve monodispersity during heat-up syntheses, researchers report having to work in highly dilute conditions, add additional solvents/surfactants, or use different annealing/aging treatments.[76,78–80,82,83] These strategies would constitute a worthwhile endeavor for follow-up studies, but were considered beyond the scope of this work, which is to evaluate the level of control over Mn oxidation state in colloidal conditions, and its relationship with crystal size.
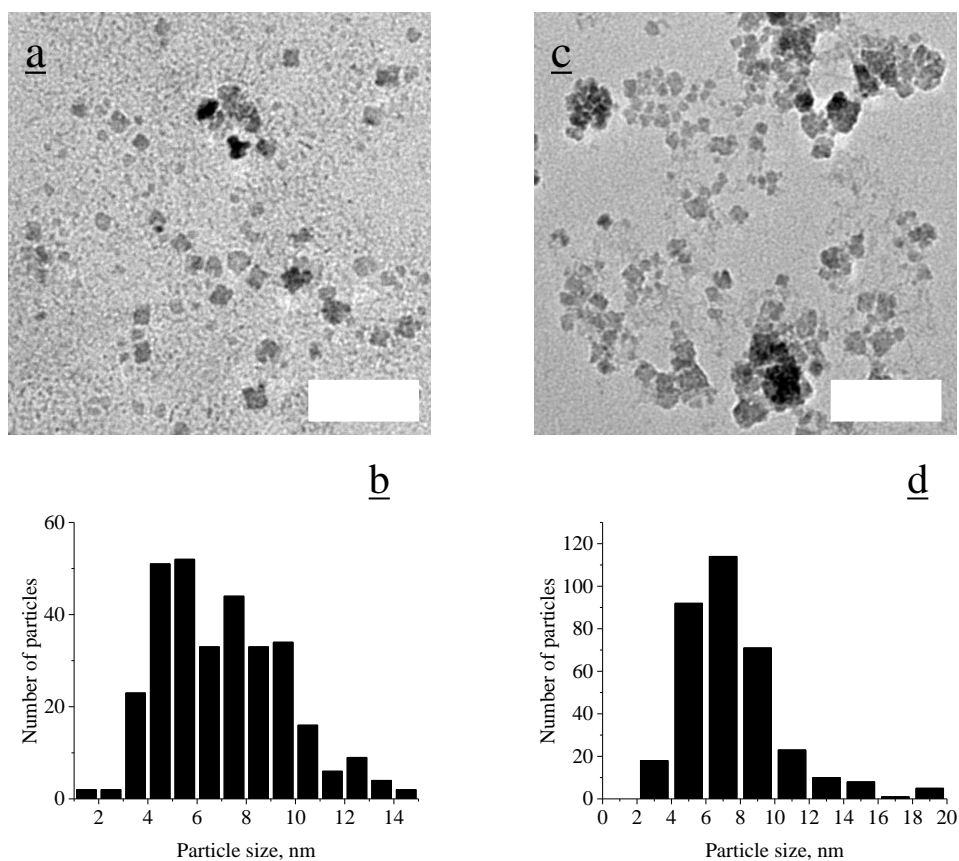
Figure 34. Transmission electron microscopy images and histograms of particle size distributions following thermolysis of $Mn(OAc)_2$ in oleylamine for (a,b) six hours at 150 °C and (c,d) three hours at 175 °C under N_2.

Table III. Summary of particle size and structure of as-prepared nanocrystals.

Precursor	Temperature	Oxidizing agent	Product	Particle size	Standard deviation
$Mn(OAc)_2$	150	None	None	-	-
$Mn(OAc)_2$	200	None	MnO	40	8
$Mn(OAc)_2$	250	None	MnO	100	30
$Mn(OAc)_2$	300	None	MnO	70	20
$Mn(OAc)_2$	150	$TMNO \cdot 2H_2O$	Mn_3O_4	8	1
$Mn(OAc)_2$	200	$TMNO \cdot 2H_2O$	MnO/Mn_3O_4	20	6
$Mn(OAc)_2$	250	$TMNO \cdot 2H_2O$	MnO	100	100
$Mn(OAc)_2$	300	$TMNO \cdot 2H_2O$	MnO	300	80
$Mn(OAc)_2$	150	Air	Mn_3O_4	10	2
$Mn(OAc)_2$	200	Air	Mn_3O_4	10	5
$Mn(OAc)_2$	250	Air	MnO	70	60
$Mn(OAc)_2$	300	Air	MnO	100	20
$Mn(acac)_3$	150	None	Mn_3O_4	8	2
$Mn(acac)_3$	200	None	Mn_3O_4	8	2
$Mn(acac)_3$	250	None	MnO	20	6
$Mn(acac)_3$	300	None	MnO	30	9

Mn(acac)$_3$	150	TMNO·2H$_2$O	Mn$_3$O$_4$	9	3
Mn(acac)$_3$	200	TMNO·2H$_2$O	MnO/Mn$_3$O$_4$	20	10
Mn(acac)$_3$	250	TMNO·2H$_2$O	MnO	60	30
Mn(acac)$_3$	300	TMNO·2H$_2$O	MnO	70	30
Mn(acac)$_3$	150	Air	Mn$_3$O$_4$	10	3
Mn(acac)$_3$	200	Air	Mn$_3$O$_4$	10	4
Mn(acac)$_3$	250	Air	MnO	20	10
Mn(acac)$_3$	300	Air	MnO	50	20

4.4 THERMAL DECOMPOSITION OF Mn^{3+} ACETYLACETONATE

After the conditions for control of chemistry and nanocrystal size of manganese oxides made by thermolysis of $Mn(OAc)_2$ were explored, it was determined that it is impossible to synthesize nanocrystals of pure Mn_2O_3. To try and prepare this product, a precursor with Mn in the 3+ oxidation state was chosen, namely Mn^{3+} acetylacetonate [$Mn(acac)_3$]. Also, to prevent any contamination by H_2O, an anhydrous salt of $Mn(acac)_3$ was used for this study. $Mn(acac)_3$ was heated in a TGA apparatus under synthetic air and underwent a series of exothermic (-61.4 J) decomposition events between 170 – 320 °C (Figure 35a). According to the diffractogram in Figure 35b, the decomposition product in air consisted of pure Mn_3O_4, which was accompanied by an reduction in mass of 77 % (theoretical loss, 78 %). Conversely, while being heated in N_2 atmosphere, $Mn(acac)_3$ underwent endothermic (0.6 J) phase changes between 170 – 320 °C (Figure 35c). Bragg reflections associated with crystalline MnO were detected after decomposition in N_2 atmosphere (Figure 35d). After thermal decomposition in N_2 atmosphere there was a 56 % loss in mass, which was much less than the expected loss of 80 %. $Mn(acac)_3$ is incredibly stable and temperatures greater than 500 °C are needed to fully decompose it under inert atmosphere.[85] When thermolysis of $Mn(acac)_3$ was carried out in oleylamine, Mn_3O_4 was produced after one hour of annealing at 150 and 200 °C, regardless of conditions (Figure 36). Following decomposition under N_2 with TMNO·2H$_2$O at 200 °C, Mn_3O_4 was mixed with MnO (Figure 36c). Compared to similar heat-up synthesis with $Mn(OAc)_2$, the only differences were observed at under rigorously inert conditions, where the use of a Mn^{3+} precursor led to Mn_3O_4 instead of MnO. In the case of 150 °C, the change in precursor also induced a reaction with accelerated kinetics, as oxide nanoparticles could be collected after just one hour of annealing under inert conditions.
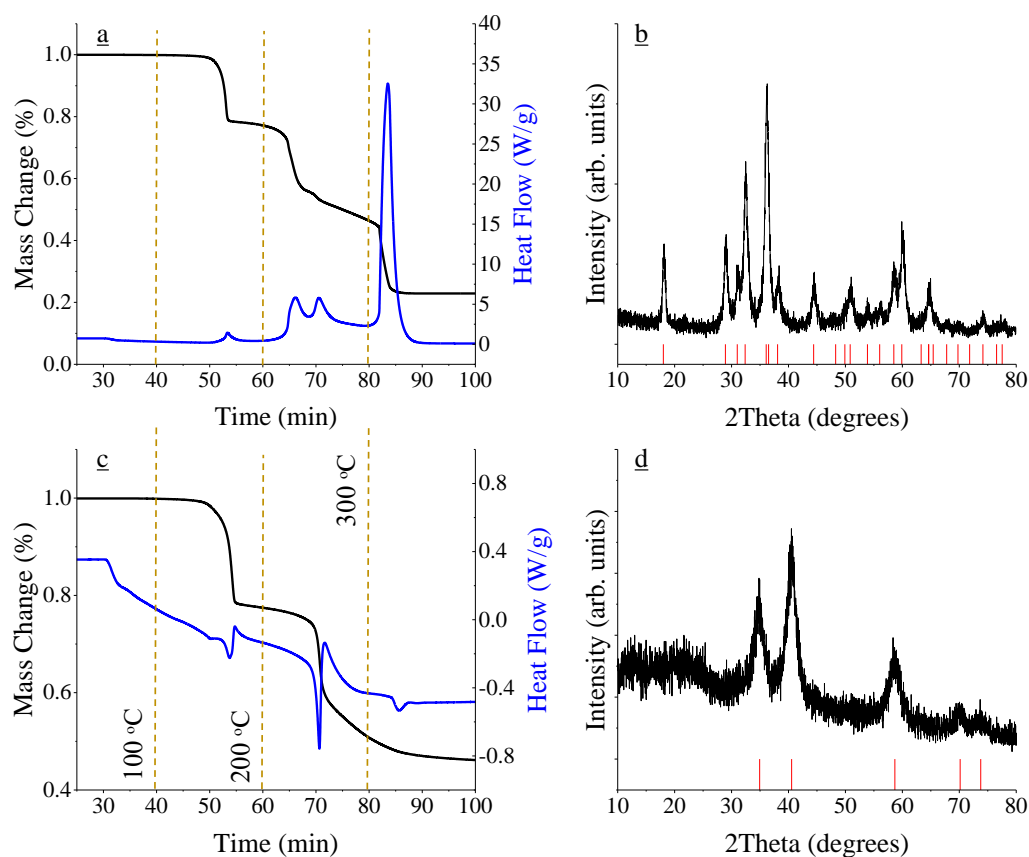
Figure 35. Thermal gravimetric analysis (black line) and differential scanning calorimetry (blue line, exo up) plots following heating of Mn(acac)$_3$ powder in synthetic air (a) or N$_2$ (c) atmospheres. Powder X-ray diffraction patterns of the corresponding products of decomposition in synthetic air (b) and N$_2$ (d) atmospheres are also shown, respectively. Red tick marks correspond to standard reflections of the crystallographic planes of spinel Mn$_3$O$_4$ (b) and cubic MnO (d). Orange dashed lines correspond time of experiment to temperature, where 40, 60, 80 and 84 min are equivalent to 100, 200, 300 and 320 $^{\circ}$C.
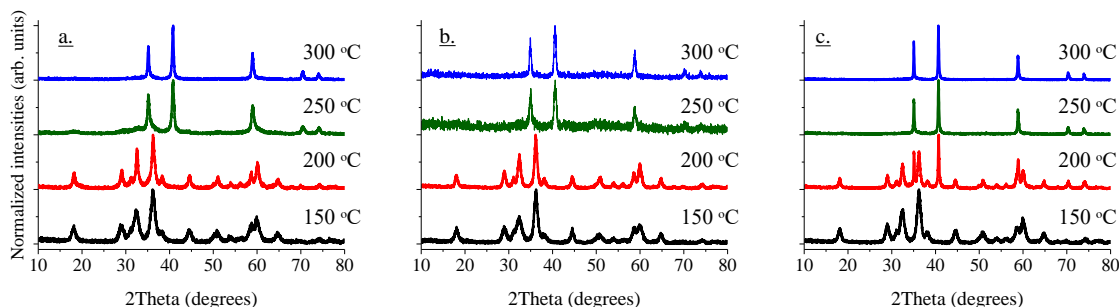
Figure 36. Powder X-ray diffraction of as-prepared nanocrystals following thermal decomposition of Mn(acac)$_3$ in oleylamine as a function of temperature in, (a) N$_2$, (b) air or (c) N$_2$ with TMNO·2H$_2$O. Diffraction peak intensities were normalized.

Figure 36 also shows that the products of thermolyzing Mn(acac)$_3$ at either 250 or 300 °C for one hour, regardless if the reaction was assisted by oxidizing agents or inert, always resulted in the formation of MnO nanocrystals. These results allude to the triple role of oleylamine as solvent, surfactant and reducing agent since all Mn^{3+} in the precursor Mn(acac)$_3$ reduced to MnO (Mn^{2+}). They build upon a body of work in the literature, where oleylamine has been shown to reduce other trivalent transition metal acetylacetonate precursors (Co(acac)$_3$ and Fe(acac)$_3$) to their pure monoxide phases (CoO and FeO) during colloidal syntheses at annealing temperatures of 200 °C or greater.[86,87] During the decomposition of Mn(acac)$_3$, reactions were consistently brown upon heating, suggesting that the discrepancy between dry heating and thermolysis in oleylamine is not due to a complete reduction of Mn^{3+} to Mn^{2+} during the early stage of Mn-O-oleylamine complex formation. To understand this process better, an aliquot of the reaction solution was taken during the thermolysis of Mn(acac)$_3$ at 250 °C in air after 30 min. PXRD revealed that the washed product was composed purely of Mn$_3$O$_4$ (Figure 37). Further annealing, for a total of one hour, resulted in pure MnO (Figures 36b and 37). From these results it is logical that upon heating, the Mn-O-oleylamine complex decomposed to favorably form Mn$_3$O$_4$ nanocrystals at low

temperature in air. Then, after maintaining a reaction temperature of at least 250 °C for one hour, Mn_3O_4 reduces totally to MnO nanocrystals. These results indicate that oleylamine acts with a triple role, solvent, surfactant, and reducing agent; likely due to the existence of an amine headthat facilitates reduction of nanocrystals at elevated temperatures.[84] It is possible that the reducing character of oleylamine assists in the reduction of Mn^{3+} to form Mn_3O_4 even at temperatures as 150°C, leading to a reaction that involves fast kinetics of product formation.
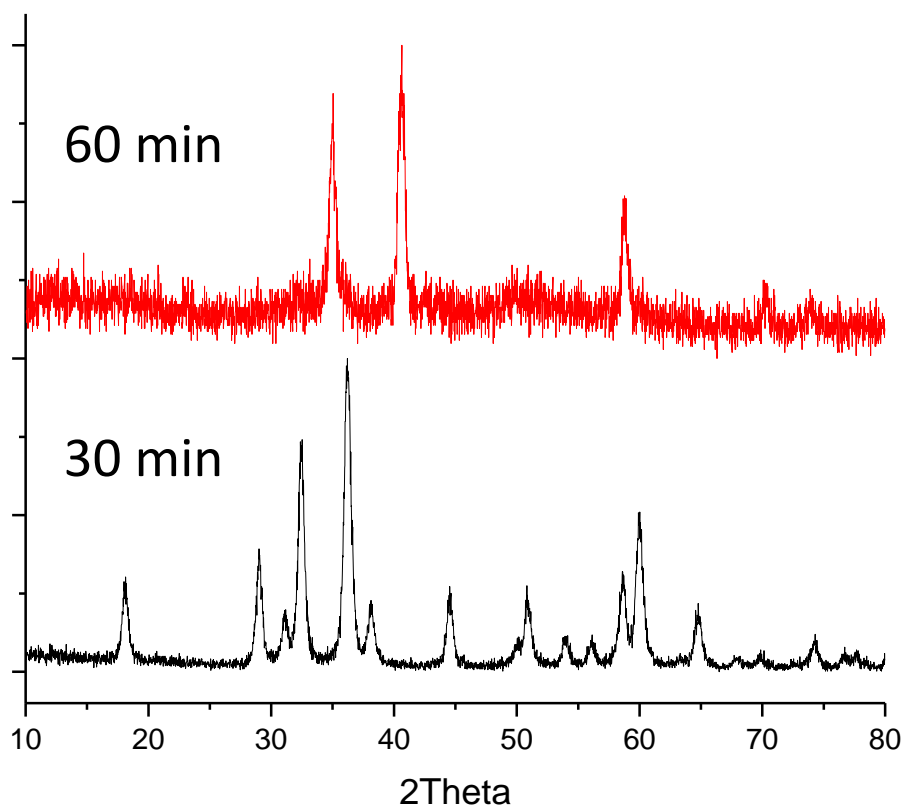
Figure 37. Powder X-ray diffraction of the powder product following the thermolysis of $Mn(acac)_3$ in oleylamine at 250 °C while exposed to air.

A global overview of particle sizes and size distributions of the decomposition products of Mn(acac)$_3$ in oleylamine is shown in Figure 38a and recorded directly in Table II. Figure 38a reflects histograms (Figure 39) determined by counting at least 300 particles in TEM images (Figure 40). Figures 38b-e correspond to TEM images of the nanocrystalline products formed after annealing Mn(acac)$_3$ in oleylamine for one hour from 150 – 300 °C, which are representative of other samples at similar temperatures. Pure Mn$_3$O$_4$ nanocrystals produced in these reactions were more or less similar in size. After one hour of decomposition at 150 °C in N$_2$, N$_2$ with TMNO·2H$_2$O, and in air, the diameters of the Mn$_3$O$_4$ particles were 8 ± 2, 9 ± 3, and 10 ± 3 nm, respectively, and spherical in shape. The most significant crystal growth occurred above 200 °C, followed by a simultaneous transformation of the rice-shaped Mn$_3$O$_4$ to quasi-cubes of MnO. At 250 and 300 °C in N$_2$, particles had measured diameters of 20 ± 6 and 30 ± 9 nm, respectively. By allowing air to enter the reaction environment, nanocrystals of MnO of 20 ± 10 and 50 ± 20 nm were produced, respectively. The use of air did not significantly change the size of the nanocrystals of MnO. However, the diameters of nanocrystals of MnO were measured to be 60 ± 30 and 70 ± 30 nm following thermal decomposition of Mn(acac)$_3$ in the presence of TMNO·2H$_2$O at 250 and 300 °C. This increase in nanoparticle diameter is consistent with TEM analysis of Mn(OAc)$_2$ decomposed in the presence of TMNO·2H$_2$O. Also, the diameter of the MnO nanocrystals at higher decomposition temperatures were found to be smaller than those formed using the precursor of Mn(OAc)$_2$.
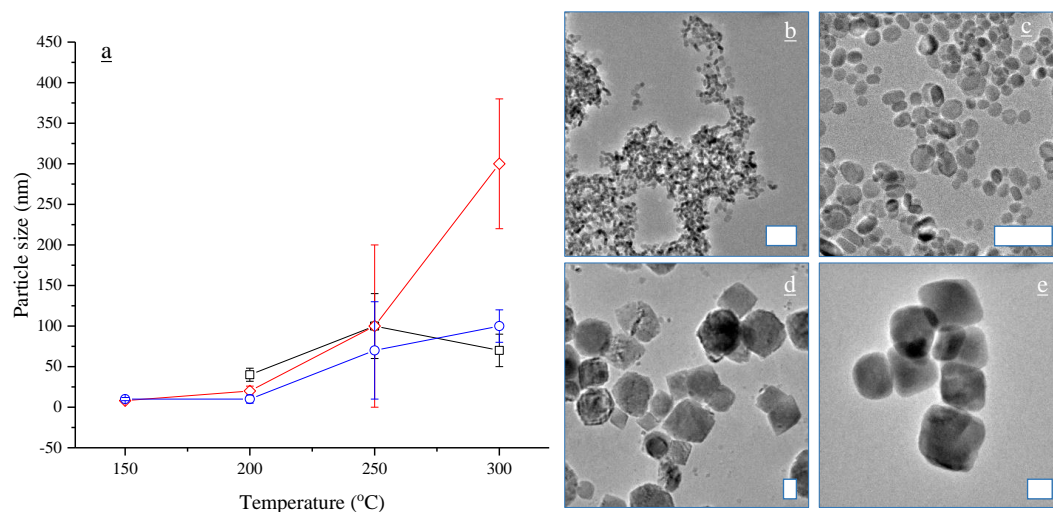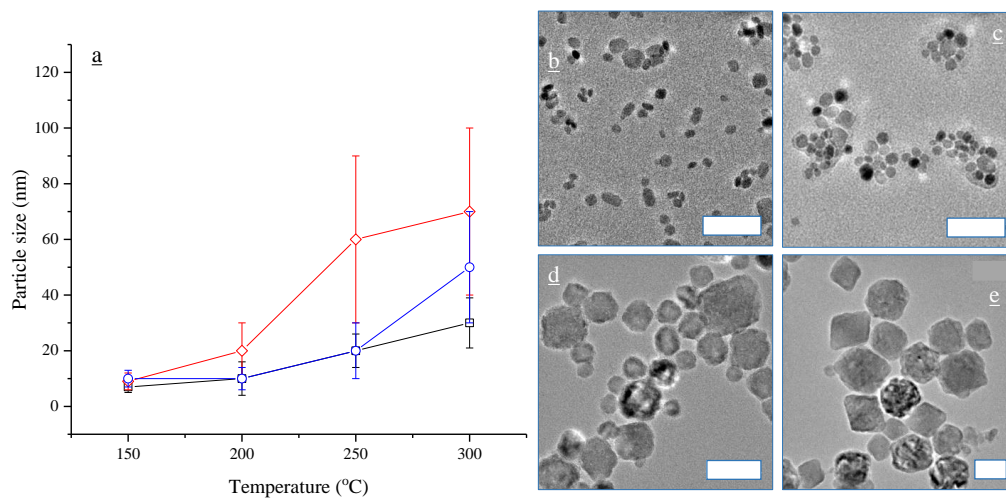
Figure 38. (a) Size distribution of nanoparticles produced after thermally decomposing Mn(acac)$_3$ in oleylamine. Squares, diamonds and circles correspond to reactions in N$_2$, N$_2$ with TMNO·2H$_2$O and air. Representative transmission electron microscopy images of products of the reactions under air, at (b) 150, (c) 200, (d 250, and (e) 300 °C. White scale bars correspond to 50 nm.
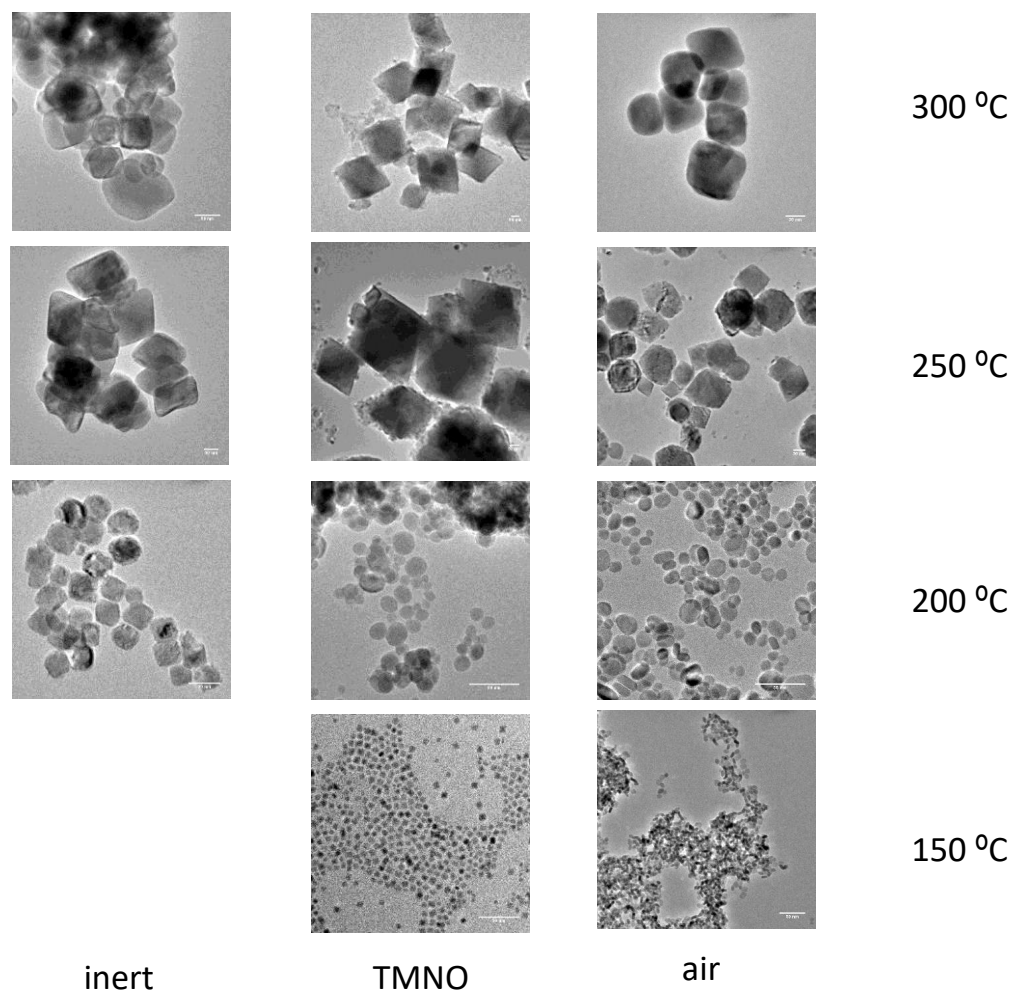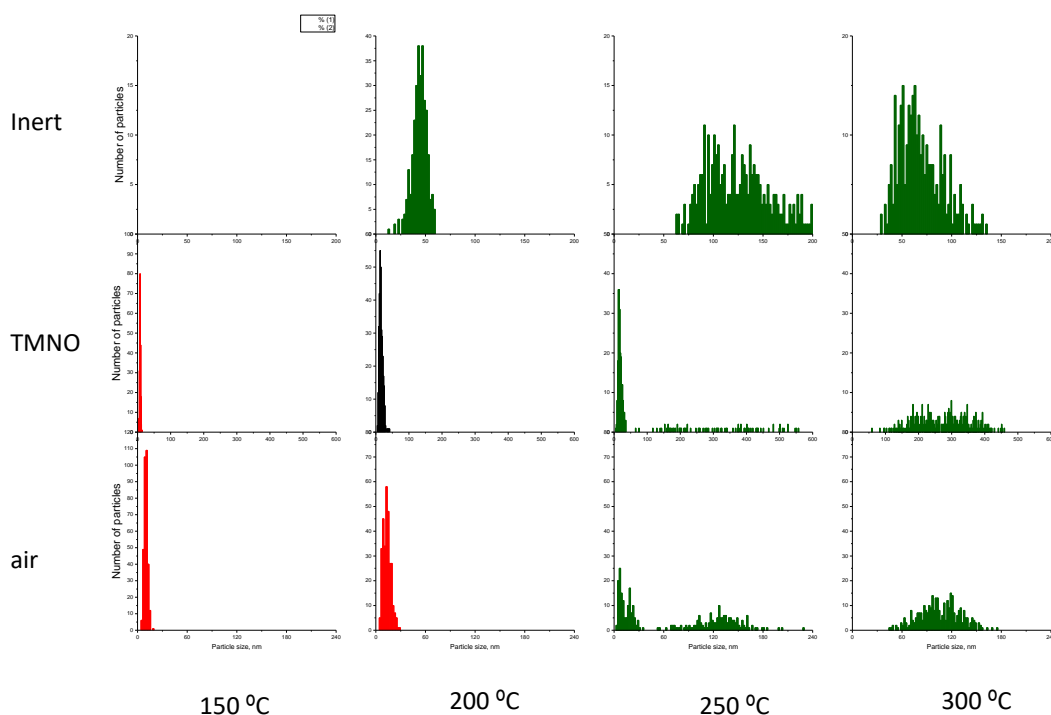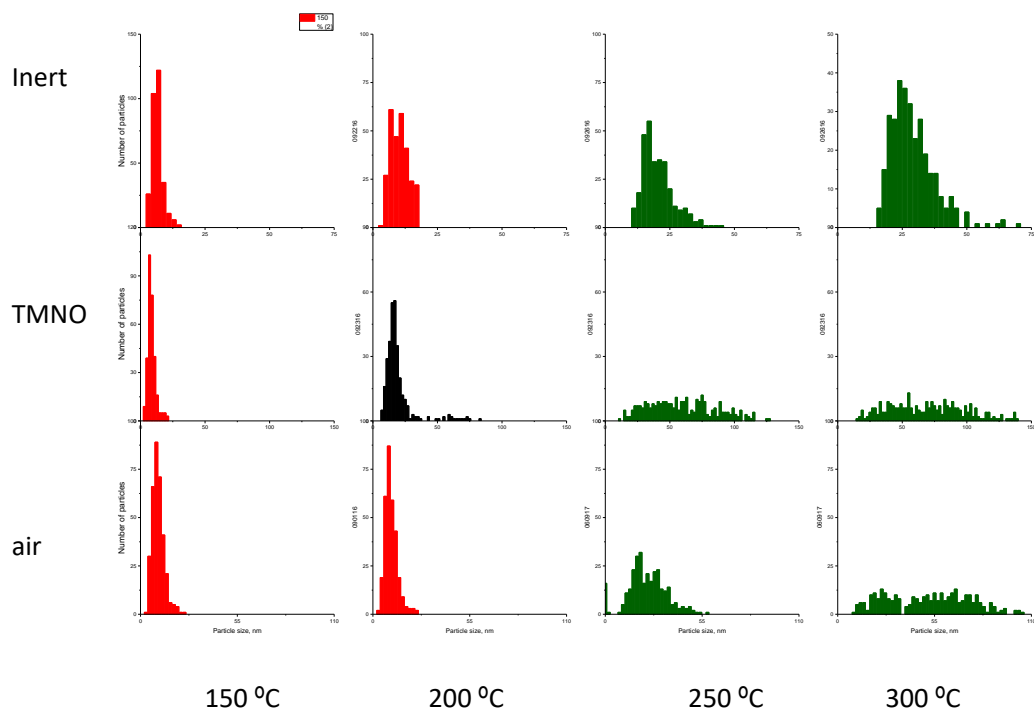
Figure 39. Histograms of particle size distribution following thermal decomposition of Mn(acac)$_3$ in

oleylamine for one hour at 150, 200, 250 and 300 $^\circ$C under inert conditions, or oxidized by TMNO·2H$_2$O

or air. Red, green and black correspond to products' phase identified as pure Mn$_3$O$_4$, pure MnO and

mixed Mn$_3$O$_4$/MnO, respectively.
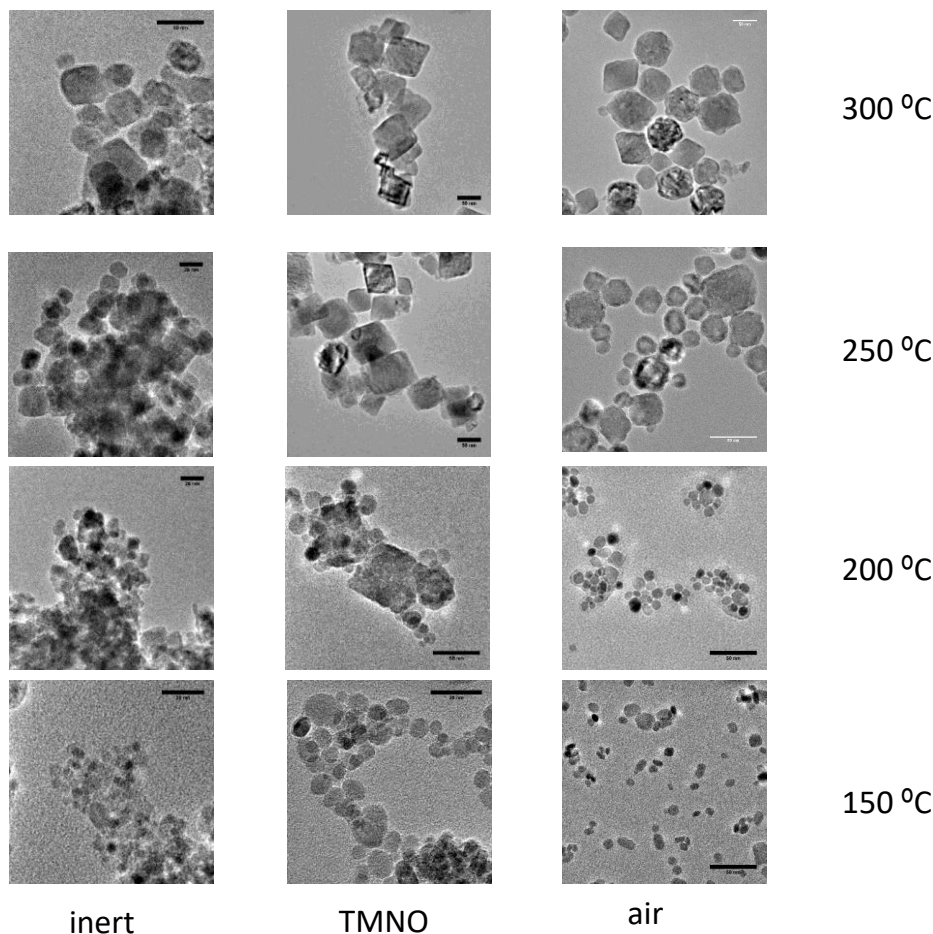
Figure 40. Transmission electron microscopy images following thermal decomposition of Mn(acac)$_3$ in oleylamine for 1 h at 150, 200, 250 and 300 °C under inert conditions, or oxidized by TMNO·2H$_2$O or air. Scale bars correspond to 50 nm.

4.5 CONCLUSIONS

This report clarifies the role of different synthetic conditions on the production of colloidal nanocrystals of MnO and Mn$_3$O$_4$ by thermolysis of Mn(OAc)$_2$ or Mn(acac)$_3$ at elevated temperature in the presence of oleylamine, using a simple heat-up approach. It was found that only nanocrystals of MnO

could be synthesized from $Mn(OAc)_2$ precursor in a reaction solution that was carefully controlled to have no O_2 and H_2O contamination, with temperature only determining particle size and reaction kinetics. Conversely, when decomposing $Mn(acac)_3$ under inert conditions, nanocrystals of Mn_3O_4 were synthesized at or below 200 °C, whereas nanocrystals of MnO were the result of treatments above 250 °C if longer than 30 min. Regardless of precursor, oxidizing agents (air and TMNO·$2H_2O$) favored the formation of Mn_3O_4 nanocrystals at annealing temperatures of 150 and 200 °C. Therefore, temperature was the dominant factor affecting the composition of the product at annealing temperatures higher than 200 °C, regardless of the use of oxidizing agents and the oxidation state of the Mn precursor. Crystals of either of MnO and Mn_3O_4 smaller than 20 nm were generally reachable below 200 °C, whereas growth was rapid above this temperature. The data in this study provide a compendium that rationalizes seemingly contradicting observations in the literature. They highlight the importance of the control of the reaction environment to produce the desired phases. The study also provides strong indication that the formation of manganese oxides showing an average oxidation state of +3 or higher in colloidal form will require chemical creativity to move beyond unsaturated solvents and surfactants. The promise of a large new families of functional materials should provide motivation for the community to embark on this synthetic challenge.

5 EXPLORING Mg INTERCALATION IN NANOCRYSTALS OF SPINEL MANGANESE OXIDES

5.1 INTRODUCTION

As discussed above, spinel-type Mn_2O_4 is predicted to allow Mg^{2+} mobility within the 3D network of tunnels with reasonable kinetics and high insertion potentials, potentially leading to rechargeable battery systems with higher energy densities.[51] Also, the materials are low-cost, safe and environmentally benign, making them promising candidates for rechargeable Mg batteries. However, the sluggish kinetics of Mg^{2+} diffusion observed in submicrometer Mn_2O_4 crystals[47] needs to be overcome and reversible Mg^{2+} intercalation in nonaqueous electrolytes needs to be realized in order to achieve a working Mg battery prototype. Solid-state methods are known to produce ordered $MgMn_2O_4$ with a spinel crystal structure, but the particle sizes are micrometric.[88] Reducing particle sizes to the nanoscale would shorten transport pathways, compensating energy barriers due to inherently slow transport within the crystal structure. Yin et al. used the Pechini method to synthesize ordered spinel-type $MgMn_2O_4$ with diameters of 11 and 31 nm.[89] Despite showing electrochemical cycling curves in Mg electrolyte, there was no spectroscopic evidence of Mn redox to accompany the subtle structural changes. Colloidal synthesis reactions are known to produce nanocrystals of complex oxides with uniform size distribution and morphological characteristics., but attempts at a simple one-pot colloidal synthesis of this target compound in oleylamine resulted in nanocrystals of incorrect stoichiometry $Mg_{0.5}Mn_{2.5}O_4$, which could not be further enriched with Mg.[52] The search for ordered tetragonal spinel $MgMn_2O_4$ nanocrystals continues and characterizing its exclusive Mg^{2+} intercalation chemistry remains a challenge.

From the colloidal reaction space surveyed in chapter 4, optimal conditions to reproducibly make <10 nm crystals of MnO were identified. The inherent limitation in the oxidation state of Mn in the environment of colloidal synthesis was overcome by developing a procedure to calcine colloidal nanocrystals of MnO with Mg precusors to form ordered $MgMn_2O_4$ while limiting increases in particle size. Their ability to

deintercalate Mg^{2+}, the key reaction in a potential Mg battery, was characterized in anhydrous electrolytes.

5.2 EXPERIMENTAL PROCEDURE

First, the MnO nanocrystals were synthesized according to a previously reported method.[90] In this particular synthesis, $Mn(acetate)_2$ was decomposed in oleylamine under inert conditions for 1 hour at 175 °C. MnO nanocrystals were prepared and used same day. Several reactions were explored to accomplish the objective of synthesizing stoichiometric, ordered $MgMn_2O_4$.

5.2.1 CALCINATION USING Mg HYDROXIDE

$Mg(OH)_2$ (Sigma-Aldrich) and MnO nanocrystals were thoroughly mixed and annealed in a 1:2 molar amount at 500 °C for 8 hours while exposed to laboratory atmosphere, for the following hypothetical reaction:

5.2.2 CALCINATION USING Mg ACETATE

Mg acetate tetrahydrate $Mg(CH_3CO_2)_2 \cdot 4H_2O$ (Sigma-Aldrich) was dissolved in ethanol in a mortar. Using IR light, the ethanol was evaporated. Then MnO was ground in at 0.9:2 molar ratio between Mg and Mn. The mixture was annealed in air at 500 C for 8 hours, for the following hypothetical reaction.

The product was reground and then characterized. Two batches will be compared, large and small. The amount of MnO and $Mg(ac)_2$ was 350 (4.9 mmol) and 490 (2.3 mmol) mg in the large batch (LB). In the small batch (SB) the amounts of precursor materials were about 5 times less than LB. In SB synthesis, the amount of MnO and $Mg(ac)_2$ was 80 (1.1 mmol) and 110 mg (0.5 mmol). Both LB and SB procedures had about 90 % product yield.

Methods of characterization are detailed in chapter 2. In this chapter, structural characterization will be completed using powder X-ray diffraction (PXRD) using ($\lambda_{avg} = 1.5418$ Å) radiation. Transmission electron microscopy (TEM) was completed using a JEM 3010 (JEOL) operated at 300 kV. Soft X-ray absorption spectroscopy was conducted at Mn $L_{2,3}$- and O K-edges.

5.3 RESULTS

5.3.1 REACTION WITH Mg HYDROXIDE

The diffractogram of precursor MnO for each following reaction is shown in chapter 4 figure 31.[90] Pawley analysis used to determine MnO nanocrystals have expected cubic unit cell with lattice constant $a = 4.448$ Å (space group *Fm-3m*). TEM analysis indicates MnO formed as 8 ± 3 nm quasicubes (chapter 4 figure 34) Powder X-ray diffraction revealed that the product of the reaction with $Mg(OH)_2$ (Figure 41) contained Bragg reflections associated with Mn_2O_3 (PDF 01-073-1826), Mg_6MnO_8 (PDF 01-073-2157), and MgO (PDF 00-045-0946). The reaction of MnO with $Mg(OH)_2$ could not be completed into the desired $MgMn_2O_4$ in these conditions probably due to the favorable formation of MgO, which formed before reaction with the Mn precursor.[91]
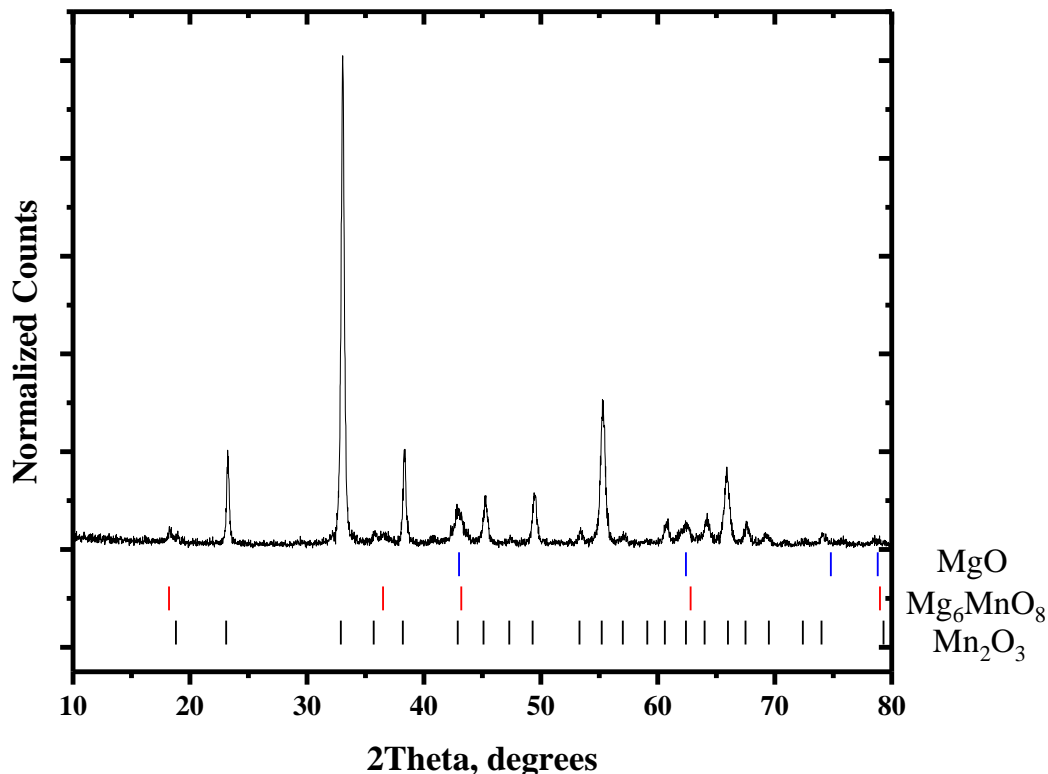
Figure 41. PXRD pattern of MnO nanocrystals reacted with Mg hydroxide. Reference Bragg reflections are Mn_2O_3, Mg_6MnO_8, and MgO.

5.3.2 REACTION WITH Mg ACETATE IN A LARGE BATCH (LB)

Nanocrystalline spinel-type $LiMn_2O_4$ has been reportedly prepared by calcining stoichiometric amounts of nanocrystals of MnO and Li acetate.[92] As an analogous system, $Mg(ac)_2$ tetrahydrate was selected as the Mg source. $Mg(ac)_2$ decomposes at 323 °C and is soluble in polar organic solvents.[91] It was important to solubilize the Mg salt in order to homogenize it with nanocrystals during mixing to enhance the reaction and avoid segregation of MgO. Figure 42 shows the diffractogram of $MgMn_2O_4$ -LB. Pawley analysis determined the product was composed of two crystalline phases. The main phase corresponds to

89

a tetragonal spinel $MgMn_2O_4$ (space group *I4₁/amd* PDF#:00-023-0392) with a = 5.73754 Å, c = 9.19640, and cell volume of 302.74 $Å^3$. These lattice constants compare well to $MgMn_2O_4$ with tetragonal spinel crystal structure found in the literature.[89] An impurity phase was also detected corresponding to cubic spinel Mg_2MnO_4 (space group *Fm-3m* PDF # 00-019-0773) with a lattice parameter (a) equal to 8.32824 Å and cell volume of 577.56 $Å^3$. This lattice constant compares well to cubic spinel Mg_2MnO_4 found in the literature.[93] In the tetragonal spinel, Mg^{2+} is in primarily in the tetrahedral sites and Mn^{3+} occupies the octahedral site. In the cubic spinel, Mg^{2+} occupies the tetrahedral sites and half of the octahedral sites, with Mn^{4+} occupying the other half of the octahedral sites. The molar fractions of tetragonal and cubic spinel phases in the large batch were determined to be 69 and 31 % after completing Pawley fits. The mixture of phases in the final product likely reflects the inhomogeneous distribution of Mg and Mn in the precursor mixture prior to annealing. The fits also estimated particle sizes to be 14 nm, based on the peak widths.
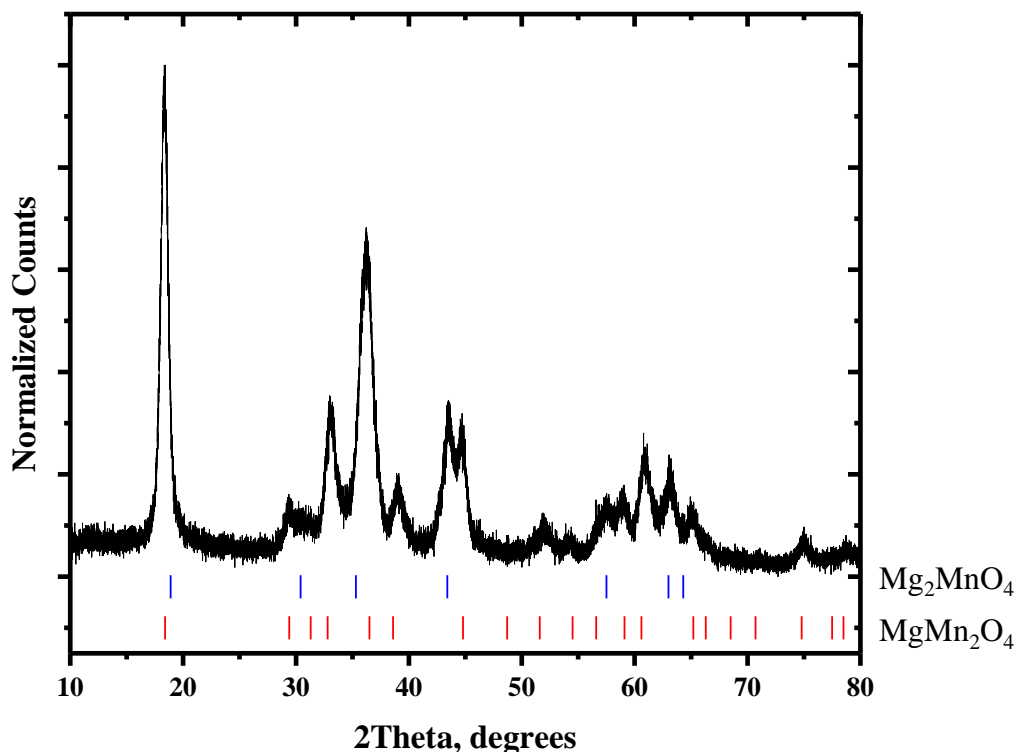
Figure 42. PXRD of MgMn$_2$O$_4$-LB. Reference Bragg reflections correspond to tetragonal spinel MgMn$_2$O$_4$ and cubic spinel Mg$_2$MnO$_4$.

Transmission electron microscope images of MgMn$_2$O$_4$-LB nanocrystals were taken and a representative example is shown in Figure 43a. To create a histogram (figure 43b), over 300 particles were counted for statistical significance according to the recommendations by editors of topical journals in nanotechnology.[61] Primary particles of MgMn$_2$O$_4$-LB appear as 15 ± 5 nm quasicubes. This value is similar to 14 nm estimated from Pawley analysis. Therefore, following calcination, there was a small increase in size of the particles compared to the MnO precursor. Secondary particles formed as

agglomerates of primary particles from one hundred to several hundred nanometers. Annealing at 500°C did not alter parent morphology.
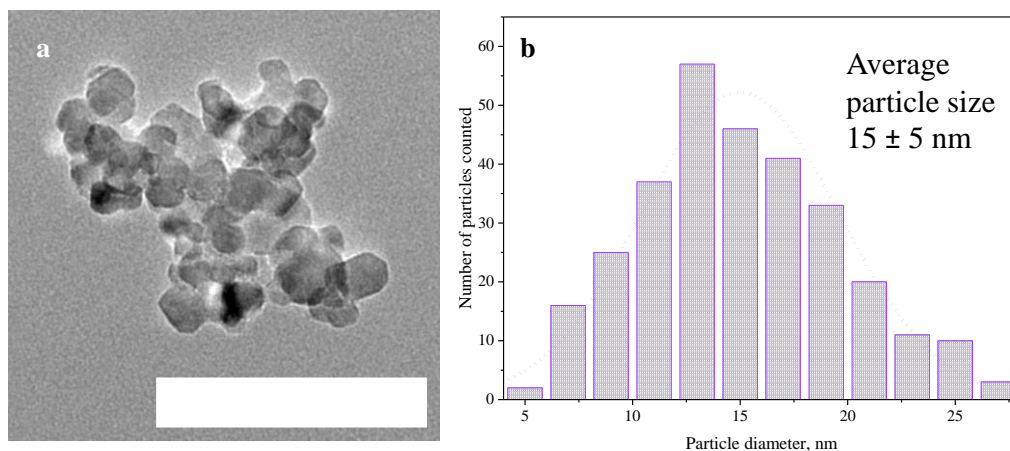
Figure 43. TEM image of (a) MgMn$_2$O$_4$-LB product and (b) histogram of particle size distribution. Scale bar is 100 nm.

Electrochemical properties in cells with Li metal counterelectrodes.

At the start of this project, electrolytes based on Mg^{2+} salts did not have sufficient anodic stability to withstand the potentials predicted to induce deintercalation of the divalent ion from MgMn$_2$O$_4$ (above 3 V vs. Mg^{2+}/Mg^0). Anhydrous Li-based electrolytes from commercial suppliers are stable to these high anodic potentials. If MgMn$_2$O$_4$ particles are submerged in Li electrolyte, the possibility of Li intercalation is negligible because this is the discharged state of the working electrode. Therefore, an avenue to investigate Mg deintercalation in this material is to use conventional coin cells with Li metal counter

electrode and commercial anhydrous Li electrolytes, because only an ionically conductive medium is needed the close the circuit. Working electrodes of $MgMn_2O_4$-LB were galvanostatically oxidized to 5 V vs. Li^+/Li^0 (4.3 V vs. Mg^{2+}/Mg^0) at room temperature at current rate of C/50. Electrochemical data is shown in figure 44a. Upon oxidation, the potential increased to 5 V vs. Li^+/Li^0 after 50 mAh/g with no plateau then plateaued until the time limit of a complete theoretical oxidation was reached (50 h).

Powder X-ray diffraction was used to characterize any structural changes following electrochemical testing. The first cell was stopped after reaching 123 mAh/g, 45% of theoretical capacity, and the diffractogram of the working electrode is shown in figure 44b. The Bragg reflections associated with the stainless steel mesh are not present because the working electrode was sonicated off the current collector. The signal to noise ratio was too poor to perform a Pawley fit. Consequently, the (001) reflection (18 °) was aligned to the pristine's (001) reflection as way to detect relative peak displacements. There was no significant difference in the position of the observed Bragg reflections. The next working electrode to be harvested and characterized by PXRD was stopped at 270 mAh/g (100 % theoretical capacity, figure 44a). XRD was taken with stainless steel current collector intact and used as internal reference. Pawley analysis of the diffractogram of this working electrode determined that both tetragonal and cubic spinel phases were present. The lattice constants of $MgMn_2O_4$-LB (space group *I41/amd*) were a = 5.72579 Å, c = 9.22692, and cell volume of 302.5 Å^3. Also, the cubic-type Mg_2MnO_4 (space group *Fm-3m*) had a lattice parameter (a) equal to 8.26174 Å and cell volume 563.9 Å^3. Compared to the pristine state, slight decreases in cell volumes were observed in both phases.
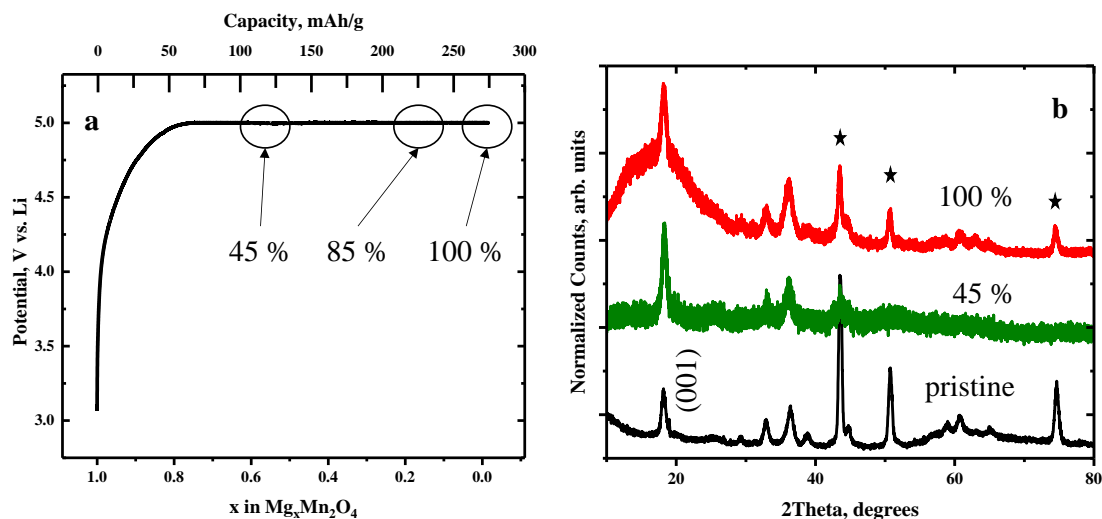
Figure 44. (a) Voltage profile for the electrochemical oxidation of $MgMn_2O_4$ -LB in a cell with Li^+ electrolytes and a Li metal counter electrode, at room temperature. Points in the reaction where chemical analysis was conducted are indicated. (b) PXRD patterns of the oxidized samples versus the pristine. Stainless steel peaks have been noted (*) and used as internal reference for peak alignment.

X-ray absorption spectroscopy was used to probe changes in the chemical states of Mn and O following electrochemical testing. XAS at the Mn $L_{2,3}$- and O K-edges on samples collected after reaching 45, 85 and 100 % theoretical capacity and are shown in figures 45 and 46. The Mn $L_{2,3}$-edge surveys the chemical state of Mn by characterizing Mn 2p electron transitions to unfilled Mn 3d orbitals. Only electron yields were detected and shown in figure 45a. The corresponding fluorescence spectra at the Mn $L_{2,3}$-edge suffered from deleterious self-absorption events, and, thus, they are not shown. Detection of electron yields correspond to chemical states within the first ten nanometers of the surface of the particle. Since the particles are 15 ± 5 nm, the electron yield can represent the interior of these objects as well. The L_3 event has many fine features and the significant absorption events will be noted. Due to

the rather featureless shape of the L_2 feature, the centers of gravity were calculated by integrating the spectra using Origin Software.

Mn $L_{2,3}$-edge spectra of the pristine $MgMn_2O_4$-LB is shown in figure 45a. This sample had at least five distinguishable maxima in the L_3 absorption region between 640 and 645 eV, with the most prominent signal at 642.3 eV, followed by a L_2 absorption event with a center of gravity near 653 eV, and a shoulder near 651 eV. Comparison of $MgMn_2O_4$-LB with standards revealed significant similarities. For instance, the energy positions of the maxima in the L_3 region were similar to those of the spinel $MgMn_2O_4$ standard, but the ratio of peak intensities differed (figure 45b). The identity of the standard was confirmed as a normal spinel by PXRD, and the result indicates the presence of only Mn^{3+} in octahedral sites. The prominent event just above 643 eV is a signature of Mn^{4+}, which has contributions from the cubic Mg_2MnO_4 phase detected by PXRD. Additionally, comparison of $MgMn_2O_4$-LB with Mn_3O_4 shows prominent intensity that is associated with Mn^{2+}. This is evidence of site exchange between Mg and Mn sites.[52] This was undetectable using in-house diffraction equipment due to the small diffraction domains of the nanocrystals. Rietveld refinements of high-resolution synchrotron X-ray diffraction should be completed to ascertain levels of site exchange.

A comparison of the subtle changes in L_3 region between electrochemically oxidized $MgMn_2O_4$-LB and other relevant compounds is shown in figures 45c and 45d. From the pristine state to 45 % oxidized, the prominent event at 643.5 eV increased in intensity relative to the other features (Fig. 45b). Additionally, the center of gravity of the L_2 event blue-shifted to 654 eV. These changes are consistent with increasing Mn^{4+} content and consequent oxidation of Mn. From 45 to 100 % oxidized, the event at 640 eV increased in intensity, which is indicative of increasing Mn^{2+} character. Also, the prominent feature at 643 eV reduced in intensity relative to the other events in the L_3 region, which is indicative of diminishing Mn^{4+} character. These signified a reduction of Mn despite the anodic currents applied to the cell.[94]
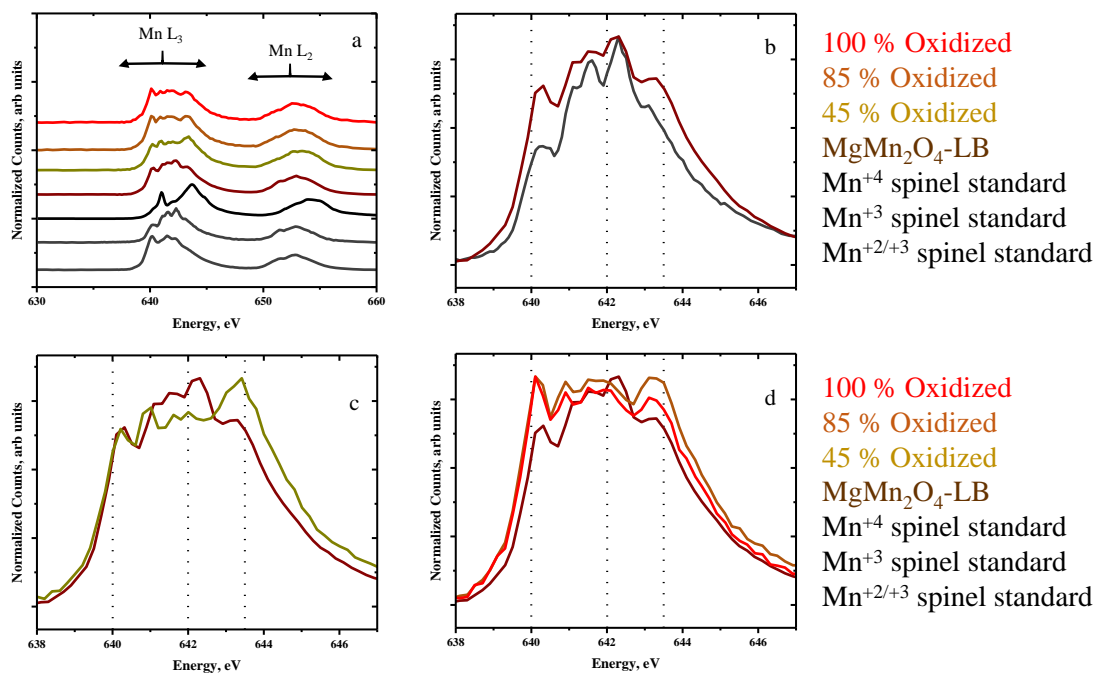
Figure 45. (a) Stacked electron yields at the Mn $L_{2,3}$-edge of $MgMn_2O_4$-LB and electrochemically oxidized samples, compared to standards of $Mn^{2+/3+}$ (spinel Mn_3O_4), Mn^{3+} (ordered spinel $MgMn_2O_4$), and Mn^{4+} (delithiated spinel Mn_2O_4), (b) overlay of pristine $MgMn_2O_4$-LB compared to ordered $MgMn_2O_4$, (c) overlay of the as-made $MgMn_2O_4$-LB compared to 45 % oxidized electrode, and (d) overlay of the as-made $MgMn_2O_4$-LB compared to 85 and 100 % oxidized electrodes. Dotted lines near 640, 642, and 643.5 eV are signatures of Mn^{2+}, Mn^{3+}, and Mn^{4+}, respectively. Working electrodes were oxidized at room temperature in Li coin cells.

The O K-edge spectra of the pristine $MgMn_2O_4$-LB and electrochemically oxidized samples compared to standards are shown in figure 46. Both modes of detection, electron (figure 46a-c) and fluorescence (figure 46d-f), were used which correspond to surface and average in-depth chemical state.

The pre-edge region corresponds to the hybridized states from mixing O 2p and Mn 3d orbitals, thus being most sensitive to changes in redox state. It had only one prominent feature near 530 eV followed by many absorption events with low intensity and resolution, reminiscent of the Mn^{3+} standard (ordered $MgMn_2O_4$). The center of gravity of the main edge, corresponding to the energy of photoionization, was slightly red-shifted to lower energy compared to the Mn^{3+} standard reflecting the existence of Mn^{2+}. Upon oxidation to 45 %, two maxima appeared in the pre-edge region of the electron yield, similar to the Mn^{+4} standard material (spinel Mn_2O_4, figure 46d). The observed peak splitting is induced by the ligand field of the d orbitals, and was calculated to be 2.2 eV. The absorption edge in the electron yield blue-shifted by 2 eV higher in energy, indicative of oxidation. The electron yield had more pronounced peak shape changes following electrochemical oxidation than in the fluorescence yield, possibly due to a combination of different reactivity and the distorting effect of the intensity of the signals due to self-absorption in the fluorescence spectrum. From 45 to 100 % oxidized, the two absorption events in the pre-edge region became less pronounced in the electron yield. Also, the main absorption event red-shifted in both electron and fluorescence yields, especially the former. These changes are indicative of a reduction of Mn on the surface and in the bulk. Since the changes are more extreme on the surface, it is safe to say that the surface is more reactive than the bulk.
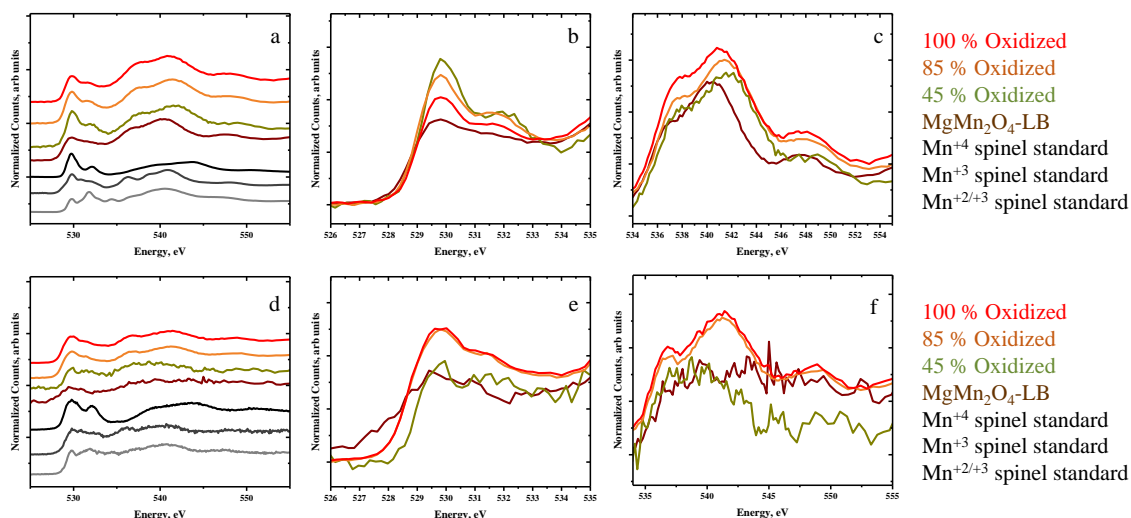
Figure 46. (a,d) Stacked O K-edge spectra of MgMn$_2$O$_4$-LB and electrochemically oxidized samples, compared to standards of Mn$^{2+/3+}$ (spinel Mn$_3$O$_4$), Mn^{3+} (ordered spinel MgMn$_2$O$_4$), and Mn^{4+} (delithiated spinel Mn$_2$O$_4$), and overlays of the pre-edge (b,e) and main edge (c,f) regions of pristine MgMn$_2$O$_4$-LB compared to electrochemically oxidized samples. Two different detection modes are shown, electron (a-c) and fluorescence (d-f) that correspond to chemical states at the surface and a depth of ~100-nm, respectively.

Theoretically, should deintercalation of Mg^{2+} occur once MgMn$_2$O$_4$ is oxidized in a cell, cubic spinel-type Mn$_2$O$_4$ should form. This compound is capable of intercalating Li$^+$ at around 4.0 V vs. Li$^+$/Li^0 to form LiMn$_2$O$_4$, and, subsequently, at around 2.9 V vs. Li$^+$/Li^0 to form Li$_2$Mn$_2$O$_4$. In contrast, MgMn$_2$O$_4$ does not uptake Li until below a cathodic potential of 1.0 V vs. Li$^+$/Li^0, and it follows a conversion reaction whereby both Mg and Mn in the oxide are reduced to their respective metallic forms, accompanied by formation of Li$_2$O.[95] Therefore, the formation of Mn$_2$O$_4$ can be probed electroanalytically in a rather simple manner using the same Li cells used to evaluate the oxidation step. Working electrodes with MgMn$_2$O$_4$-LB were first oxidized to 5 V vs. Li$^+$/Li^0 then cycled between 2 – 5 V

vs. Li^+/Li^0 for 10 cycles (Figure 47a). Despite the open circuit potential being at 1.5 V vs. Li^+/Li^0, the first

oxidation was generally consistent with the data in Figure 44a. Upon reduction, a small voltage plateau at

2.75 V vs. Li^+/Li^0 for about 10 mAh/g was observed before finally concluding reduction 45 mAhg/g. This

capacity of reduction corresponds to about 0.3 mol Li (figure 47b) Subsequent reductions resulted in the

observed capacity eventually increasing to 50 mAh/g. Upon oxidation, voltage plateaus at approximately

3 and 4 V vs. Li^+/Li^0 was observed and were apparent for the following oxidations. Unlike reduction, the

capacity of oxidation decreased from 300 to 50 mAh/g (83 % reduction) as cycling continued. The

voltage plateaus at around 4.0 and 2.9 V vs. Li^+/Li^0 are associated with intercalation of Li into and out of

the spinel host, suggesting that a detectable amount of Mn_2O_4 did form in the cell.[96]
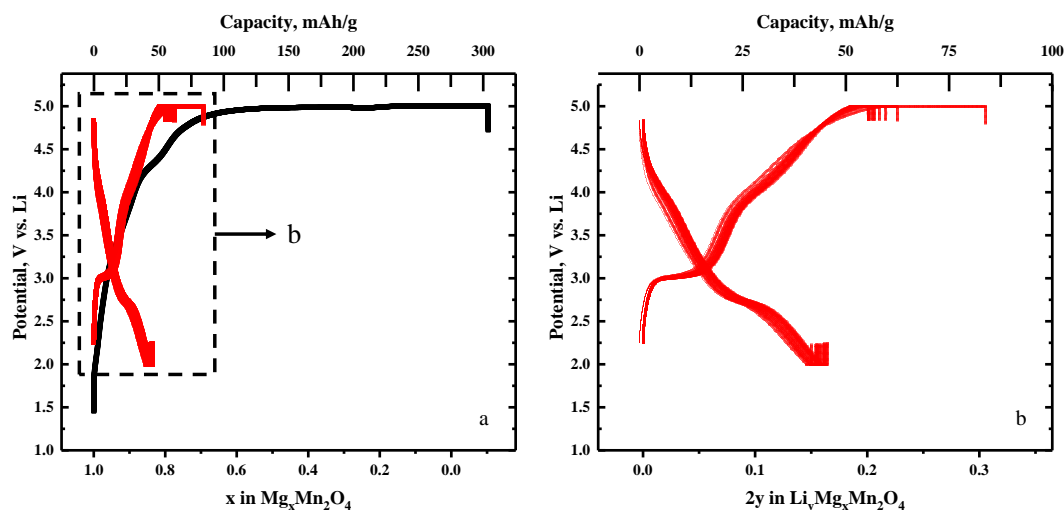
Figure 47. (a) Voltage profile for the electrochemical cycling of $MgMn_2O_4$-LB between 5 V and 2 V vs.

Li^+/Li^0 at room temperature where the initial oxidation is shown in black and the theoretical loss of Mg^{2+}

is shown on the x-axis and (b) voltage profile for subsequent cycles shown in red where the theoretical

loss or gain of Li^+ is shown in the bottom x-axis.

X-ray absorption spectroscopy at the Mn $L_{2,3}$-edge on working electrodes of $MgMn_2O_4$-LB electrochemically cycled in a Li coin cell at room temperature are shown in figure 48a compared to standards. Subtle changes in L_3 region following electrochemical testing are shown figures 48b-d. Upon initial electrochemical oxidation to 110 % theoretical, features at 640 and 643.5 eV increase in relative intensity to the other features. These changes are observed in figure 45d and are consistent with increasing Mn^{2+} and Mn^{4+} contents. Also, the L_2 feature broadens and red-shifts upon oxidation to 110 % (figure 48a). Similar changes were observed when comparing the O K-edge spectra in Figures 49 with those in Figures 46. The corresponding O K-edge spectrum of the electrode surface (electron yield, figure 49c) presented one prominent feature in the pre-edge region at 530 eV, followed by small feature at 532 eV. These changes are consistent with increasing increasing Mn^{2+} and Mn^{4+} contents. Parasitic side reactions at high oxidizing potentials likely contribute to the observed capacity and are the source of increased Mn^{2+} content.

After oxidation to 110 % capacity, the working electrode was reduced to 2 V vs. Li^+/Li^0 at room temperature. In the Mn L_3 region, the features at 640 eV gained significant intensity relative to the other features and the event at 643.5 eV significantly reduced in intensity (figure 48c). The centroid of L_2 further shifted to lower energy. These changes are indicative of the reduction of Mn. The disappearance of Mn^{4+} features at 643.5 eV could be ascribed to the insertion of Li into Mn_2O_4, as proposed based on the electrochemical response. The corresponding O K-edge spectrum of the electrode surface (electron yield, figure 49a-c) presented one prominent feature in the pre-edge region at 530 eV, followed by small feature at 532 eV. The onset of the main edge shifted to lower energy by 1 eV. There was also a notable change in the signals after the absorption edge, where peak intensity ratios changed. The changes reflected the existence of both Mn^{2+} and Mn^{3+} bonds with O^{2-}, consistent with the corresponding Mn $L_{2,3}$-edge spectra. The O K spectrum collected deeper into the electrode (fluorescence yield, figure 49d) showed much more subtle changes throughout, notably a smaller shift of the main edge compared to the oxidized electrode (figure 49e). These results suggest that a gradient in the extent of reduction, which was most extensive at

the first surface layers than the interior (~100 nm) of the electrode. In fact, compared to the theoretical reaction Mn_2O_4-$Li_2Mn_2O_4$ upon reduction to 2 V, it is clear that the surface of the electrode over-reduced.

Subsequent re-oxidation to 5 V vs. Li^+/Li^0 led to a reversible change of the shape of the Mn L_3 region, with an increase in absorption at 640 eV and a re-emergence of the peak at 643.5 eV, and a blue-shift of the centroid of the L_2 event (figure 48d). These changes are indicative of increasing Mn^{3+} and Mn^{4+} contents and, consequently, evidence of Mn oxidation. The O K-edge spectra partly reverted after this second oxidation, especially in terms of the onset of the main edge (Figure 49). The changes were more pronounced at the surface of the electrode (Figure 49a-c) than the interior (Figure 49d-f), reinforcing the idea that the electrochemical reactions are sluggish in the bulk.
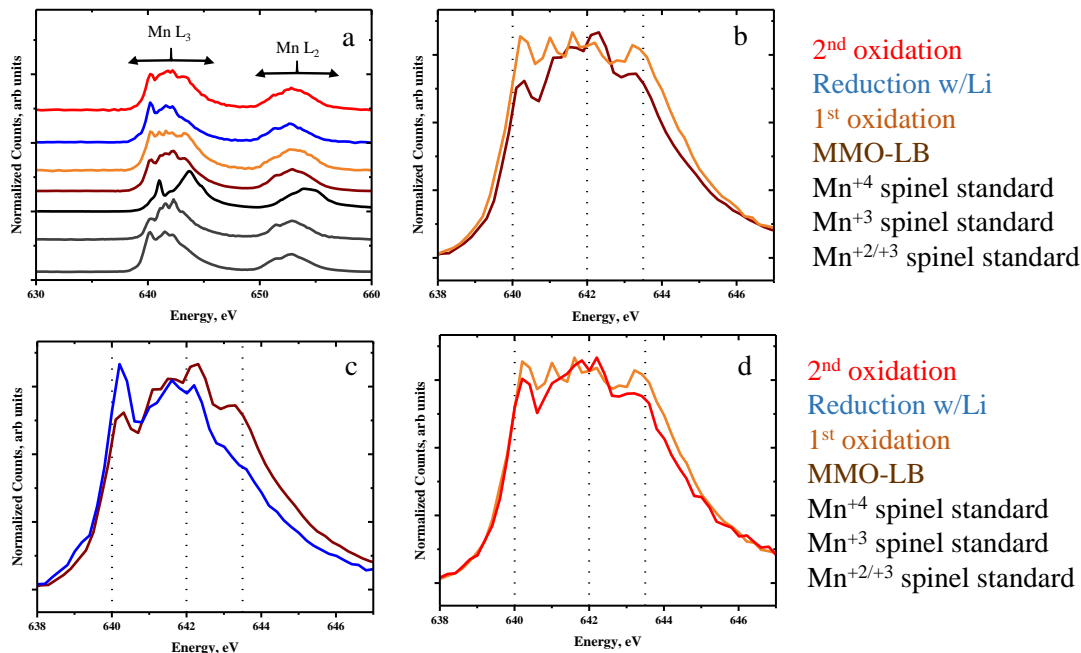
Figure 48. (a) Stacked electron yields at the Mn $L_{2,3}$-edge of MgMn$_2$O$_4$-LB and electrochemically cycled samples in Li coin cell at room temperature, compared to standards of Mn$^{2+/3+}$ (spinel Mn$_3$O$_4$), Mn^{3+} (ordered spinel MgMn$_2$O$_4$), and Mn^{4+} (delithiated spinel Mn$_2$O$_4$), (b) overlay of pristine MgMn$_2$O$_4$-LB compared to first oxidized state, (c) overlay of the as-made MgMn$_2$O$_4$-LB compared to the working electrode reduced in Li electrolyte, and (d) overlay of the first and second oxidized states of the working electrode. Dotted lines near 640, 642, and 643.5 eV are signatures of Mn^{2+}, Mn^{3+}, and Mn^{4+}, respectively.
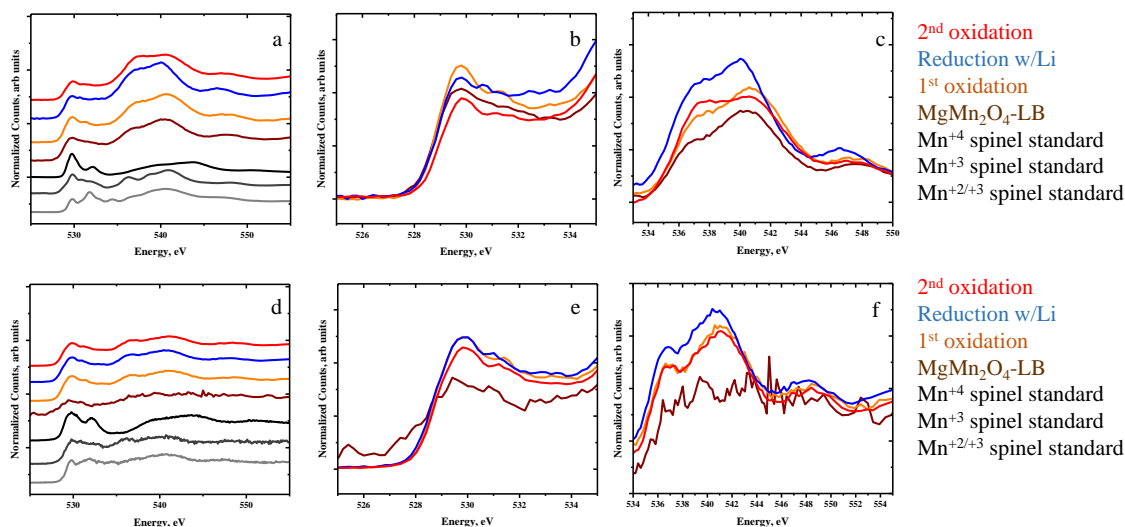
Figure 49. (a,d) Stacked O K-edge spectra of $MgMn_2O_4$-LB and electrochemically cycled samples in Li coin cell at room temperature, compared to standards of $Mn^{2+/3+}$ (spinel Mn_3O_4), Mn^{3+} (ordered spinel $MgMn_2O_4$), and Mn^{4+} (delithiated spinel Mn_2O_4), and overlays of the pre-edge (b,e) and main edge (c,f) regions of pristine $MgMn_2O_4$-LB compared to electrochemically cycled samples. Two different detection modes are shown, electron (a-c) and fluorescence (d-f) that correspond to surface and average in-depth chemical states.

Electrochemical properties in cells at 50 ᵒC.

An increase of the temperature of the experiment should result in increases rates of diffusion according to equation 1.12. The Li coin cell setup was used again to investigate Mg deintercalation through electrochemical oxidation. The working electrode was oxidized to 5 V at 50 ᵒC at C/20 and the electrochemical curve shown in figure 50a. The open circuit voltage of the cell was about 2.4 V vs. Li^+/Li^0 at the start of the experiment. Upon oxidation the potential increased to 3.5 V vs. Li^+/Li^0, then dropped to 3.2 V and leveled off for 25 mAh/g then increased rapidly to 4.8 V vs. Li^+/Li^0 with a small voltage event at 4.1 V vs. Li^+/Li^0. The diffractogram of the completely oxidized $MgMn_2O_4$-LB at 50 ᵒC is

103

shown in figure 50b. Pawley fit determined that the oxidized tetragonal spinel lattice parameters to be a = 5.67562 Å, c = 9.28244 Å, and cell volume of 299.0 Å^3 and the cubic spinel lattice parameter (a) equal to 8.24964 Å and cell volume 561.4 Å^3.

Figure 50. (a) Voltage profile for the electrochemical oxidation of MgMn$_2$O$_4$-LB to 5 V vs. Li$^+$/Li^0 at 50 °C and (b) PXRD patterns of the oxidized samples versus the pristine. Stainless steel peaks have been noted (*) and used at internal reference for peak alignment.

The possibility of Mg intercalation into the oxidized working electrode was subsequently investigated under reducing conditions in a coin cell with a Mg electrolyte. In this coin cell setup, the counter electrode is activated carbon cloth and the electrolyte is Mg-based ionic liquid. The oxidized working electrode was harvested and cleaned, then was reduced to 0.2 V vs. Mg^{2+}/Mg^0 and the electrochemical curve shown in figure 51a. Upon reduction, the voltage of the cell dropped to 0.2 V vs. Mg^{2+}/Mg^0 after 40 mAh/g. There was a voltage plateau for about 30 mAh/g before the cell was stopped. This plateau may be attributed to Mg intercalation or parasitic side reactions. The diffractogram of the

reduced sample is shown in figure 51b. The Bragg reflections of the stainless steel current collector were used an internal standard. There was no significant difference in the observable peaks, with the exception of a loss of the signal with respect to the noise, suggesting loss of crystallinity due to degradation. The signal to noise ratio was too poor to perform a Pawley fit.
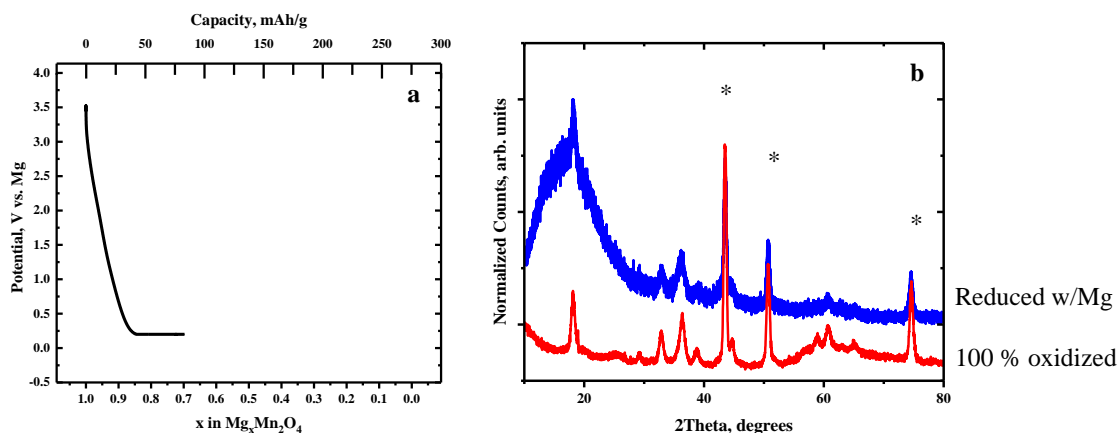
Figure 51. (a) Voltage profile for the electrochemical reduction of 100 % oxidized $MgMn_2O_4$-LB to 0 V vs. Mg^{2+}/Mg^0 at 50 $^{\circ}$C and (b) PXRD patterns of the oxidized samples versus the reduced one. Stainless steel peaks have been noted (*) and used at internal reference for peak alignment.

X-ray absorption spectroscopy at the Mn $L_{2,3}$- and O K-edges on working electrodes of $MgMn_2O_4$-LB electrochemically oxidized in Li-containing electrolyte and then reduced in Mg-containing electrolyte are shown in figure 52. The Mn $L_{2,3}$-edges of samples are compared to standards in figure 52a, whereas the pristine and electrochemically cycled $MgMn_2O_4$-LB are overlaid in figures 52b,c. Upon complete oxidation, the prominent absorption events at 640 and 643.5 eV grew in intensity relative to the

other absorption events in the L_3 region, especially the latter, and the centroid of the L_2 shifted by 0.5 eV to higher energy. These changes are indicative of increasing Mn^{2+} and Mn^{4+} contents. There appeared to be a greater degree of Mn^{4+} generated at 50 °C compared to electrochemical oxidation at 25 °C. After reduction in Mg cell, the L_3 region underwent a severe change in shape where the event at 640 eV grew in intensity at the expense of the signal at 643.5 eV. Furthermore, the center of gravity L_2 red-shifted to lower energy by 1 eV. This spectrum is similar to reduction in Li coin cell at room temperature (figure 48b) as well as MnO seen in the literature.[94] Therefore, these changes are associated with increasing Mn^{2+} and decreasing Mn^{4+}.
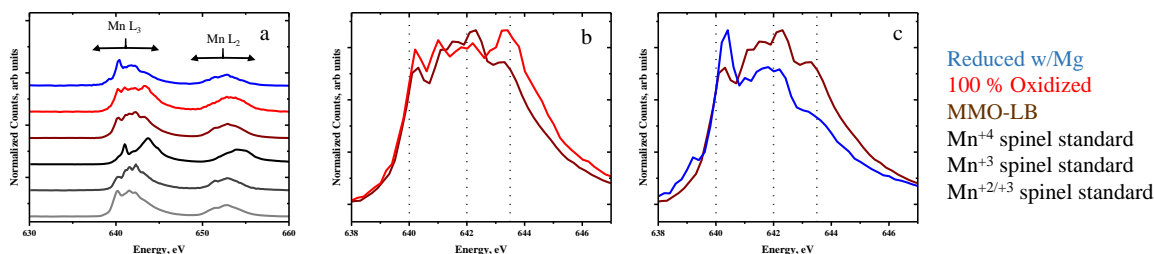
Figure 52. (a) Stacked electron yields at the Mn $L_{2,3}$-edge of $MgMn_2O_4$-LB and electrochemically cycled samples in Li coin cell at 50 °C, compared to standards of $Mn^{2+/3+}$ (spinel Mn_3O_4), Mn^{3+} (ordered spinel $MgMn_2O_4$), and Mn^{4+} (delithiated spinel Mn_2O_4), (b) overlay of pristine $MgMn_2O_4$-LB compared to fully oxidized state, and (c) overlay of the as-made $MgMn_2O_4$-LB compared to the working electrode reduced in ionic liquid Mg electrolyte. Dotted lines near 640, 642, and 643.5 eV are signatures of Mn^{2+}, Mn^{3+}, and Mn^{4+}, respectively.

Oxidation to 100 % (electron yield, figure 53ab) resulted in the evolution of two maxima in the O K pre-edge region. These two maxima are separated by 2 eV which is the crystal field splitting energy, the main absorption edge shifted to higher energy by 1 eV (figure 53c). The crystal field splitting energy is the difference in energy between the d orbitals of Mn due to the electric field produced by surrounding Mg and O. These results indicate that Mn oxidized on the surface, supporting Mn $L_{2,3}$-edge findings. Similar changes were seen in the fluorescence yield but to a lesser degree, supporting the overarching theme that the surface of these particles is more reactive that the bulk. Upon reduction in the Mg electrolyte, the O K-edge spectrum of the surface of the electrode (electron yield, figure 53a-c) underwent a significant shape change, leading to a single feature centered at 533 eV in the pre-edge region, with a notable shift of the absorption edge to higher energy than the oxidized electrode. These changes are reminiscent of Mn^{+2} reference.[94] In the fluorescence yield (figure 53d-f), the O K-edge showed a single prominent peak at 530 eV. The main edge peaks red-shifted by 1 eV; which is indicative of a slight reduction of Mn toward +3. Reduction in ionic liquid Mg electrolyte over-reduced the surface of the working electrode particle compared to the bulk.
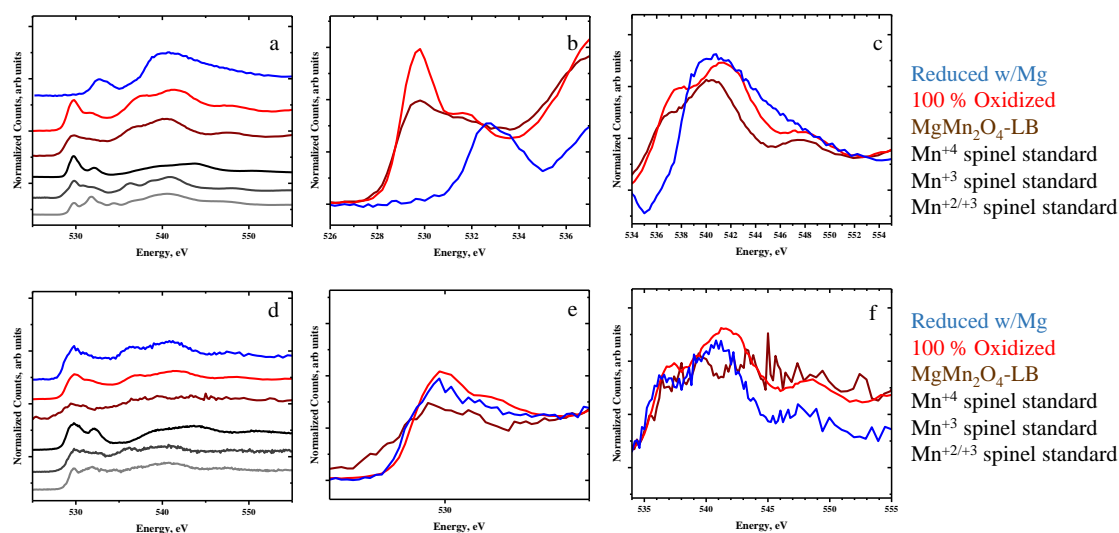
Figure 53. (a,d) Stacked O K-edge spectra of MgMn$_2$O$_4$-LB and electrochemically oxidized in Li coin cell and reduced in ionic liquid Mg electrolyte at 50 °C, compared to standards of Mn$^{2+/3+}$ (spinel Mn$_3$O$_4$), Mn^{3+} (ordered spinel MgMn$_2$O$_4$), and Mn^{4+} (delithiated spinel Mn$_2$O$_4$), and overlays of the pre-edge (b,e) and main edge (c,f) regions of pristine MgMn$_2$O$_4$-LB compared to electrochemically cycled samples. Two different detection modes are shown, electron (a-c) and fluorescence (d-f) that correspond to surface and average in-depth chemical states.

5.3.2 REACTION WITH Mg ACETATE IN A SMALL BATCH (SB)

Given that the issues of co-existence of two crystal structures related to Mg-Mn-O in the original attempts of synthesis (LB) were ascribed to improper mixing, the reaction was downscaled to afford increased control over reagent dispersion. The experimental parameters are discussed in chapter 2. Powder X-ray diffraction of pristine MgMn$_2$O$_4$-SB was consistent with a tetragonal spinel structure, with no other impurities (Figure 54). Pawley analysis determined cell parameters a = 5.72717 Å, c = 9.25990 Å (space group *I41/amd* PDF#:00-023-0392), and cell volume of 303.73 Å^3. These lattice constants were

close to pure particles in the literature,[88] but, compared to the tetragonal spinel phase found in the large batch, a subtle decrease in a and an increase in c led to an overall reduction of 1% of the cell volume. Representative TEM images of the $MgMn_2O_4$-SB nanocrystals and a histogram of particle size distribution are shown in Figure 55a,b, respectively. Synthesis of parent MnO 8 ± 3 nm quasicubes is discussed in chapter 4. In contrast, primary particles of $MgMn_2O_4$-SB consisted of 13 ± 5 nm quasicubes, indicating an increase in volume upon transformation to the Mg-containing oxide. Secondary agglomerates of primary particles formed, amounting to several hundred nanometers.
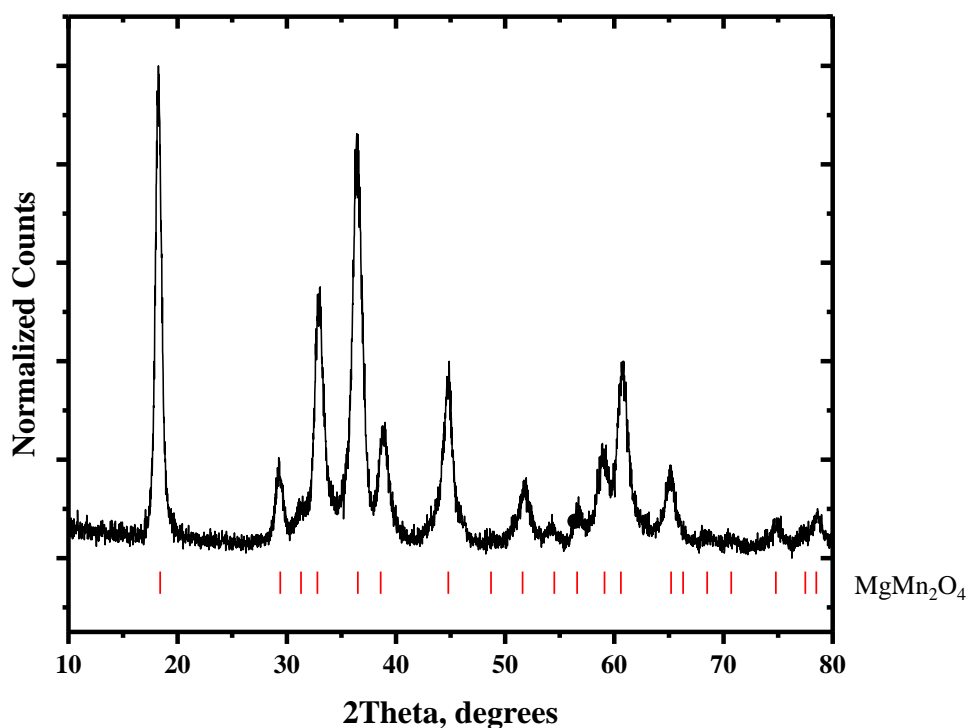
Figure 54. PXRD of $MgMn_2O_4$-SB. Reference Bragg reflections correspond to tetragonal spinel $MgMn_2O_4$.
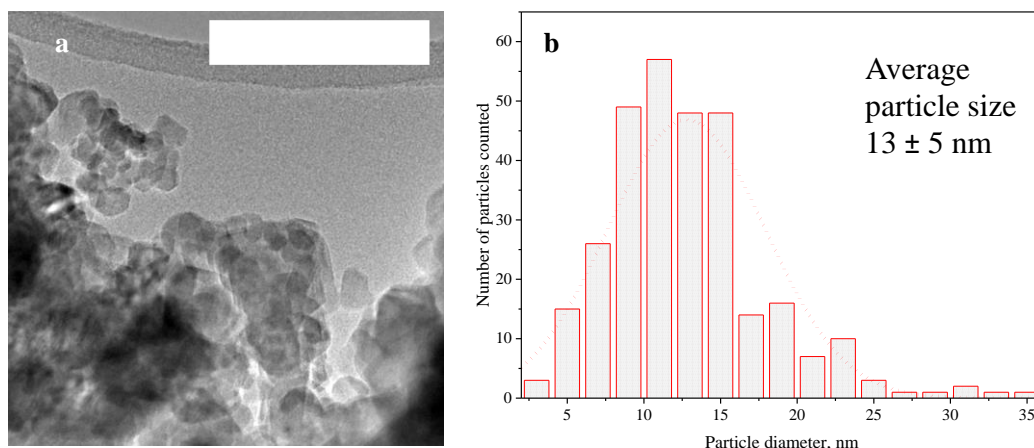
Figure 55. TEM image of (a) MgMn$_2$O$_4$-SB product and (b) histogram of particle size distribution. Scale bar is 100 nm.

As with MgMn$_2$O$_4$-LB, electrochemical oxidation of MgMn$_2$O$_4$-SB was attempted in Li coin cells at 50°C (figure 56a). The electrochemical response was similar between separate runs at the same experimental conditions. The potential first spiked to 3.7 V then fell to a plateau at 3.3 V for about 55 mAh/g. Then, the potential raised again, asymptotically trending toward 4.8 V vs. Li$^+$/Li^0. Two working electrodes were harvested after reaching 60 and 100 % completion of the theoretical capacity oxidation of the oxide, to hypothetical compositions of Mg$_{0.4}$Mn$_2$O$_4$ and Mg$_0$Mn$_2$O$_4$. The PXRD patterns of those electrodes are shown in figure 56b. Pawley fits on the pattern of the states at 60 % and 100% led to lattice parameters a = 5.71988 Å, c = 9.26970 Å (cell volume = 303.277 Å^3) and 5.72115 Å, c = 9.25975 Å (cell volume = 303.086 Å^3), respectively. Compared to the pristine state, the values were considered too close to be significantly outside the error of the measurement, especially taking into account the large width of the diffraction peaks.
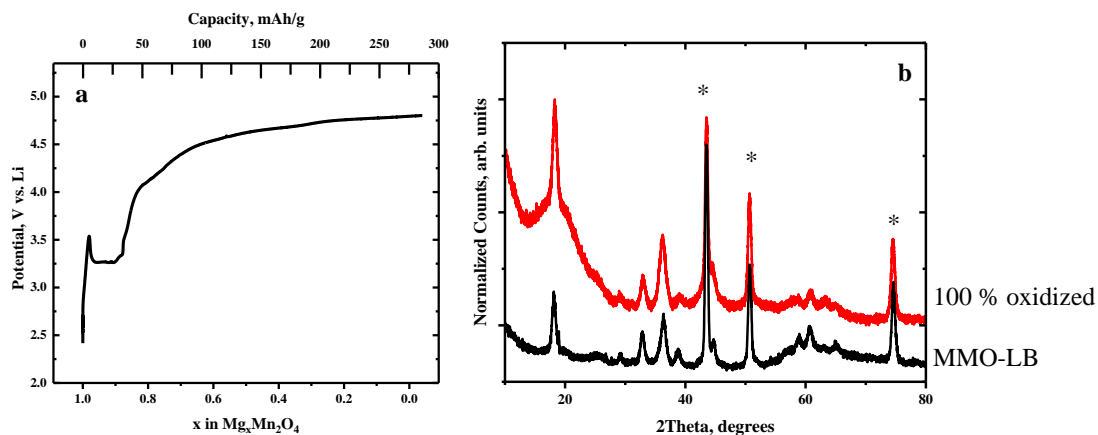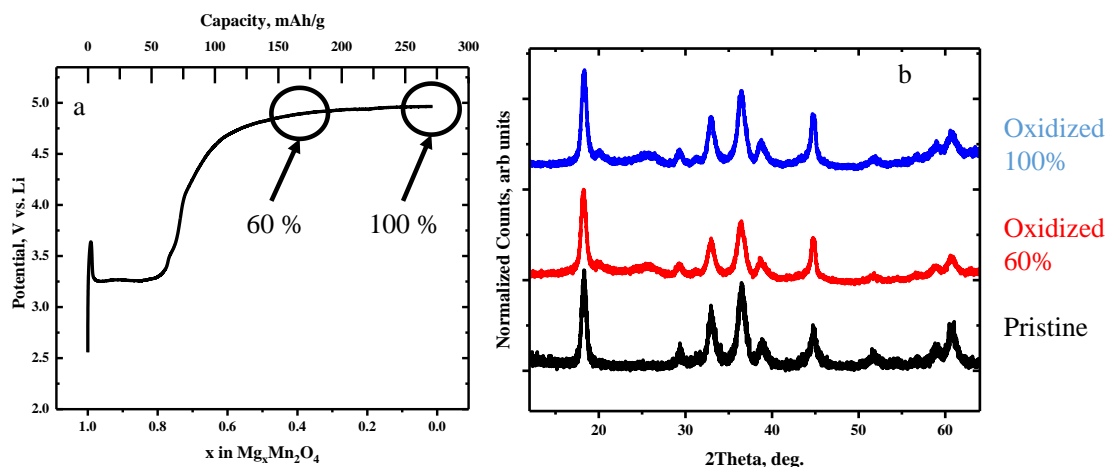
Figure 56. (a) Voltage profile for the electrochemical oxidation of $MgMn_2O_4$-LB to 5 V vs. Li^+/Li^0 at 50 °C and (b) PXRD patterns of the oxidized samples versus the pristine.

X-ray absorption spectroscopy at the Mn $L_{2,3}$- and O K-edges on working electrodes of $MgMn_2O_4$-SB electrochemically oxidized in Li cells are shown in figure 57. The Mn $L_{2,3}$-edge spectra of pristine $MgMn_2O_4$-SB was very close to the standard of ordered, spinel $MgMn_2O_4$, with five distinguishable maxima in the L_3 region between 640 and 645 eV, the most prominent peak being at 642.3 eV, followed by a L_2 absorption event with a center of gravity near 653 eV, and a shoulder near 651 eV (figure 57b). Oxidation resulted in changes in peak intensity of the many maxima in the L_3 region (figure 57c, d). The absorption events at 643.5 grew in intensity relative to the other peaks. This change is indicative of increasing Mn^{4+} content. These shape of these features match well with the standard delithiated spinel Mn_2O_4; which corresponds to Mn oxidation.[97] However, a shoulder at 640 eV was noted even at 100% oxidation (Figure 57d), suggesting that Mn^{2+} was also forming on the surface of the electrode. Also, the center of gravity of L_2 feature further blue-shifted to 654 eV, further indication of Mn oxidation. However, this was still 1 eV lower in energy than the Mn^{4+} standard.

111

Pristine $MgMn_2O_4$-SB featured an O K pre-edge with three peaks in similar position to Mn^{3+} standard (figure 58a,b). The presence of multiple peaks in the pre-edge is consistent with the splitting of 3d states due to the presence of a Jahn−Teller distortion,[52] as expected for ordered $MgMn_2O_4$. Upon oxidation to 100 %, the spectrum of the surface of the electrode progressively developed intense features at 530 and 532 eV. These peaks were separated by 2.4 eV. Also, the main edge broadened and its center of gravity blue-shifted to higher energy by 2 eV. These new spectral features were similar to the Mn_2O_4 (Mn^{+4}) standard, consistent with a dominant oxidation of the surface. The changes were much less pronounced in the interior of the electrode (figure 58d-f). Due to the size of the cathode nanocrystals, this observation indicates that oxidation of Mn occurred throughout the particles of $MgMn_2O_4$-SB.
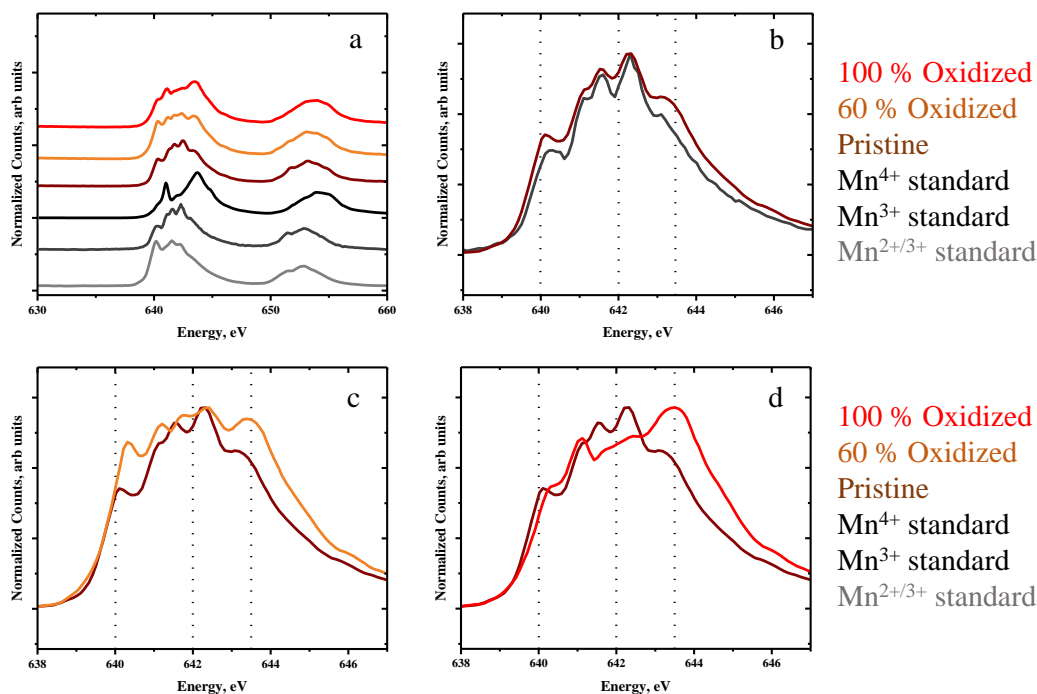
Figure 57. (a) Stacked electron yields at the Mn $L_{2,3}$-edge of $MgMn_2O_4$-SB and electrochemically oxidized samples, compared to standards of $Mn^{2+/3+}$ (spinel Mn_3O_4), Mn^{3+} (ordered spinel $MgMn_2O_4$), and Mn^{4+} (delithiated spinel Mn_2O_4), (b) overlay of pristine $MgMn_2O_4$-SB compared to ordered $MgMn_2O_4$, (c) overlay of the as-made $MgMn_2O_4$-LB compared to 60 % oxidized electrode, and (d) overlay of the as-made $MgMn_2O_4$-LB compared to 100 % oxidized electrode. Dotted lines near 640, 642, and 643.5 eV are signatures of Mn^{2+}, Mn^{3+}, and Mn^{4+}, respectively.
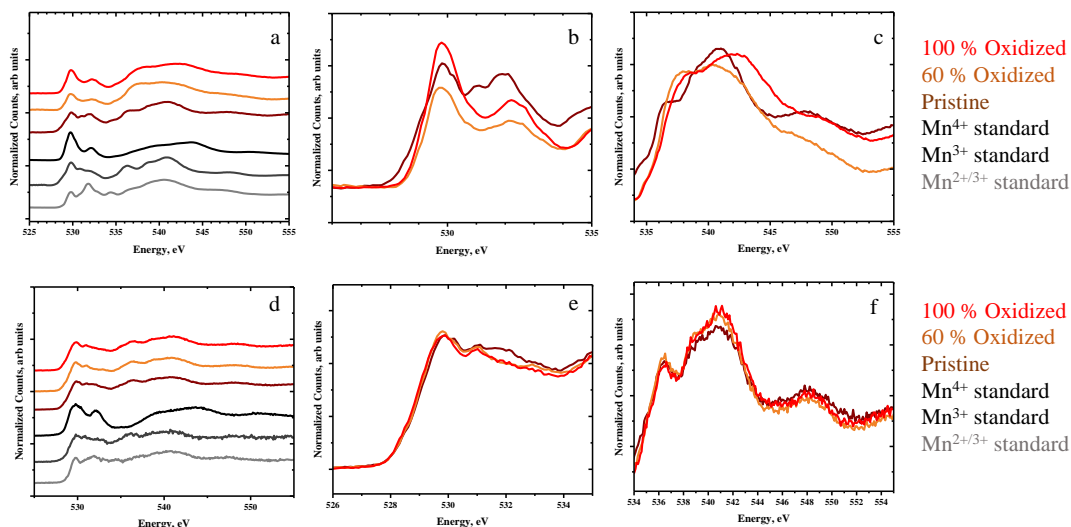
Figure 58. (a,d) Stacked O K-edge spectra of MgMn$_2$O$_4$-SB and electrochemically oxidized samples, compared to standards of Mn$^{2+/3+}$ (spinel Mn$_3$O$_4$), Mn^{3+} (ordered spinel MgMn$_2$O$_4$), and Mn^{4+} (delithiated spinel Mn$_2$O$_4$), and overlays of the pre-edge (b,e) and main edge (c,f) regions of pristine MgMn$_2$O$_4$-SB compared to electrochemically oxidized samples. Two different detection modes are shown, electron (a-c) and fluorescence (d-f) that correspond to surface and average in-depth chemical states. Working electrodes were oxidized at 50 °C in Li coin cells.

5.4 DISCUSSION

Nanocrystals of MnO were reacted with Mg(ac)$_2$ in two different batch sizes, large (LB) and small (SB). LB was 5 times larger in mass than SB. Following LB synthesis, a mixed phase product was obtained containing both tetragonal MgMn$_2$O$_4$ and cubic Mg$_2$Mn$_2$O$_4$ spinel phases. The mixture of phases in the product likely stemmed from inhomogenities in the precursor mixture when it was mixed by hand. Reducing batch size and improving precursor mixing resulted in a single phase product of tetragonal spinel MgMn$_2$O$_4$. Subsequent XAS demonstrated the exclusive presence of Mn^{3+}, indicative of an ordered

spinel with Mg^{2+} and the transition metal in the tetrahedral and octahedral sites, respectively. Calcination resulted in an increase in particle size by about 100 % for both LB and SB syntheses, but the final product still had primary particles of less than 20 nm in diameter.

Electrochemical testing of $MgMn_2O_4$ was mainly completed using Li coin cells due to the lack of Mg-based electrolytes with sufficient anodic stability to explore the oxidative deintercalation of Mg^{2+}. The electrochemical responses to oxidation showed high capacities, but oxidation of Mn was modest in comparison. When a mixture of cubic and tetragonal spinel phases was present ($MgMn_2O_4$-LB) Mn oxidation was concentrated primarily on the surface of the electrode compared to the interior or bulk. Pushing the anodic potential only exacerbated side reactions of other cell components, such as the electrolyte, which actually reduced the surface of the electrode instead. Electroanalysis provided evidence that some Mn_2O_4 was formed, but it could not subsequently be reduced in a Mg^{2+} ionic liquid to provide evidence of intercalation. In comparison, $MgMn_2O_4$-SB showed much clearer evidence of the formation of mostly Mn^{4+}, both in the surface and in the bulk. Although no changes in structure could be detected, the redox changes would be consistent with deintercalation. Overall, the observations would be consistent with computational predictions indicating that Mg mobility is higher in ordered Mn_2O_4 than when Mg/Mn inversion is present. However, to fully ascertain the reactivity of this material, it is vital that better Mg electrolytes are developed so that these experiments can be conducted with greater ease.

5.5 CONCLUSIONS

The electrochemical reactivity of ordered and disordered spinel type $MgMn_2O_4$ nanocrystals was evaluated in nonaqueous electrolytes. Following charging to anodic potentials, spectroscopic studies were able to identify explicit Mn oxidation, which was more widespread and pronounced in the ordered material. Unfortunately, despite the high anodic stability of the electrolytes used, evidence of side reactions between the working electrode and electrolyte were also evident. Therefore, while the results suggest that ordered $MgMn_2O_4$ nanocrystals can reversibly intercalate Mg^{2+}, further development

electrolytes with high anodic and chemical stabilities are needed to fully elucidate the extent and reversibility of this reaction.

6 SYNTHESIS, CHARACTERIZATION AND ELECTROCHEMICAL PROPERTIES OF CaFe₂O₄-TYPE MANGANESE OXIDES

6.1 INTRODUCTION

Over a quarter of a century ago, the structural transition from spinel-type to calcium ferrite-type ($CaFe_2O_4$) was found to occur upon heating the mineral called "spinel" ($MgAl_2O_4$) at high pressure (~25 GPa).[98] The denser "post-spinel" phase is supposed to be an important host for Al in the Earth's lower mantle, which is subject to extreme temperature and pressure. The spinel $LiMn_2O_4$ has also been reported to undergo a phase transition to an $CaFe_2O_4$ structure type after being heated to 1500 °C at 6 GPa.[56] This post-spinel was determined to be 6 % denser than the spinel and with a Li-deficient composition of $Li_{0.92}Mn_2O_4$; however, a minor impurity phase of Li_2MnO_3 was observed as well. In the $CaFe_2O_4$ structure type, all Mn ions are coordinated by 6 O in an octahedral formation and the Li is 8-fold coordinated with O to form bicapped trigonal prisms. The LiO_8 sites connect via to form large unidimensional tunnels that support facile Li ion transport. Conversely, while the normal spinel $LiMn_2O_4$ has all Mn in similar octahedral environments, Li remains coordinated by four O in an network of three dimensional tunnels.

As discussed in chapter 1, generally, spinel compounds can undergo "post-spinel" phase transitions at high pressure to polymorphs with $CaFe_2O_4$, $CaMn_2O_4$ or $CaTi_2O_4$ structure types. First principles calculations were used to study the relative stability of the three possible post-spinel polymorphs of $LiMn_2O_4$, $NaMn_2O_4$ and $MgMn_2O_4$, as well as their applications as rechargeable battery systems.[41] Interestingly, for each composition, the $CaFe_2O_4$ structure type systematically possesses the highest cationic mobility of the three studied. In fact, the calculated activation energy of the migration of Li^+ and Mg^{2+} ions in the tunnels of the $CaFe_2O_4$ structure type are lower than that of Li^+ mobility in typical Li-ion battery cathodes, indicative of a facile process. Mamiya et al. reported that the electrochemical performance of $CaFe_2O_4$-type $LiMn_2O_4$ as positive electrode in secondary battery systems is dependent on its preparation method.[99] When made by exchanging Na by Li in the $NaMn_2O_4$ counterpart, the charge carrier capacity was an order of magnitude greater, with excellent cyclability, compared to a material made directly in the Li form at high pressure. The origin of this discrepancy was

not addressed in literature reports, so it remains an open question. On the other hand, Na deintercalation from $CaFe_2O_4$-type $NaMn_2O_4$ is possible, with an initial discharge capacity of 83 mAh/g and 94 % capacity retention in the voltage range of 4.8 – 1.5 V,[100] although significant contents of carbon had to be added to improve electronic conductivity.

Within the past decade, researchers have developed direct methods to synthesize $CaFe_2O_4$-type $LiMn_2O_4$. It was found that, by heating carbonate or oxide precursors of Li and Mn, at 4.5 GPa and lower temperatures than 1500 C, the $CaFe_2O_4$ phase could be made with excellent purity.[99,101] High pressure syntheses of the Na polymorph of this compound have been reported.[100–102] Researchers found that heating Na_2O_2 and Mn_2O_3 in a 1:1 molar ratio at 4.5 GPa resulted in an ordered $CaFe_2O_4$-type $NaMn_2O_4$ product. Additionally, it has been found that even softer methods may be used to prepare $CaFe_2O_4$-type $LiMn_2O_4$ when reacting $CaFe_2O_4$-type $NaMn_2O_4$ with $LiNO_3$ as molten salt at 360 C for 12 h in air.[99,101] It is not possible to synthesize $CaFe_2O_4$-type $MgMn_2O_4$ and test Mg^{2+} ion mobility directly because the more stable form at high pressure is $CaMn_2O_4$, which is predicted to have a much higher activation barrier for Mg^{2+} migration than in the $CaFe_2O_4$ framework.[41]

In the present study, $CaFe_2O_4$-type $LiMn_2O_4$ was prepared via both Na/Li ion exchange from $CaFe_2O_4$-type $NaMn_2O_4$ and directly using high pressure synthesis. Their electrochemical properties were compared, confirming the dramatically improved capacity for the ion-exchanged material. To elucidate the causes of this difference, powder X-ray diffraction and X-ray absorption spectroscopy studies were completed, pointing at a critical role of surface defects that block cation transfer. Taking advantage of the possibility of generating $CaFe_2O_4$-tye Mn_2O_4 by electrochemical deintercalation, the possibility of intercalating Mg^{2+} ions into the structure was also investigated, in a high-temperature cell using an ionic liquid electrolyte. The results point towards complex chemical reactions that happen to the working electrode during electrochemical reduction, but that include intercalation of the divalent ion. These observations provide new insight into the key aspects that govern the ability of hosts to electrochemically intercalate cations with different charge.

6.2 EXPERIMENTAL METHODS

Details on the methods of synthesis of $LiMn_2O_4$ and $NaMn_2O_4$ at high pressures are provided in chapter 2. Na/Li exchange from $NaMn_2O_4$ was conducted at 350°C for 8 hr in molten $LiNO_3$ with a mass ratio of 1:20, contained in a platinum crucible.

Details about the methods of characterization can be found in chapter 2. Galvanostatic cycling in Li and Mg cells was completed at 25 and 50 °C. Structural characterization was completed using powder X-ray diffraction using both $\lambda_{avg} = 0.412647$ and 1.5418 Å radiation. Scanning, transmission and scanning transmission electron microscopes were used to characterize particle size and morphology. X-ray absorption spectroscopy was used to characterize Mn $L_{2,3}$- and O K-edges. X-ray transmission spectroscopy was used to characterize Mn K-edges.

6.3 DIRECT SYNTHESIS OF $CaFe_2O_4$-TYPE $LiMn_2O_4$

High resolution powder X-ray diffraction, incident wavelength of 0.41 Å, was used to determine the crystal structure and purity of the samples. The synthesis procedure for $CaFe_2O_4$-type $LiMn_2O_4$ is detailed in chapter 2. The precursor molar ratio of Li:Mn was 0.8:2 to form nominally $Li_{0.8}Mn_2O_4$. For brevity, it will be referred to as $LiMn_2O_4$ in this chapter. Other ratios of precursor mixtures were attempted, but this ratio led to the product with the highest purity. Tokiwa et al. determined the composition of powder made by high-pressure methods at 4.5 GPa to be $Li_{0.69}Mn_2O_4$ by indicatively coupled plasma mass spectrometry.[101] However, in that report, the amounts of precursors were not explicitly provided. In contrast, Yamaura et al. estimated a composition $Li_{0.92}Mn_2O_4$ by Rietveld analysis of neutron data of powder made using precursors of $LiCO_3$ and Mn_2O_3 in a molar ratio of Li:Mn as 0.9:2, although it cannot be considered as quantitative and it is unclear why more Li was evident in the product than precursor mixture.[56]

The results of Rietveld refinement for $LiMn_2O_4$ mounted in the form of an electrode (see, again, chapter 2) are shown in figure 59a and Table III. The as-made sample contained a small amount of Mn_2O_3 and a second phase with low crystallinity, which came from other components of the electrode and filter paper used to mount the sample. The latter peaks were excluded from the refinement (see, e.g., weak

119

signals at 9.1 and 11.7 º). The refinement was carried out in a 2θ range of 4.74 – 30 º, with an excluded region at 5.60 – 6.66 º. Lattice cell parameters were determined to be a = 8.7770(1) Å, b = 2.84002(1) Å, c = 10.655(9) Å and a cell volume of 265.68 Å^3. These parameters agreed with other single-step syntheses of $Li_xMn_2O_4$ with $CaFe_2O_4$ structure-type reported in the literature, where 0.69 < x < 1 mol Li was claimed as described above.[56,99,101] The close values of cell parameters in all cases suggest that, in fact, all the available information is for very similar x. Analysis of the atomic positions revealed the existence of small amounts of Mn in the Li site (3% ± 1.5). As Li positions and occupancies are not refineable by XRD due to the fact that Li is a poor scatterer of X-rays, the possibility that these defects are due to crystallographic Li/Mn exchange, as opposed to migration of the Mn to vacancies in the Li position, could not be established. It must be noted that Tokiwa et al. found evidence of site exchange between Li/Mn in $CaFe_2O_4$-type in nuclear magnetic resonance studies as well.[101]

Anisotropic strain in the lattice was identified in $LiMn_2O_4$. Strain was required to fit peaks in Rietveld analysis and is reported in table III. Structural strain can be caused by the defects such as site exchange or site vacancies, but their origin could not be established. Due to anisotropy in unit cell, strains relax more effectively in some directions than in others. The lowest strain was found in the b direction. Due to the low strain value, cations are expected to be mobile along tunnels in the b direction.

Scanning electron microscope imaging was used to characterize particle size and morphology. $LiMn_2O_4$ was a black powder composed of primary particles that have quadratic prism-like shapes 4 x 2 x 2 um (Figure 59b). These primary particles aggregate to form larger secondary particles with diameters larger than 4 microns and rough facets. These particles compare well to other reports.[56]
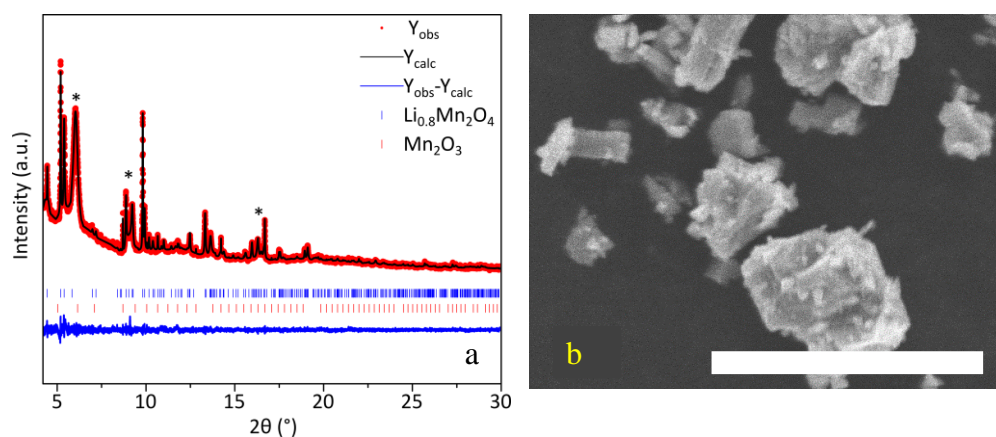
Figure 59. (a) Rietveld refinement of $LiMn_2O_4$. The red dots are the experimental data, the blue line the simulated one and the blue one their difference. Blue markers are the Bragg reflections for $LiMn_2O_4$ while red ones are for Mn_2O_3. The star (*) denotes impurity peaks. (b) Scanning electron miscroscopy images of $LiMn_2O_4$. Scale bar is 10 μm.

Table IV. Results from Rietveld refinement of $LiMn_2O_4$.

	Agreement factors			
	R_p	R_{wp}	R_e	χ^2
	28.4	26.2	22.2	1.4
$Li_{0.8}Mn_2O_4$	Structural parameters			
	Space group	a (Å)	b (Å)	c (Å)	size (nm)
	Pnma	8.7770(12)	2.84002(14)	10.6585(9)	>500
	Anisotropic strains*	S200	S020	S002	Average*
		87	13	47	47(19)

Mn₂O₃ impurity %	1.42(7)			
Atomic positions				
Atom	**x**	**y**	**z**	**Occupancy**
Mn1	0.061(2)	0.25	0.117(2)	1
Mn2	0.081(2)	0.25	0.602(1)	0.97(2)
Li1	0.216(14)	0.25	0.37(2)	0.8
Mn3	0.216(14)	0.25	0.37(2)	0.030(16)
O1	0.313(6)	0.25	0.651(5)	1
O2	0.380(5)	0.25	0.977(5)	1
O3	0.460(7)	0.25	0.197(4)	1
O4	0.076(8)	0.25	0.926(4)	1

*The high standard deviation of the average anisotropic strain is the measure of the degree of anisotropy,

not of the estimated error.

X-ray absorption spectroscopy at the Mn $L_{2,3}$-, Mn K- and O K-edges on pristine powder samples was collected and shown in figure 60 and 61. The Mn $L_{2,3}$-edge spectra in figure 60a are compared to oxides with known oxidation states of Mn. Overlaid spectra of all the pristine post-spinel materials are in figure 60b. The Mn $L_{2,3}$-edge surveys the chemical state of Mn by characterizing Mn 2p electron transitions to unfilled Mn 3d orbitals. Only electron yields were measured because the fluorescence signal was severely affected by deleterious self-absorption events. Electron yields correspond to chemical states within the first few nanometers below the surface of the particle. The L_3 event has many fine features and the significant absorption events will be noted. $LiMn_2O_4$ had many spectral lines contribute to a large event in the L_3 absorption region between 640 and 645 eV. The energy position of the first maximum ($\sim$ 640 eV) was similar to that of spinel Mn_3O_4, but the spectrum had significant intensity at 643.5 eV, where the Mn_2O_4 standard shows its dominant feature. This alludes to the presence of of Mn^{2+}, Mn^{3+} and Mn^{4+} on the material surface. These spectral events were followed by a L_2 absorption event with a center of gravity near 653 eV, which, through comparison with the standards, provides further evidence of reduced Mn at the surface.

X-ray absorption spectroscopy at the Mn K-edge probes electron transitions from Mn 1s orbital to the Mn 2p orbitals. The Mn K-edge position, a traditional indicator of oxidation state, of $LiMn_2O_4$ is intermediate between the Mn_2O_3 and MnO_2 standards (figure 60c). This observation suggests that the average oxidation state of the electrode material lies between +3 and +4, which is consistent with Rietveld analysis. Since the standards do not have the same crystal structure as $CaFe_2O_4$-type $LiMn_2O_4$, variations in lineshape can occur that reflect local coordination rather than redox state, which precludes precise quantification.

Two maxima were evident in the pre-edge region of the O K-edge of $LiMn_2O_4$ (below 535 eV) when fluorescence (bulk sensitivity) was detected, which is similar to Mn^{+4} standard material (figures 61ab). However, the linewidths were larger than in the standard, reflecting the high dispersion of states in the Mn^{3+} standard. The splitting of signals in this reflects the distorted octahedral ligand field and exchange energy and was calculated to be 2.3 eV. The detection of electrons was unreliable and is not

discussed. There was a small absorption event at 535 eV which was reminiscent of a similar signature in the Mn^{3+} standard. The main event was broad (FWHM ~ 10 eV) and had an edge position at 536 eV. The main edge position of $LiMn_2O_4$ is red-shifted compared to Mn^{4+} reference, indicative of the oxidation state of Mn to be between +3 and +4 throughout the bulk, supporting Mn K-edge XAS.

Overall, these results suggest that the bulk of the $LiMn_2O_4$ has close to the expected stoichiometry of Li to Mn. However, Mn $L_{2,3}$-edge analysis identified Mn^{2+} at the surface. Tetragonal spinel Mn_3O_4 is reported to undergo a phase transition at high pressure and crystallize in the $CaMn_2O_4$-type post-spinel structure.[103] In this material, the octahedrally coordinated sites are occupied by Mn^{3+} and the eight-fold coordinated sites are occupied by Mn^{2+}. Therefore, in the as-prepared $LiMn_2O_4$, it is possible that there could be domains reminiscent of post-spinel Mn_3O_4, reflecting a deficiency of lithium, at the surface of the particles.
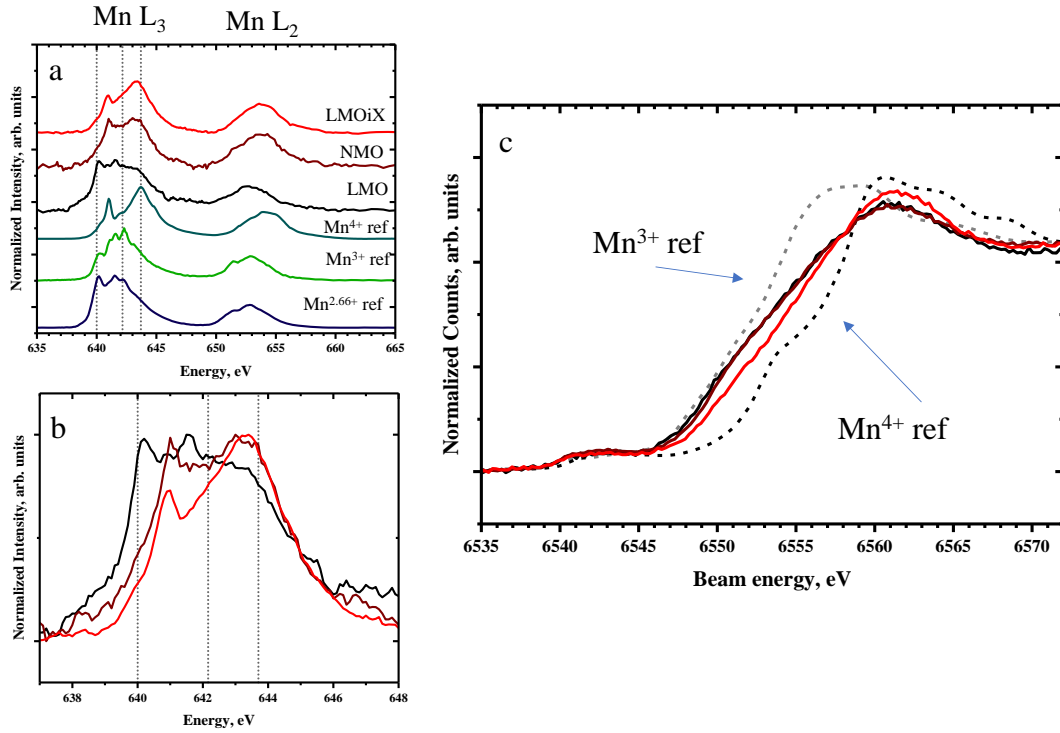
Figure 60. (a) Mn $L_{2,3}$-edge XAS of as-made post-spinel samples compared to (a) Mn spinel-type standards or (b) each other, measured with an electron detector. The reference spectra for $Mn^{2.66+}$, Mn^{3+}, and Mn^{4+} are tetragonal spinel Mn_3O_4, tetragonal spinel $MgMn_2O_4$ and delithiated spinel Mn_2O_4, respectively. Dotted lines near 640, 642, and 643.5 eV are signatures of Mn^{2+}, Mn^{3+}, and Mn^{4+}, respectively. (c) Spectra of pristine samples collected in transmission mode at the Mn K-edge at the University of Washington. The standards of Mn^{3+} and Mn^{4+} are bixbyite Mn_2O_3 and rutile MnO_2. LMO, NMO, and LMOiX correspond to $CaFe_2O_4$-type $LiMn_2O_4$, $NaMn_2O_4$, and $LiMn_2O_4$-iX.
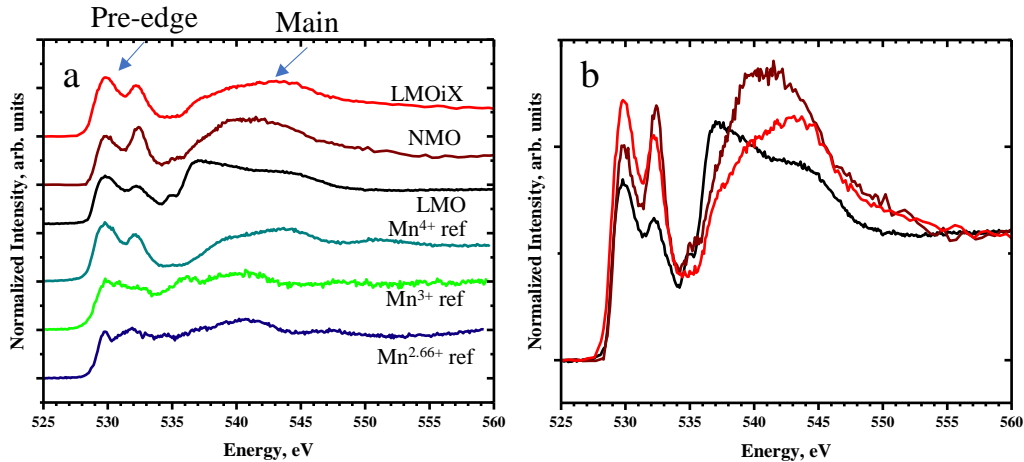
Figure 61. O K-edge XAS of as-made post-spinel samples compared to (a) Mn spinel-type standards or (b) each other, measured with a fluorescence detector. The reference spectra for $Mn^{2.66+}$, Mn^{3+}, and Mn^{4+} are tetragonal spinel Mn_3O_4, tetragonal spinel $MgMn_2O_4$ and delithiated spinel Mn_2O_4, respectively. LMO, NMO, and LMOiX correspond to $CaFe_2O_4$-type $LiMn_2O_4$, $NaMn_2O_4$, and $LiMn_2O_4$-iX.

$LiMn_2O_4$ was oxidized to 5 V vs. Li^+/Li^0 at 25 °C in Li metal half cell (Figure 62a). During oxidation, voltage plateaus were observed at 3.25 and 4.2 V vs. Li^+/Li^0, followed by an asymptotic increase in potential until the cutoff. The final cumulative capacity was 34 mAh/g, which is only one third of the theoretical capacity of 118 mAh/g.[99] Powder X-ray diffraction (Figure 62b) revealed only slight changes in peak intensity ratios in the 30 – 40 ° 2θ region between pristine and oxidized states, with other Bragg reflections remaining largely unchanged. In order to assess the need for thermal activation, the electrochemical reaction was carried out at 50 °C (Figure 63a). In this case, the profile showed no discernible plateaus from open circuit at 3.0 V until reaching 4.6 V vs. Li^+/Li^0, where approximately 90 mAh/g accumulated and the experiment was stopped. The cell was subsequently cycled (Figure 63b). Upon discharge to 2 V vs. Li, only 18 mAh/g reached (12.2 % theoretical) at 3 V vs. Li^+/Li^0 and 57

mAh/g (39.1 % theoretical) at 2 V vs. Li$^+$/Li^0. Re-oxidation completed after reaching 4.7 V vs. Li$^+$/Li^0 and

a capacity of 90 mAh/g was observed. However, the electrochemical profile was substantially different

from the first oxidation, with half of the capacity accumulating below 3.5 V vs. Li$^+$/Li^0. The capacity

accumulated in the first charge increased when the sample was ball-milled (figure 64b), with a final

oxidative capacity of 148 mAh/g. This value was higher than theoretical (118 mAh/g), suggesting the

presence of parasitic side reactions that account for the additional capacity.
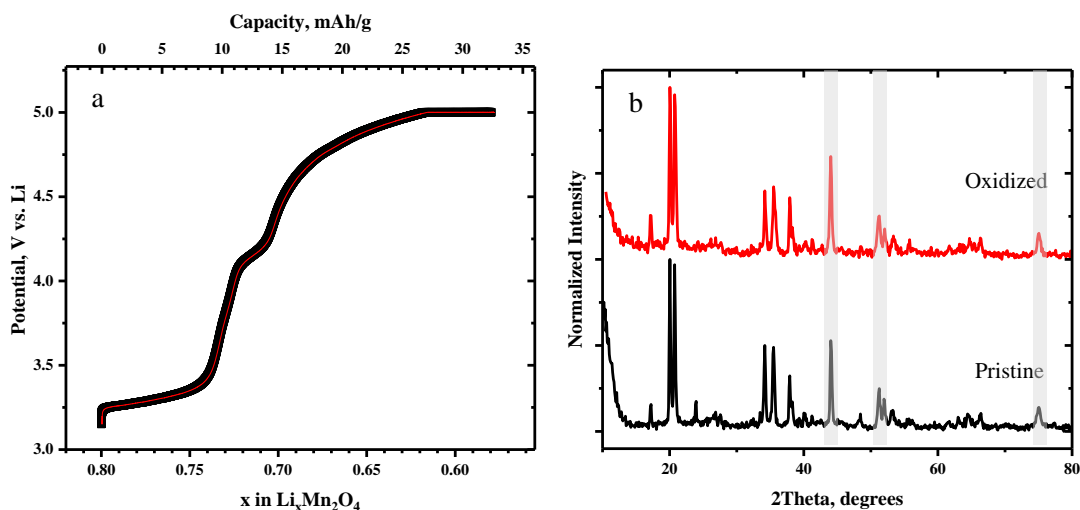
Figure 62. (a) Galvanostatic oxidation of LiMn$_2$O$_4$ to 5 V in Li coin cell at a current rate of C/50 and at 25

°C and (b) PXRD of working electrodes prior to and after oxidation using $\lambda = 1.54$ Å. Shaded regions

represent Bragg reflections from stainless steel.

Electrochemical activation was also explored by ballmilling the as-made powder prior to making

an electrode. TEM image (figure 64a) indicates that ball-milling reduced particle size and introduced

fractures. The PXRD pattern of the ball-milled electrode was acquired after oxidation (figure 65a). No new reflections were observed, and the pattern could be fit with a space group Pnma and unit cell parameters a = 8.78417 Å, b = 10.64240 Å, c = 2.82512 Å, with cell volume = 264.105 Å^3. These lattice parameters were not much different from the pristine material. The Mn L$_{2,3}$-edge spectrum of the surface of the oxide after ballmilling also resembled the pristine material. In contrast, the spectrum of the oxidized electrode (figure 65b) greatly resembled the Mn$_3$O$_4$ reference sample, with a prominent first maximum at 640.1 eV, followed by many smaller events until about 645 eV. The L$_2$ absorption event red-shifted by 1 eV compared to the pristine state. These findings indicate that Mn at the surface was significantly reduced during electrochemical oxidation. It strongly suggests that the electrochemical oxidation is plagued by parasitic side reactions that inadvertently reduce the surface of the particle, with net electron production coming from other components of the cell, such as the electrolyte. All in all, increasing thermal energy and ball-milling with carbon did not improve the electrochemical properties of LiMn$_2$O$_4$.
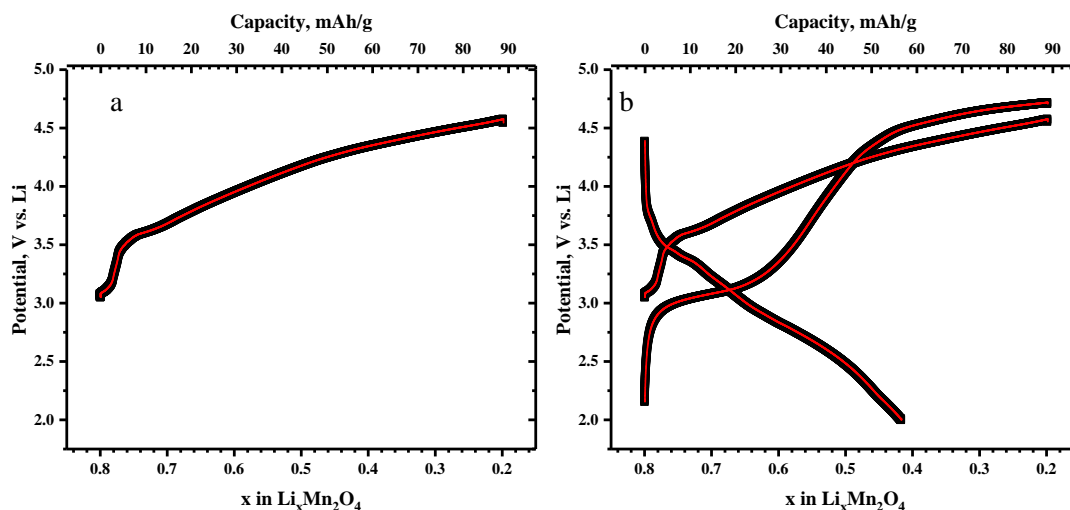
Figure 63. Galvanostatic (a) oxidation and (b) oxidation-reduction reactions of LiMn$_2$O$_4$ in Li coin cell.

Experiments were completed at a current rate of C/50 and at 50 °C
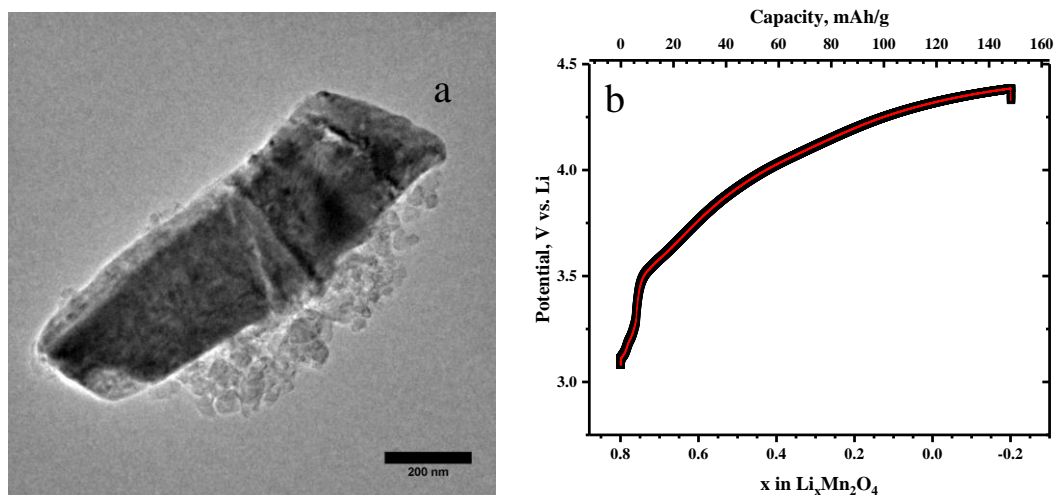
Figure 64. (a) TEM image of LiMn₂O₄ ball-milled in a 1:1 mass ratio with C for 12 hours at 500 RPM.

Scale bar is 200 nm. (b) Galvanostatic oxidation curve of ball-milled LiMn2O4 in Li coin cell with a

current rate of C/20 and at 50 °C.
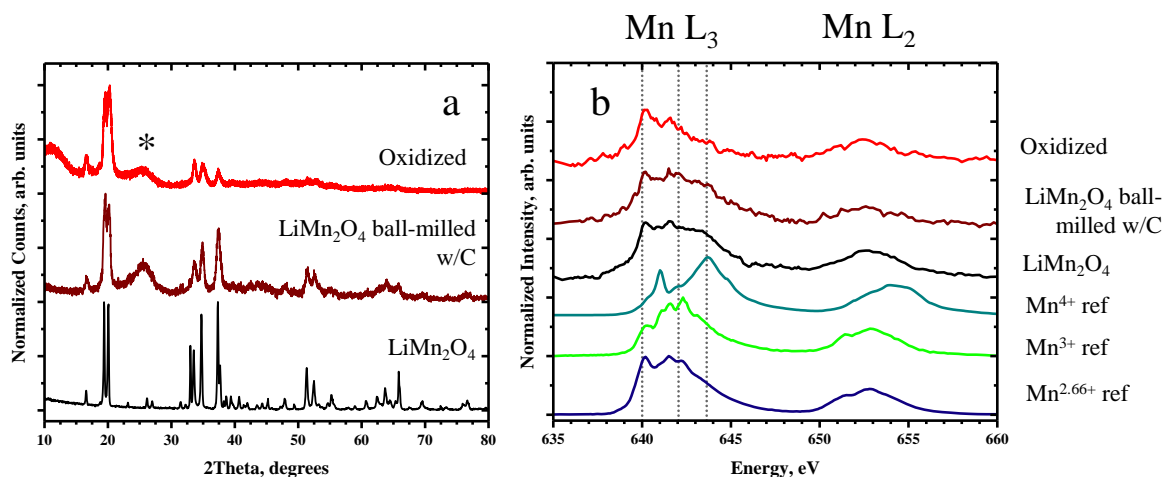
Figure 65. (a) PXRD of samples using $\lambda = 1.54$ Å and * corresponds to C. (b) Mn $L_{2,3}$-edge XAS spectra in electron yield of the samples compared to tetragonal spinel Mn_3O_4 and delithiated spinel Mn_2O_4 reference materials. The reflection at 25 ° was assigned to the presence of carbon in the sample.

6.4 CATION EXCHANGE METHOD TO FORM CaFe₂O₄-TYPE LiMn₂O₄ (LiMn₂O₄-IX)

Reports exists where Na and Li cations are exchanged in $CaFe_2O_4$-type $NaMn_2O_4$ to form $LiMn_2O_4$ with higher electrochemical activity than a material made directly in Li form.[99] $CaFe_2O_4$-type $NaMn_2O_4$ was synthesized according to the experimental section. The PXRD pattern of $NaMn_2O_4$ is shown in figure 66a, and the results of Rietveld refinement is shown in table IV. This sample has an orthorhombic unit cell (space group Pnma) and lattice cell parameters were determined to be a = 8.8894(3) Å, b = 2.8482(1) Å, c = 11.258(5) Å, for a cell volume of 265.05 Å³. These parameters compare well with other reports that synthesized this material.[100–102] Despite the sample exhibiting some reflections at very low intensity that are attributed to poorly crystalline impurities, only one phase was used to refine this pattern. The unit cell volume of $NaMn_2O_4$ is approximately 7 % larger than $LiMn_2O_4$, as expected from the larger ionic radius of Na^+ than Li^+. The occupancy of sodium atoms was initially left to vary, but since it did not result in any significant improvement of the refinement it was finally fixed to

130

its nominal value. However, alkali metal/manganese exchange was also tried in both samples and it was found that $NaMn_2O_4$ showed a 9% crystallographic exchange, resulting in a final composition of $[Na_{0.91(9)}Mn_{0.090(9)}][Mn_{1.91(9)}Na_{0.090(9)}]O_4$.

Na was exchanged by Li by dispersing $NaMn_2O_4$ in molten $LiNO_3$ to create crystalline $LiMn_2O_4$ (herein $LiMn_2O_4$-iX) with the calcium ferrite-type structure. Both powders were black and composed of needle-like particles with diameters of 100 – 500 nm and lengths of 2 – 5 μm. (Figures 66b and 66d), indicating that the ion exchange process had no effect on morphology. In both cases, particle size and morphology compare well to earlier reports.[99] [100,102] The results of Rietveld refinement of the XRD pattern of $LiMn_2O_4$-iX are shown in figure 66c and table V. The oxide has an orthorhombic unit cell with space group Pnma, and lattice cell parameters a = 8.715(2) Å, b = 2.837(4) Å, c = 10.531(3) Å, with a cell volume of 260.4 $Å^3$. Despite again exhibiting some reflections at very low intensity attributed to impurities, only one phase was used to refine this sample. These parameters compare well with other reports of $LiMn_2O_4$ synthesized via ion exchange methods.[99,101] The unit cell is smaller in comparison with $LiMn_2O_4$ prepared by single-step, especially in the a and c directions (0.70% for a, 0.09% for b and 1.19% for c). Two possible explanations are possible for the volume shrinkage: i) a difference in the occupation of the Li site as vacancies occupy less crystallographic space, ii) an increase in average Mn oxidation state in the ion exchanged sample, which would reduce the ionic radius in the transition metal site. Indeed, Mamiya et al. identified that only up to 0.81 molar amount of Li was present in the post-spinel lattice after exchange based on inductively coupled plasma mass spectrometry resulting in nominal $Li_{0.81}Mn_2O_4$.[99] These results indicate that both effects are in place, as the Li deficiency would be compensated by Mn in the ion-exchanged product being more oxidized than in the single-step product. Since Li scatters X-rays poorly, Li site occupancy was fixed to 1 for simplicity in the Rietveld refinement. The refinement also revealed that there was no evidence of Mn in the Li sites, in contrast with the material made directly in Li form at high pressure. There was also no evidence of vacancies in the Mn site. This observation suggests that the temperature and the large concentration of Li in the cation exchange reaction were sufficient for Li to exchange with Na and to reallocate all Mn in the 6-fold

131

coordinated site. Anisotropic strain broadening was required to fit peak profiles in Rietveld analysis for

$NaMn_2O_4$ and $LiMn_2O_4$-iX. Overall, strain was the lowest for $NaMn_2O_4$, which can be explained by the

larger atomic distances due to the larger size of Na^+ helping to partially release the stress caused by high

pressures. Also, since there is no site Mn at the Li site in the ion-exchange product, which reduces

structural strain compared as-prepared $LiMn_2O_4$.
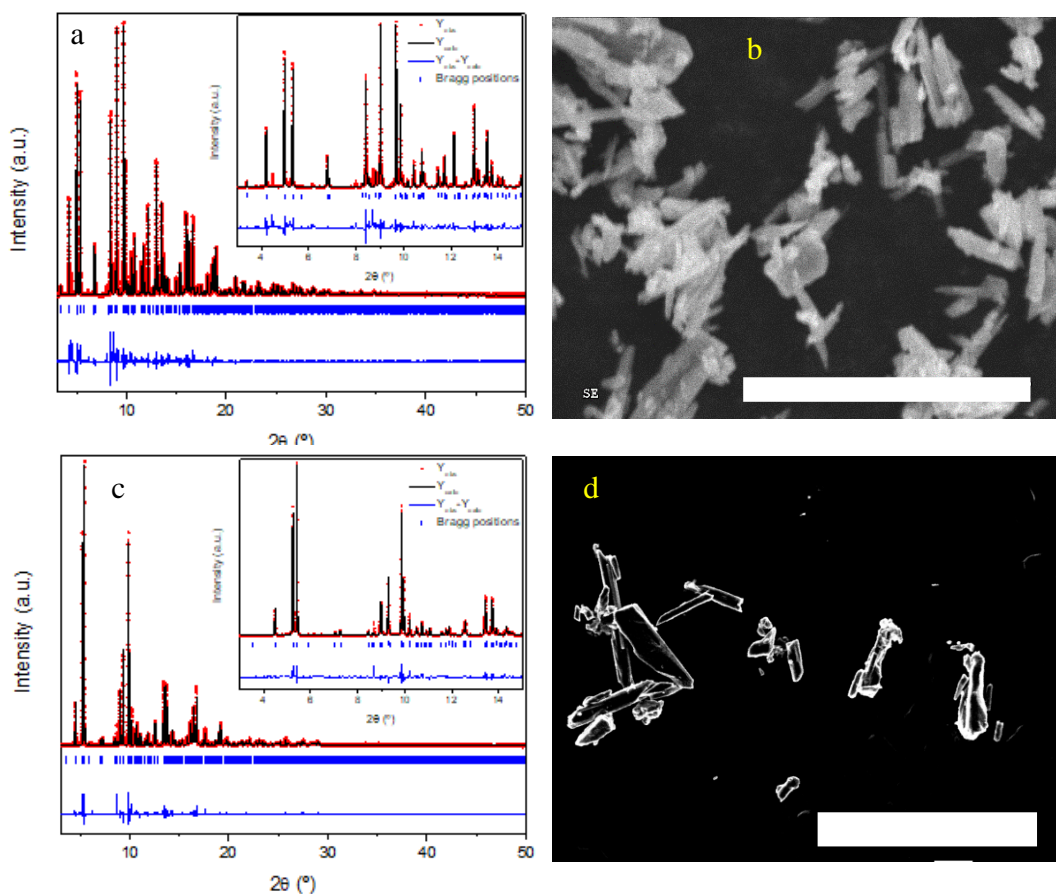
Figure 66. (a) Rietveld refinement of $NaMn_2O_4$. The red dots are the experimental data, the blue line the

simulated one and the blue one their difference. (b) Scanning electron miscroscopy images of $NaMn_2O_4$.

(c) Rietveld refinement of $LiMn_2O_4$-iX. (d) Scanning electron miscroscopy images of $LiMn_2O_4$-iX. Scale

bar is 10 μm.

Table V. Results from Rietveld refinement for $NaMn_2O_4$.

	Agreement factors				
	R_p	R_{wp}	R_e	χ^2	
	15.5	20.9	7.04	8.821	
	Structural parameters				
	Space group	a (Å)	b (Å)	c (Å)	size (nm)
	Pnma	8.8894(3)	2.8482(1)	11.2585(4)	352(2)
	Anisotropic strains*	S200	S020	S002	Average
		15.5187	8.3151	18.4295	14(3)
	Atomic positions				
	Atom	x	y	z	Biso ($Å^2$)	Occupancy
$NaMn_2O_4$	Na1	0.249(2)	0.25	0.335(1)	1.5(5)	0.910(2)
	Mn1	0.249(2)	0.25	0.335(1)	1.5(5)	0.090(2)
	Mn2	0.0731(9)	0.25	0.1091(5)	0.4(1)	0.910(2)
	Na2	0.0731(9)	0.25	0.1091(5)	0.4(1)	0.090(2)
	Mn3	0.0798(9)	0.25	0.5943(5)	0.3(1)	0.910(2)
	Na3	0.0798(9)	0.25	0.5943(5)	0.3(1)	0.090(2)
	O1	0.286(3)	0.25	0.641(2)	0.6(5)	1
	O2	0.384(2)	0.25	0.982(2)	0.3(5)	1
	O3	0.475(3)	0.25	0.198(2)	-0.2(4)	1
	O4	0.065(3)	0.25	0.914(2)	0.6(5)	1

Table VI. Results from Rietveld refinement for $LiMn_2O_4$-iX.

	Agreement factors			
	R_p	R_{wp}	R_e	χ^2
	14.4	17	6.45	6.917
	Structural parameters			
	Space group	a (Å)	b (Å)	c (Å)	size (nm)
	Pnma	8.7152(3)	2.8374(1)	10.5313(4)	>500
	Anisotropic strains*	S200	S020	S002	Average
		22.6221	8.7287	36.6345	23 (7)
$LiMn_2O_4$	**Atomic positions**			
	Atom	x	y	z	Biso (Å^2)	Occupancy
	Li1	0.278	0.25	0.37	0.127	1
	Mn2	0.0605(5)	0.25	0.1168(4)	0.8(1)	1
	Mn3	0.0844(5)	0.25	0.5998(4)	0.64(9)	1
	O1	0.295(2)	0.25	0.653(2)	0.3(3)	1
	O2	0.383(2)	0.25	0.983(2)	0.6(3)	1
	O3	0.472(2)	0.25	0.207(2)	0.3(3)	1
	O4	0.077(2)	0.25	0.923(1)	0.9(3)	1

The Mn $L_{2,3}$-edge spectra of the surface of pristine $NaMn_2O_4$ and $LiMn_2O_4$-iX are shown in figures 60ab. These spectra had two maxima in the L_3 absorption region at 641 and between 643 – 644 eV, followed by a L_2 absorption events with centers of gravity near 654 eV. Comparison with standards revealed similarities in the shapes of the L_3 region, especially the absorption at 644 eV, to spinel Mn_2O_4, which are evidence of high Mn^{4+} content at the surface. For both $NaMn_2O_4$ and $LiMn_2O_4$-iX, there was also significant absorption near 642 eV, which is evidence of Mn^{3+}. The L_2 events for both samples have centers of gravity at 654 eV, which is blue-shifted compared to $LiMn_2O_4$ indicating that the oxidation state of Mn in $NaMn_2O_4$ and $LiMn_2O_4$-iX is higher than $LiMn_2O_4$ on the surface but not quite completely Mn^{4+}.

The Mn K-edge position of $NaMn_2O_4$ and $LiMn_2O_4$-iX is intermediate between the Mn^{3+} and Mn^{4+} empirical standards (figure 60c). This observation indicates that the oxidation states of Mn in the complex oxides lie between +3 and +4. The position of the edge and shape of the spectrum of $NaMn_2O_4$ is very similar to $LiMn_2O_4$, suggesting similar local electronic structures around the Mn atoms in the bulk average of both systems. On the other hand, the Mn K-edge position of $LiMn_2O_4$-iX blue-shifted compared to $LiMn_2O_4$ and $NaMn_2O_4$; which suggests that Mn in the bulk in the ion-exchanged product is more oxidized than the as-prepared samples. This observation is consistent with differences in occupancy in the Li/Na site, which are compensated by changes in oxidation state of Mn.

There were two maxima evident in the pre-edge region of O K-edge of both $NaMn_2O_4$ and $LiMn_2O_4$-iX in fluorescence yield (figures 61ab). Signals detected from electron yield were not reliable and are not discussed. The relative intensity of the two maxima in the pre-edge region for $NaMn_2O_4$ was inverted compared to $LiMn_2O_4$ and with slightly higher splitting energy (2.5 eV). These signals reflect the t_{2g}-e_g hybridized states in a highly octahedral environment. The difference in intensity reflects a subtle difference in electron distribution that should be explored with the aid of band structure calculations. The relative intensity of these peaks are similar to reports of Mn_2O_3,[104] where the expected Jahn-Teller distortion of the octahedron around Mn^{3+} can be frustrated.[105] Since the presence of mixed Mn^{3+} and Mn^{4+} in the ternary oxides studied prevents a Jahn-Teller distortion, the binary oxide is a better comparison

135

than spinel $MgMn_2O_4$, where Mn^{3+} is Jahn-Teller distorted and the degeneracy of Mn 3d-O 2p hybridized orbitals is lifted from the octahedral case. The main edge, which depends on the ionization of the material, had a strong absorption feature at 540 eV. O K-edge spectra indicate that Mn in the bulk of $NaMn_2O_4$ is more reduced than the surface, which is consistent with Mn K-edge and XRD analysis. Upon cation exchange, the relative intensity of the two maxima in the pre-edge region flipped again and looked relatively similar to Mn^{4+} standard spectra. Also, the main event broadened and blue-shifted to 542. This is evidence that Mn in $LiMn_2O_4$-iX is in a higher oxidation state than a $LiMn_2O_4$ and $NaMn_2O_4$, which is consistent with Mn K-edge analysis.

The electrochemical performance of $NaMn_2O_4$ is reportedly poor,[100] so it was not evaluated. The electrochemical properties of the $LiMn_2O_4$-iX were characterized between 3 - 4.2 V vs. Li^+/Li^0 and at a charge rate of C/10 (figure 67a). The cell was initially oxidized and had a capacity of 85 mAh/g. The initial capacity upon oxidation was slightly smaller than the following reduction capacity (93 mAh/g) but is in good agreement with the literature.[99] The larger capacity on reduction is evidence that the structure can intercalate more Li^+ than it started with, which would further support the existence of vacancies in the Li site of the initial structure. The oxidation-reduction profile is dominated by a voltage plateau at 3.8 V vs. Li^+/Li^0, which is attributed to the $Mn^{+3/+4}$. The favorable kinetic properties of Li intercalation are manifested by the very low polarization at C/10 (20 mV) and the subsequent rate capability (figure 67b). There was no capacity fade following 20 cycles, which alludes to the chemical stability of this material to reversibly intercalate Li^+. The working electrode was repeatedly cycled between 3 – 4.2 V vs. Li^+/Li^0 at charge rates from C/10 to 10 C. The larger current density (10 C) resulted in a diminished discharge capacity of around 45 mAh/g, or over 48% of the capacity at C/10. However, the system rebounded to the initial discharge capacity once it returned to a slower charge rate of C/10. Considering that the primary particles were several microns in the longest dimensions and that no efforts of electrode optimization where made, these results provide evidence of the inherently notable electronic and ionic conductivity in the high-pressure form of $LiMn_2O_4$ with a $CaFe_2O_4$ crystal structure.
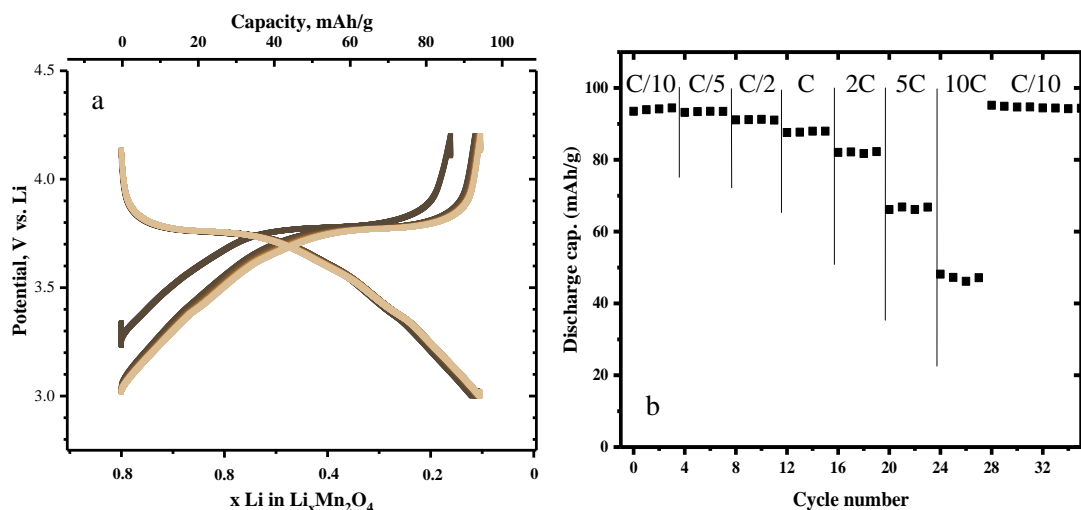
Figure 67. (a) Reversible galvanostatic cycling curves of $LiMn_2O_4$-iX (nominal composition $Li_{0.8}Mn_2O_4$) at rate of C/10 at 25 ºC and (b) rate capability results. The first cycle is shown in (a) as dark color and as the working electrode is cycled the color of the curve gets lighter. Twenty cycles are shown.

From these results of electrochemical cycling of $LiMn_2O_4$-iX working electrodes in Li cell, the kinetics of Li^+ diffusion appear to be improved from as-prepared $LiMn_2O_4$. Mg^{2+} is also predicted to have good mobility in $CaFe_2O_4$-type Mn_2O_4 structure. Therefore, the possibility of Mg^{2+} intercalation in CF-type Mn_2O_4 structures was investigated. First, a $LiMn_2O_4$-iX working electrode was oxidized to 4.2 V vs. Li^+/Li^0 in Li metal half-cell at current rate of C/20 at 25 ºC (figure 68a). In theory, roughly 93 % of Li^+ was removed following electrochemical oxidation, resulting in a theoretical composition of $Li_{0.07}Mn_2O_4$ and Mn with an average oxidation state of +3.9. The oxidized $LiMn_2O_4$-iX working electrode was subsequently reduced at 50 ºC in a coin cell with activated carbon cloth as counter electrode and an ionic liquid electrolyte containing Mg^{2+} (figure 68b). The reduction was cut after 20 hours, which would

137

correspond to the theoretical capacity. At the beginning, there was a drop in the measured voltage until about 0.1 V vs. Mg^{2+}/Mg^0 (-2.1 V vs. ACC) (25 mAh/g). Then a voltage plateau started at 0 V vs. Mg^{2+}/Mg^0 and was observed over a gravimetric capacity of 285 mAh/g (net discharge capacity is 310 mAh/g). PXRD characterization was completed on the electrochemically tested samples (figure 68c). Upon oxidation in Li coin cell, the Bragg reflections changed from the pristine pattern. Pawley analysis determined that the lattice parameters of the oxidized working electrode are a = 8.65 Å, b = 2.74 Å, c = 10.43 Å, and volume = 256.3 $Å^3$. Oxidizing resulted in shrinking of the unit cell volume by 1.6 %, but no change in crystal structure, consistent with topotactic Li^+ deintercalation. Reducing in a Mg cell resulted in further changes to the Bragg reflections. The lattice parameters of the reduced working electrode were a = 8.80 Å, b = 2.86 Å, c = 10.64 Å and 267.7 $Å^3$. This unit cell volume increased by about 4.4 % relative to the oxidized sample. However, this shift was accompanied by notable losses in Bragg reflection intensity. To evaluate the possibility of a chemical reaction between electrode and ionic liquid being the at the origin of this intensity loss, an oxidized working electrode was allowed to rest in Mg electrolyte for 30 hours at 110 ºC. These conditions are more extreme than the electrochemical test of 20 hours at 50 ºC. No significant changes were observed when the corresponding PXRD (λ = 1.54 Å) was compared to the as-oxidized electrode (figure 69), indicating that the changes observed in the cells are due to electrochemical reactions.
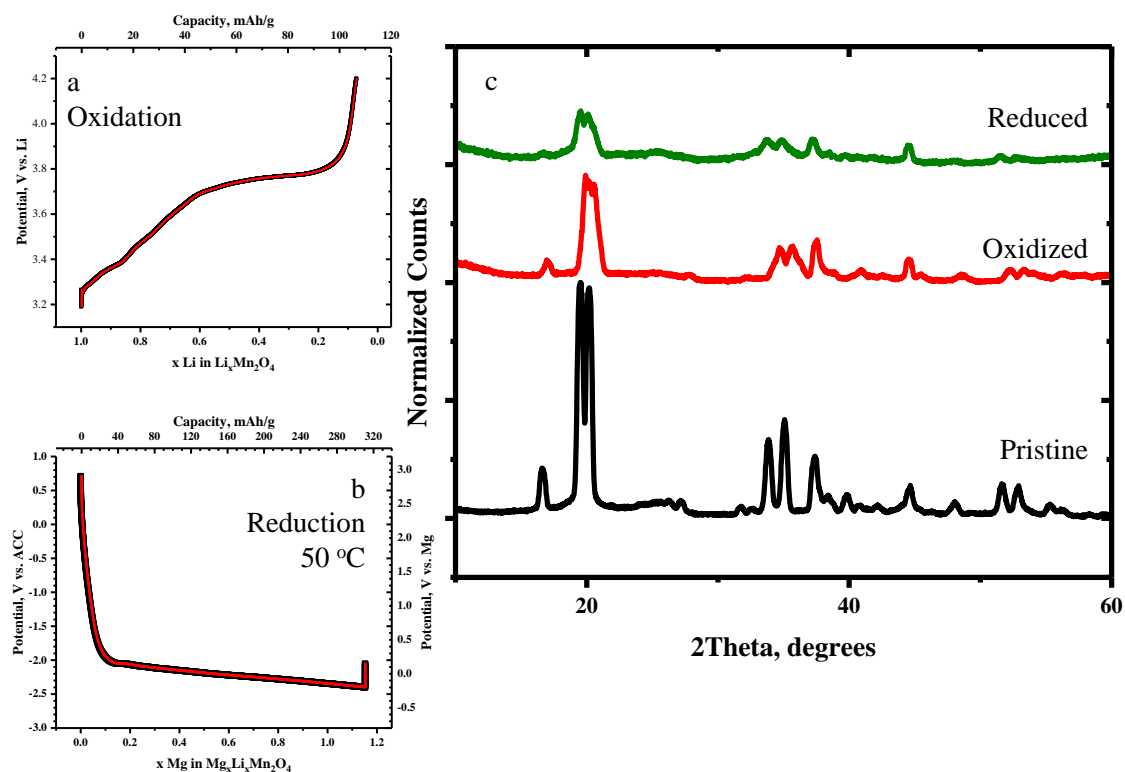
Figure 68. Electrochemical curves of LiMn$_2$O$_4$-iX (a) oxidized in Li cell at 25 $^\circ$C and then (b) reduced in Mg ionic liquid electrolyte at 50 $^\circ$C. (c) PXRD patterns of electrochemically tested samples.
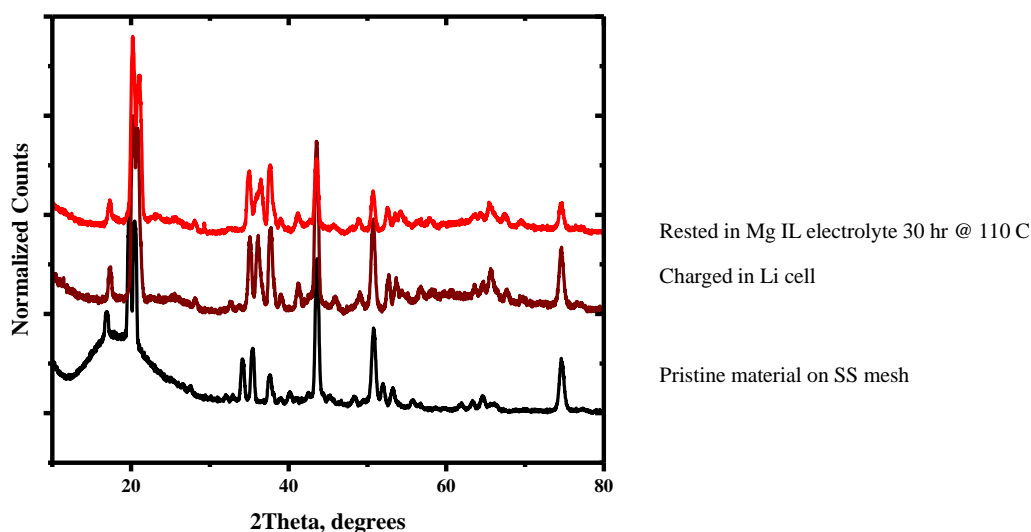
Figure 69. PXRD of pristine LiMn$_2$O$_4$-iX compared to oxidized working electrode and an oxidized

working electrode rested in Mg electrolyte. Stainless steel peaks were used to align peaks.

Transmission electron microscopy coupled with energy dispersive spectroscopy was completed

on working electrodes reduced in ionic liquid Mg electrolyte and are shown in figures 70 – 73. All EDS

spectra of reduced samples show K-edge signatures of C, Cu, Mn, and Mg and atomic percentages are

reported in table VI. It was found that the largest particles showed weak K-edge signals for Mg. Particles

which had lengths smaller than 200 nm showed strong K-edge signals for Mg. EDS scans of smaller

particles with C show high Mg content. The highest contents led to Mg/Mn ratios well above the

theoretical value, indicating the presence of Mg impurities, likely products of electrolyte decomposition.

Further high-resolution imaging should be completed to ascertain the actual level of Mg intercalation into

the atomic structure of Mn$_2$O$_4$.
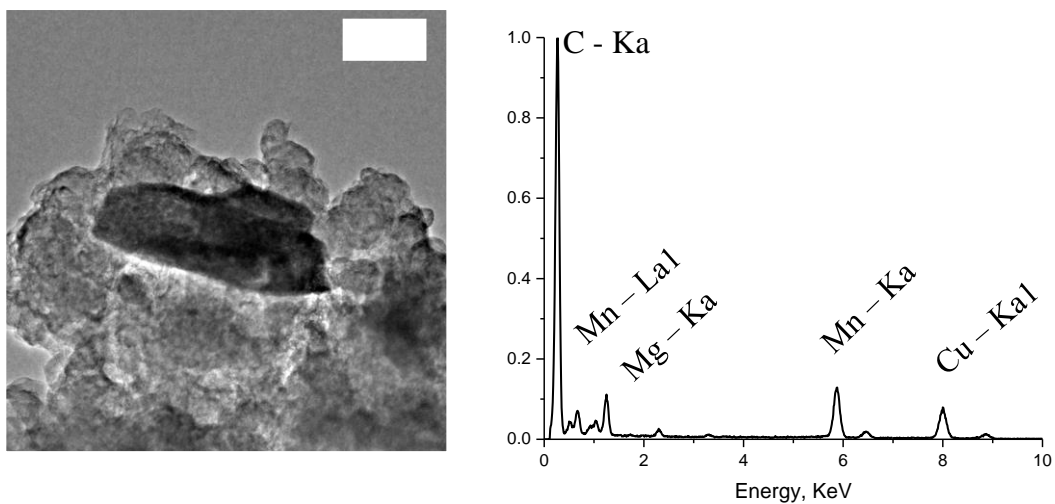
Figure 70. TEM image and EDS spectra of a working electrode composed of oxidized LiMn$_2$O$_4$-iX

following a reduction in Mg ionic liquid electrolyte at 50 $^{\circ}$C. Scale bar is 100 nm.
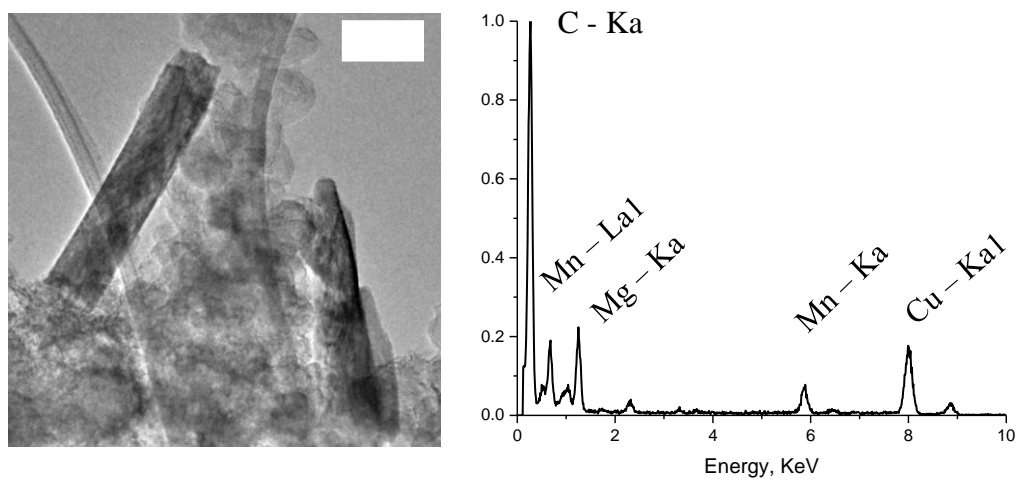
Figure 71. TEM image and EDS spectra of a working electrode composed of oxidized LiMn$_2$O$_4$-iX

following a reduction in Mg ionic liquid electrolyte at 50 °C. Scale bar is 100 nm.
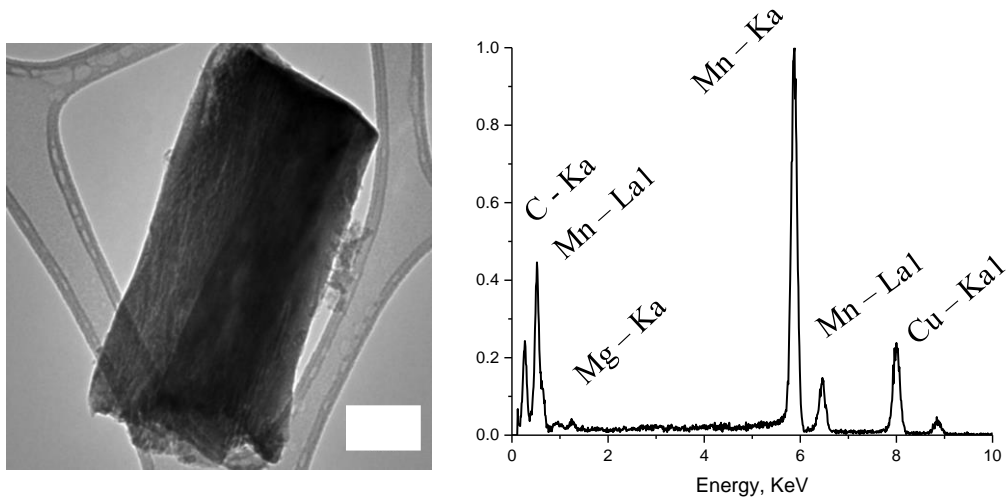
Figure 72. TEM image and EDS spectra of a working electrode composed of oxidized LiMn$_2$O$_4$-iX

following a reduction in Mg ionic liquid electrolyte at 50 ℃. Scale bar is 100 nm.
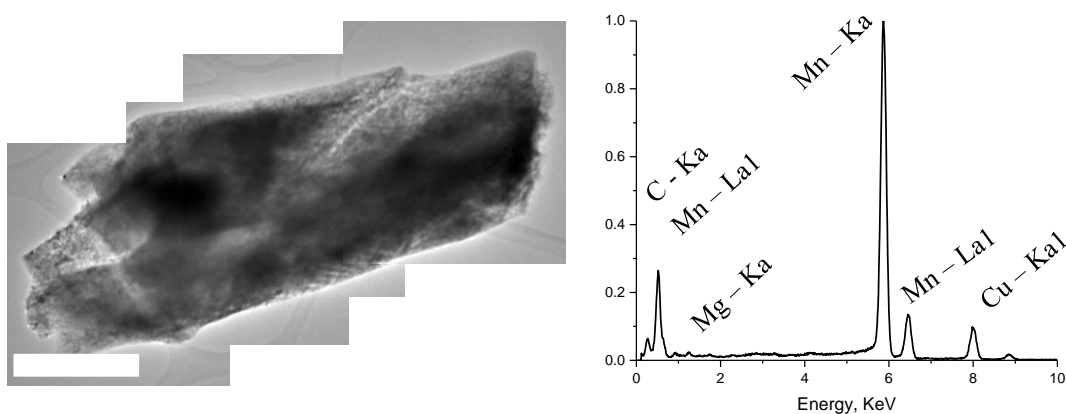
Figure 73. TEM image and EDS spectra of a working electrode composed of oxidized $LiMn_2O_4$-iX following a reduction in Mg ionic liquid electrolyte at 50 °C. Scale bar is 500 nm.

Table VI. Atomic percentages of Mg, Mn and Cu from EDS analyses.

Figure	70	71	72	73
Mg	43	52	3	1
Mn	34	10	77	89
Cu	23	33	20	10
Nominal	$Mg_{2.5}Mn_2O_4$	$Mg_{10}Mn_2O_4$	$Mg_{0.07}Mn_2O_4$	$Mg_{0.03}Mn_2O_4$

X-ray absorption spectroscopy at the Mn $L_{2,3}$-, Mn K- and O K-edges on working electrodes of LiMn$_2$O$_4$-iX electrochemically oxidized in Li-containing electrolyte and then reduced in Mg-containing electrolyte are shown in figures 74 and 75. The Mn $L_{2,3}$-edge spectra in electron yield are shown in figure 74ab, which correspond to the surface of the electrode. The spectra of the oxidized working electrode had L_2 and L_3 features similar energy position with pristine LiMn$_2$O$_4$-iX. There were subtle losses in intensity at 640 eV and increased intensity at 642 eV. The L_2 feature did not shift energy position (654 eV). These spectral changes were less pronounced that after electrochemical oxidation of spinel LiMn$_2$O$_4$ concurrent to partial deintercalation of Li$^+$.[106] This possibly means that the surface of pristine LiMn$_2$O$_4$-iX was already deficient of Li, leading to more Mn^{4+} compared to the bulk. After reduction in Mg ionic liquid electrolyte electrolyte, the L_3 region changed shape to a prominent maximum at 640 eV followed by weaker absorption events until 644 eV. Also, the L_2 event red-shifted to 653 eV. These changes are indicative of Mn reduction. The peak shape is similar to reported MnO; which is purely a Mn^{2+} compound.[94]

Mn K-edge spectra are shown in figure 74c, which correspond to bulk changes. The spectra of the electrochemically cycled working electrodes of LiMn$_2$O$_4$-iX are compared to Mn^{3+} and Mn^{4+} standards. Upon oxidation, the Mn K-edge blue-shifted to higher energy; indicative of the oxidation of Mn and the deintercalation of Li$^+$. The position of the edge was very close to the Mn^{4+} standard. Upon reduction in Mg electrolyte, the Mn K-edge red-shifted beyond the pristine state, indicating substantial reduction, but not past the Mn^{3+} standard. Therefore, there was a substantial difference in the extent of reduction of Mn between surface (rich in Mn^{2+}) and the bulk (average close to Mn^{3+}) of the electrode.

O K-edge spectra are shown in electron (figures 75ab) and fluorescence yields (figures 75cd) of electrochemically cycled LiMn$_2$O$_4$-iX samples. In the pre-edge region, the signatures of pristine LiMn$_2$O$_4$-iX in the electron yield were similar to the fluorescence yield, already discussed above. There was an additional feature at 534 eV, assigned to the presence of Li$_2$CO$_3$ likely from improperly washed Li salts from the ion exchange process. Upon electrochemical oxidation, in electron yield, there was a loss of the feature at 534 eV, which is indicative of decomposition of Li$_2$CO$_3$, yet the other pre-edge features

remained rather constant. On the other hand, in fluorescence, oxidation results in more pronounced relative intensity of the pre-edge peak at 529.5 eV with respect to the second peak at 532.2 eV, as well as an overall increase in intensity of the pre-edge compared to the main absorption edge. This observation would be consistent with oxidation of Mn^{3+} (d^4) to Mn^{4+} (d^3), which would lead to the removal of one electron from Mn 3d-O 2p orbitals, creating new unoccupied states detectable by XAS. These changes were accompanied by a subtle blue-shift of the main edge, which is also consistent with oxidation of the compound. Reduction in Mg electrolyte resulted in a drastic change in the shape of the pre-edge measured from the surface of the electrode (i.e., electron yield) to one maximum at 534 eV. The center of gravity of the main region of absorption red-shifted to 542 eV. These changes are reminiscent of Mn^{+2} reference spectra in the literature.[94] In contrast, when the spectra were measured in fluorescence yield, the O K edge showed a pre-edge event similar in shape to Mn^{3+} standard. The main edge peaks red-shifted by 1 eV after reduction; which is indicative of reduction of Mn. These results are consistent with results from electrochemical, XRD and Mn K-edge analyses, building robust provide proof of the topotatic reduction of Mn in Mg ionic liquid electrolyte.
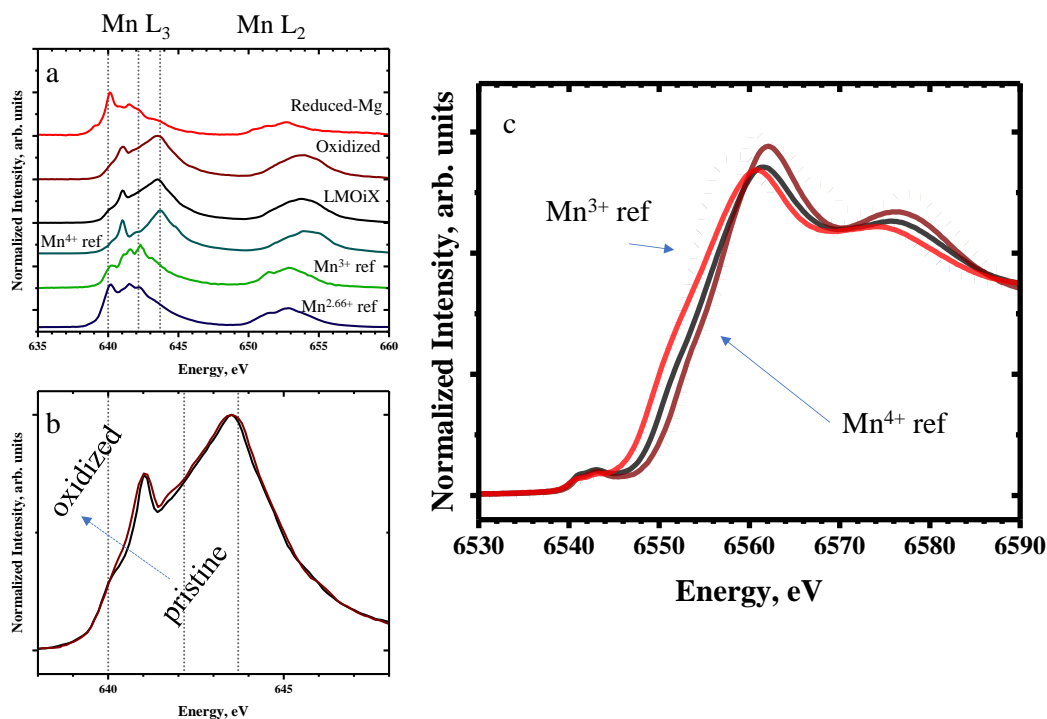
Figure 74. (a) Mn $L_{2,3}$-edge XAS of electrochemically tested $LiMn_2O_4$-iX samples compared to Mn spinel-type standards or (b) or just pristine compared to oxidized, measured with an electron detector. The reference spectra for $Mn^{2.66+}$, Mn^{3+}, and Mn^{4+} are tetragonal spinel Mn_3O_4, tetragonal spinel $MgMn_2O_4$ and delithiated spinel Mn_2O_4, respectively. Dotted lines near 640, 642, and 643.5 eV indicate representative signatures of Mn^{2+}, Mn^{3+}, and Mn^{4+}, respectively. (c) Spectra of pristine samples collected in transmission mode at the Mn K-edge at beamline 10-BM at the Advanced Photon Source at Argonne National Laboratory. The standards of Mn^{3+} and Mn^{4+} are bixbyite Mn_2O_3 and rutile MnO_2. LMOiX corresponds to $CaFe_2O_4$-type $LiMn_2O_4$-iX.
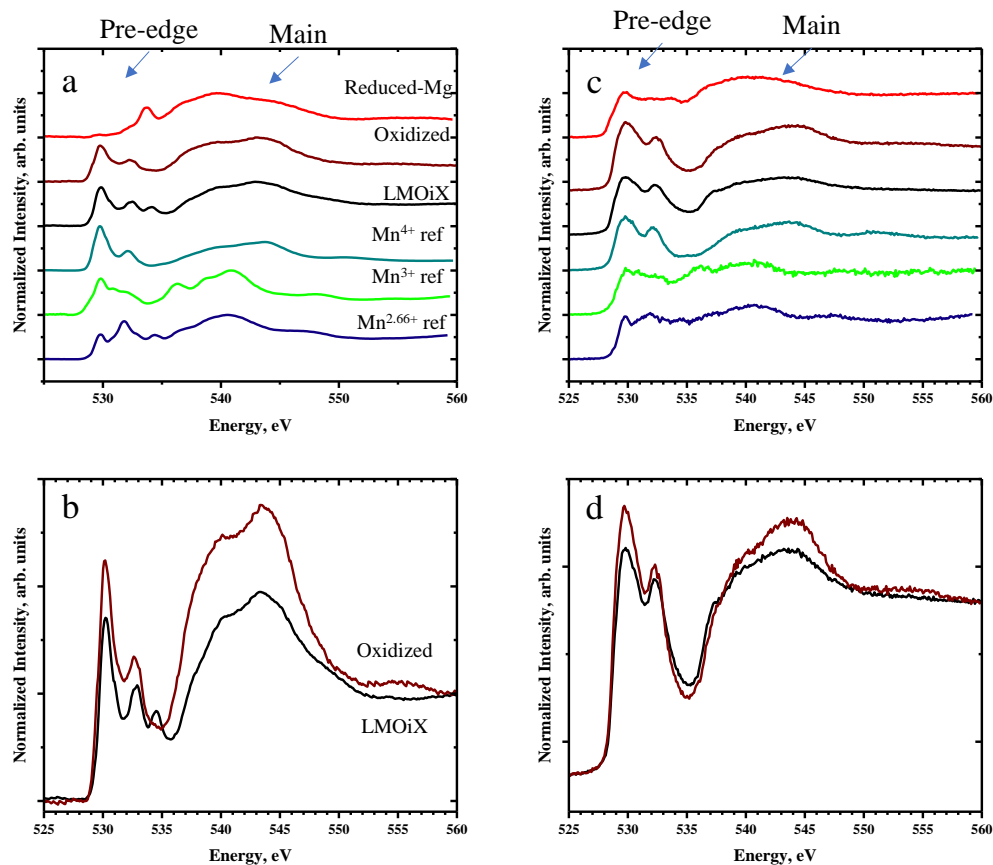
Figure 75. O K-edge XAS of electrochemically tested LiMn$_2$O$_4$-iX samples compared to (a) Mn spinel-type standards or (b) just pristine compared to oxidized, measured with a electron detector. Both (c) and (d) follow the same format as (a) and (b), but a fluorescence detector was used. The reference spectra for Mn$^{2.66+}$, Mn^{3+}, and Mn^{4+} are tetragonal spinel Mn$_3$O$_4$, tetragonal spinel MgMn$_2$O$_4$ and delithiated spinel Mn$_2$O$_4$, respectively.

Working electrodes of oxidized LiMn$_2$O$_4$-iX were also repeatedly cycled at 50 $^\circ$C Mg electrolyte to observe any electrochemical reactivity. The electrochemical curve is shown in figure 76. The initial reduction response (green in figure 76) is comparable to figure 68b where the cell potential dropped quickly to 0 V vs. Mg^{2+}/Mg^0 then plateaued until ~1 mol of Mg was inserted according to the capacity

recorded. Upon oxidation, the potential increased rapidly and started to plateau around 2.5 V vs. Mg^{2+}/Mg^0. The potential of the cell then increased at a slower rate until theoretical capacity was reached. At around the eighth cycle (yellow in figure 76), the limit of potential of oxidation and reduction were reached after only theoretically intercalating ~0.3 Mg in the host structure and the polarization between the two reactions increased. Then, as cycling continued till the 20th cycle (red in figure 76), the polarization between oxidation and reduction reactions reduced. Also, potential plateaus started to emerge at 1.8 V vs. Mg^{2+}/Mg^0 upon reduction and 3.4 V vs. Mg^{2+}/Mg^0 upon oxidation. These voltage plateaus increased in length as cycling continued. Images of the Mg coin cell after long term cycling were taken and shown in figure 65. Following cycling, the carbon cloth counter electrode had dissolved (figure 77a), separator was fused to working electrode (figure 77b), and the working electrode dislodged from the Al foil current collector following washing (figure 77c). This effect was not observed after the first reduction.
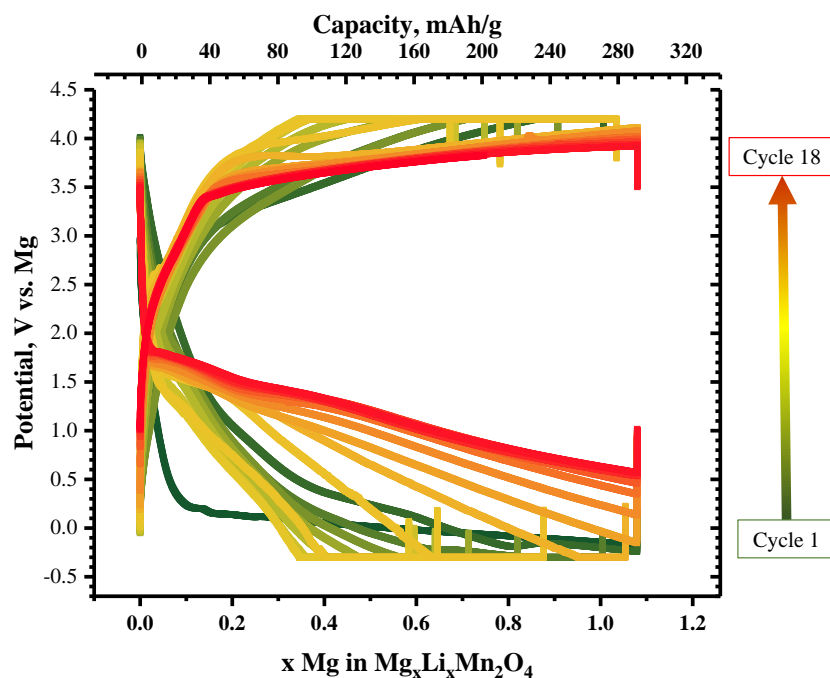
Figure 76. Galvanostatic cyling curve of an oxidized LiMn$_2$O$_4$-iX working electrode cycled at 50 °C at c-rate of C/20 for 18 cycles in Mg electrolyte.

Figure 77. Pictures of the coin cell components after 18 cycles in Mg ionic liquid electrolyte at 50 °C. (a) image of the carbon sludge (b) image of current collector and working electrode and separator pre-washing, and (c) image of separator and working electrode post-washing.

After 20 cycles in Mg electrolyte, the working electrode was characterized using PXRD (figure 78). The full diffraction patterns are shown in figure 78a and zoomed regions are shown 78b and 78c. Comparing diffractograms of reduced once versus 20 times shows a dramatic loss of signal as well as a loss of Bragg reflections. These results suggest that the material was digested during the cycling process; which is to be expected given the surface overreacted in Mn $L_{2,3}$-edge analysis.
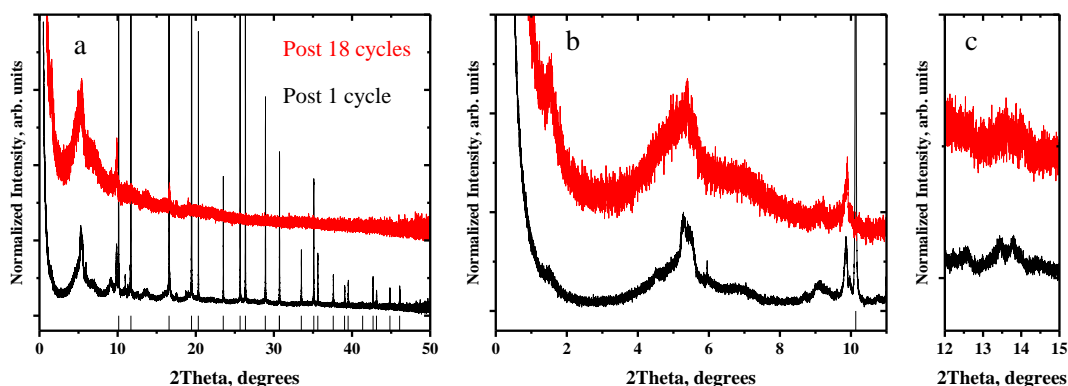
Figure 78. PXRD of working electrode that was discharged once vs cycled for 18 times in Mg ionic liquid electrolyte at 50 °C. Reference peaks at bottom of figure are associated with Bragg reflections of Al foil current collector. (a) is the full spectra, while (b) and (c) are zoomed insets.

6.5 DISCUSSION

Single-step high-pressure synthesis methods were used to prepare black particles of $LiMn_2O_4$ and $NaMn_2O_4$ with $CaFe_2O_4$ crystal structure type. Analysis of structural and spectroscopic characterization

pristine samples showed was evidence of Mn^{2+} on the surface, likely in the form of Mn defects in the Li site observed from Rietveld refinements. It is possible that they accumulate on the surface despite the average concentration in the bulk being low. A mechanism by which such defect accumulation could take place is loss of Li from the particle surface when heated at high temperature. Even though the energy barriers for cation diffusion in $LiMn_2O_4$ are predicted to be low, the electrochemical performance of the as-made powder was poor. Results from electrochemical tests indicate the issue was not related to reaction kinetics or electronic conductivity. In turn, a cation exchange reaction was used to exchange Na^+ with Li^+ in $NaMn_2O_4$ to form defect-free $LiMn_2O_4$ with the $CaFe_2O_4$ crystal structure. Its electrochemical properties were significantly enhanced in this material. Therefore, the poor electrochemistry of $LiMn_2O_4$ made directly in Li form is attributed to surface Mn defects that block one-dimensional ion transport channels and consequently Li^+ diffusion from the electrolyte into the interior of the particles.

Due to its improved kinetics and predicted mobility of Mg^{2+}, the ion exchanged material was used as framework to investigate the intrinsic ability of $CaFe_2O_4$-type Mn_2O_4 to intercalate Mg^{2+} ions. Electrochemical reduction in Mg-based electrolyte was characterized by an expansion of the unit cell and a reduction to Mn^{3+} in the bulk, yet with a loss of crystallinity. Furthermore, the surface of the working electrode was over-reduced, leading to the formation of Mn^{2+}-rich domains. The electrochemical instability of the ionic liquid Mg electrolyte on the surface of the working electrodes at the very low potentials of reaction likely led to a number of unwanted side reactions that lower the coulombic efficiency of the cell. These results suggest that Mg intercalation is possible in the bulk but hampered by slow kinetics of Mg^{2+} intercalation, exacerbated by the formation of ion blocking, over-reduced domains. Furthermore, Mg uptake appears to be heterogenous, with large particles not taking in significant amounts of Mg. As in chapter 5, the full elucidation of the details of this reaction, especially the rate limiting steps, was hampered by the absence of electrolytes that are stable with all cell components and facilitate Mg^{2+} intercalation.

6.6 CONCLUSIONS

In this chapter, the ability of the $CaFe_2O_4$-type Mn_2O_4 structure to conduct electrochemical intercalation of Li^+ and Mg^{2+} ions was characterized. $CaFe_2O_4$-type $LiMn_2O_4$ was prepared via both Na/Li ion exchange from $CaFe_2O_4$-type $NaMn_2O_4$ and direct Li form using high pressure synthesis. Despite have similar structures and nominal stoichiometries, the presence of domains of surface defects with Mn in the Li site blocked cation transfer in the as-prepared $LiMn_2O_4$. These defects were not detected in the Na/Li exchanged product, explaining its drastically improved performance as electrode. Using an ionic liquid Mg-based electrolyte, structural and spectroscopic characterization showed topotactic reduction of the interior of $CaFe_2O_4$-type Mn_2O_4 particles, strongly suggesting the existence of Mg^{2+} intercalation. However, severe heterogeneity was detected, with excessive reduction of the surface of the electrode, and inactivity of the particles at micrometric sizes. These effects are postulated to arise from a combination of slow kinetics of the reaction of Mg^{2+} intercalation and instability of the electrolyte on the surface of the working electrode at the highly cathodic potentials required to reduce the bulk of the compound. For the sake of improving the homogeneity of Mg^{2+} intercalation reactions of $CaFe_2O_4$-type Mn_2O_4, it is again imperative to discover electrolytes with higher cathodic stability as well as more efficient charge transfer kinetics at the oxide interface.

7 CONCLUSIONS

In this work, the ability of working electrodes of manganese oxide, with the spinel or post-spinel crystal structures, to intercalate divalent cations has been assessed using electranalytical, structural and spectroscopic probes. During electrochemical testing of micrometric ordered spinel Mn_2O_4 in aqueous electrolytic environments, reversible intercalation of Mg^{2+} seems more favorable than Ca^{2+} and Zn^{2+}. In electrochemical testing using nonaqueous electrolytes, which are needed to make a functional Mg battery, an ionic liquid Mg electrolyte was chosen because of its high anodic stability. To reduce transport distances in spinel type $MgMn_2O_4$, colloidal methods were used to make nanocrystalline cathode materials. It was determined that ordered $MgMn_2O_4$ nanocrystals with the spinel structure could not be made in a single step, but rather a combination of colloidal and solid-state steps. Colloidal methods were explored to control the synthesis of nanocrystals of MnO, which, after careful mixing in small batches, could then be annealed with $Mg(ac)_2$ to form nanoscale ordered spinel-type $MgMn_2O_4$. Upon electrochemical oxidation, this material showed signs of Mn oxidation from Mn^{3+} to Mn^{4+}, which alludes to Mg^{2+} deintercalation. Despite this reactivity, there was evidence of unwanted side reactions with the ionic liquid Mg electrolyte that inhibited reversible Mg^{2+} intercalation. Lastly, the post-spinel, ordered $CaFe_2O_4$-type Mn_2O_4 framework showed preliminary evidence of reversible intercalation of Mg^{2+} in ionic liquid Mg electrolyte. However, strong intercalation reaction heterogeneity was detected and particle degradation effects are postulated to arise from a combination of slow kinetics of the reaction of Mg^{2+} intercalation and instability of the electrolyte on the surface of the working electrode at the highly cathodic potentials required to reduce the bulk of the compound. This work advances our understanding of the requirements in crystal size and structure with the goal of efficient and reversible intercalation of Mg^{2+} into oxides with high redox potential. Furthermore, for the sake of being able to further elucidate the extent of the reaction, it important to design and develop electrolytes with higher cathodic stability that also facilitate rapid charge transfer kinetics at the oxide interface.

8 CITED LITERATURE

(1) Zumdahl, S. S.; Zumdahl, S. A. *Chemistry, Seventh Edition*.

(2) Tianran, Z.; Daixin, L.; Tao, Z.; Jun, C. Understanding Electrode Materials of Rechargeable Lithium Batteries via DFT Calculations. *Prog. Nat. Sci. Mater. Int.* **2013**, *23* (3), 256–272.

(3) Harris, D. *Quantitative Chemical Analysis*, 7th ed.; W. H. Freman and Company: New York, 2007.

(4) Ponrouch, a.; Frontera, C.; Bardé, F.; Palacín, M. R. Towards a Calcium-Based Rechargeable Battery. *Nat. Mater.* **2015**, *15* (October), 1–5.

(5) Konarov, A.; Voronina, N.; Jo, J. H.; Bakenov, Z.; Sun, Y. K.; Myung, S. T. Present and Future Perspective on Electrode Materials for Rechargeable Zinc-Ion Batteries. *ACS Energy Lett.* **2018**, *3* (10), 2620–2640.

(6) Xing, Z.; Wang, S.; Yu, A.; Chen, Z. Aqueous Intercalation-Type Electrode Materials for Grid-Level Energy Storage: Beyond the Limits of Lithium and Sodium. *Nano Energy* **2018**, *50* (May), 229–244.

(7) Lee, B.; Lee, H. R.; Kim, H.; Chung, K. Y.; Cho, B. W.; Oh, S. H. Elucidating the Intercalation Mechanism of Zinc Ions into α-MnO$_2$ for Rechargeable Zinc Batteries. *Chem. Commun.* **2015**, *51* (45), 9265–9268.

(8) Lee, B.; Yoon, C. S.; Lee, H. R.; Chung, K. Y.; Cho, B. W.; Oh, S. H. Electrochemically-Induced Reversible Transition from the Tunneled to Layered Polymorphs of Manganese Dioxide. *Sci. Rep.* **2014**, *4*, 1–8.

(9) Alfaruqi, M. H.; Mathew, V.; Gim, J.; Kim, S.; Song, J.; Baboo, J. P.; Choi, S. H.; Kim, J. Electrochemically Induced Structural Transformation in a γ-MnO$_2$ Cathode of a High Capacity Zinc-Ion Battery System. *Chem. Mater.* **2015**, *27* (10), 3609–3620.

(10) Gregory, T. D.; Hoffman, R. J.; Winterton, R. C. ChemInform Abstract: Nonaqueous Electrochemistry of Magnesium. Applications to Energy Storage. *ChemInform* **1990**, *21* (22).

(11) Tutusaus, O.; Mohtadi, R. Paving the Way towards Highly Stable and Practical Electrolytes for

Rechargeable Magnesium Batteries. *ChemElectroChem* **2015**, *2* (1), 51–57.

(12)   Ha, S. Y.; Lee, Y. W.; Woo, S. W.; Koo, B.; Kim, J. S.; Cho, J.; Lee, K. T.; Choi, N. S. Magnesium(II) Bis(Trifluoromethane Sulfonyl) Imide-Based Electrolytes with Wide Electrochemical Windows for Rechargeable Magnesium Batteries. *ACS Appl. Mater. Interfaces* **2014**, *6* (6), 4063–4073.

(13)   Orikasa, Y.; Masese, T.; Koyama, Y.; Mori, T.; Hattori, M.; Yamamoto, K.; Okado, T.; Huang, Z. D.; Minato, T.; Tassel, C.; Kim., J., Kobayahi, Y., Abe, T., Kageyama, H., and Uchimoto, Y.. High Energy Density Rechargeable Magnesium Battery Using Earth-Abundant and Non-Toxic Elements. *Sci. Rep.* **2014**, *4*, 1–6.

(14)   Ma, Z.; Kar, M.; Xiao, C.; Forsyth, M.; MacFarlane, D. R. Electrochemical Cycling of Mg in Mg[TFSI]$_2$/Tetraglyme Electrolytes. *Electrochem. commun.* **2017**, *78*, 29–32.

(15)   Muldoon, J.; Bucur, C. B.; Gregory, T. Fervent Hype behind Magnesium Batteries: An Open Call to Synthetic Chemists—Electrolytes and Cathodes Needed. *Angew. Chemie - Int. Ed.* **2017**, *56* (40), 12064–12084.

(16)   Shterenberg, I.; Moshkovich, M.; Gofer, Y.; Levi, E.; Aurbach, D. The Challenge of Developing Rechargeable Magnesium Batteries. *MRS Bull.* **2014**, *39*, 453–460.

(17)   Aurbach, D.; Lu, Z.; Schechter, A.; Gofer, Y.; Gizbar, H.; Turgeman, R.; Cohen, Y.; Moshkovich, M.; Levi, E. Prototype Systems for Rechargeable Magnesium Batteries. *Nature* **2000**, *407* (6805), 724–727.

(18)   Levi, E.; Levi, M. D.; Chasid, O.; Aurbach, D. A Review on the Problems of the Solid State Ions Diffusion in Cathodes for Rechargeable Mg Batteries. *J. Electroceramics* **2009**, *22* (1–3), 13–19.

(19)   Attias, R.; Salama, M.; Hirsch, B.; Goffer, Y.; Aurbach, D. Anode-Electrolyte Interfaces in Secondary Magnesium Batteries. *Joule* **2019**, *3* (1), 27–52.

(20)   Liu, Z.; Lee, J.; Xiang, G.; Glass, H. F. J.; Keyzer, E. N.; Dutton, S. E.; Grey, C. P. Insights into the Electrochemical Performances of Bi Anodes for Mg Ion Batteries Using [25]Mg Solid State NMR Spectroscopy. *Chem. Commun.* **2017**, *53* (4), 743–746.

(21)   Blondeau, L.; Foy, E.; Khodja, H.; Gauthier, M. Unexpected Behavior of the InSb Alloy in Mg-Ion Batteries: Unlocking the Reversibility of Sb. *J. Phys. Chem. C* **2019**, *123* (2), 1120–1126.

(22)   Periyapperuma, K.; Tran, T. T.; Purcell, M. I.; Obrovac, M. N. The Reversible Magnesiation of Pb. *Electrochim. Acta* **2015**, *165*, 162–165.

(23)   Jin, W.; Li, Z.; Wang, Z.; Fu, Y. Q. Mg Ion Dynamics in Anode Materials of Sn and Bi for Mg-Ion Batteries. *Mater. Chem. Phys.* **2016**, *182*, 167–172.

(24)   Wu, N.; Lyu, Y.; Xiao, R.; Yu, X.; Yin, Y.; Yang, X.; Li, H.; Gu, L.; Guo, Y. A Highly Reversible, Low-Strain Mg-Ion Insertion Anode Material for Rechargeable Mg-Ion Batteries. *NPG Asia Mater.* **2014**, *6* (2), 1–7.

(25)   Wang, M.; Jiang, C.; Zhang, S.; Song, X.; Tang, Y.; Cheng, H. M. Reversible Calcium Alloying Enables a Practical Room-Temperature Rechargeable Calcium-Ion Battery with a High Discharge Voltage. *Nat. Chem.* **2018**, *10* (6), 667–672.

(26)   Yao, Z.; Hegde, V. I.; Aspuru-Guzik, A.; Wolverton, C. Discovery of Calcium-Metal Alloy Anodes for Reversible Ca-Ion Batteries. *Adv. Energy Mater.* **2019**, *9* (9), 1–10.

(27)   Balogun, M. S.; Yu, M.; Huang, Y.; Li, C.; Fang, P.; Liu, Y.; Lu, X.; Tong, Y. Binder-Free Fe_2N Nanoparticles on Carbon Textile with High Power Density as Novel Anode for High-Performance Flexible Lithium Ion Batteries. *Nano Energy* **2015**, *11*, 348–355.

(28)   Balogun, M. S.; Yu, M.; Li, C.; Zhai, T.; Liu, Y.; Lu, X.; Tong, Y. Facile Synthesis of Titanium Nitride Nanowires on Carbon Fabric for Flexible and High-Rate Lithium Ion Batteries. *J. Mater. Chem. A* **2014**, *2* (28), 10825–10829.

(29)   Whittingham, M. S. Lithium Batteries and Cathode Materials. *Chem. Rev.* **2004**, *104* (10), 4271–4301.

(30)   Armand, M.; Tarascon, J.-M. Building Better Batteries. *Nature* **2008**, *451* (7179), 652–657.

(31)   Shiga, T.; Hase, Y.; Kato, Y.; Inoue, M.; Takechi, K. A Rechargeable Non-Aqueous $Mg–O_2$ Battery. *Chem. Commun.* **2013**, *49* (80), 9152.

(32)   Pan, B.; Zhou, D.; Huang, J.; Zhang, L.; Burrell, A. K.; Vaughey, J. T.; Zhang, Z.; Liao, C. 2,5-

Dimethoxy-1,4-Benzoquinone (DMBQ) as Organic Cathode for Rechargeable Magnesium-Ion Batteries. *J. Electrochem. Soc.* **2016**, *163* (3), A580–A583.

(33) Kim, D. M.; Kim, Y.; Arumugam, D.; Woo, S. W.; Jo, Y. N.; Park, M. S.; Kim, Y. J.; Choi, N. S.; Lee, K. T. Co-Intercalation of Mg^{2+} and Na^+ in $Na_{0.69}Fe_2(CN)_6$ as a High-Voltage Cathode for Magnesium Batteries. *ACS Appl. Mater. Interfaces* **2016**, *8* (13), 8554–8560.

(34) Liu, M.; Jain, A.; Rong, Z.; Qu, X.; Canepa, P.; Malik, R.; Ceder, G.; Persson, K. A. Evaluation of Sulfur Spinel Compounds for Multivalent Battery Cathode Applications. *Energy Environ. Sci.* **2016**, *9* (10), 3201–3209.

(35) Sun, X.; Bonnick, P.; Duffort, V.; Liu, M.; Rong, Z.; Persson, K. A.; Ceder, G.; Nazar, L. F. A High Capacity Thiospinel Cathode for Mg Batteries. *Energy Environ. Sci.* **2016**, *195*, 6902–6904.

(36) Zhou, B.; Shi, H.; Cao, R.; Zhang, X.; Jiang, Z. Theoretical Study on the Initial Stage of a Magnesium Battery Based on a V_2O_5 Cathode. *Phys. Chem. Chem. Phys.* **2014**, *16* (34), 18578–18585.

(37) Yoo, H. D.; Jokisaari, J. R.; Yu, Y.-S.; Kwon, B. J.; Hu, L.; Kim, S.; Han, S.-D.; Lopez, M.; Lapidus, S. H.; Nolis, G. M.; Ingram, B., Bolotin, I., Ahmed, S., Klie, R., Vaughey, J., Fister, T., and Cabana, J. Intercalation of Magnesium into a Layered Vanadium Oxide with High Capacity. *ACS Energy Lett.* **2019**, acsenergylett.9b00788.

(38) Verrelli, R.; Black, A. P.; Pattanathummasid, C.; Tchitchekova, D. S.; Ponrouch, A.; Oró-Solé, J.; Frontera, C.; Bardé, F.; Rozier, P.; Palacín, M. R. On the Strange Case of Divalent Ions Intercalation in V_2O_5. *J. Power Sources* **2018**, *407* (July), 162–172.

(39) Nuli, Y.; Yang, J.; Li, Y.; Wang, J. Mesoporous Magnesium Manganese Silicate as Cathode Materials for Rechargeable Magnesium Batteries. *Chem. Commun.* **2010**, *46* (21), 3794–3796.

(40) Liu, M.; Rong, Z.; Malik, R.; Canepa, P.; Jain, A.; Ceder, G.; Persson, K. A.; Liu, M. Spinel Compounds as Multivalent Battery Cathodes: A Systematic Evaluation Based on Ab Initio Calculations. *Energy Environ. Sci* **2015**, *8* (3), 964–974.

(41) Ling, C.; Mizuno, F. Phase Stability of Post-Spinel Compound AMn_2O_4 (A = Li, Na, or Mg) and

Its Application as a Rechargeable Battery Cathode. *Chem. Mater.* **2013**, *25* (15), 3062–3071.

(42) Crank, J. *The Mathematics of Diffusion*; Clarendon Press: Oxford, 1956.

(43) Broussely, M.; Biensan, P.; Simon, B. Lithium Insertion into Host Materials: The Key to Success for Li Ion Batteries. *Electrochim. Acta* **1999**, *45* (1), 3–22.

(44) Winter, M.; Besenhard, J.; Spahr, M.; Novak, P. Insertion Electrode for Rechargeable Lithium Batteries. *Adv. Mater.* **1998**, *10* (10), 725.

(45) Sebastian, L.; Gopalakrishnan, J. Lithium Ion Mobility in Metal Oxides: A Materials Chemistry Perspective. *J. Mater. Chem.* **2003**, *13* (3), 433–441.

(46) Erickson, E. M.; Markevich, E.; Salitra, G.; Sharon, D.; Hirshberg, D.; de la Llave, E.; Shterenberg, I.; Rosenman, A.; Frimer, A.; Aurbach, D. Publisher's Note: Review—Development of Advanced Rechargeable Batteries: A Continuous Challenge in the Choice of Suitable Electrolyte Solutions [*J. Electrochem. Soc.,* 162, A2424 (2015)]. *J. Electrochem. Soc.* **2017**, *164* (4), X5–X5.

(47) Kim, C.; Phillips, P. J.; Key, B.; Yi, T.; Nordlund, D.; Yu, Y. S.; Bayliss, R. D.; Han, S. D.; He, M.; Zhang, Z.; Burrell, A., Klie, R., and Cabana, J. Direct Observation of Reversible Magnesium Ion Intercalation into a Spinel Oxide Host. *Adv. Mater.* **2015**, *27* (22), 3377–3384.

(48) Brito, M.; Clottes, J.; Aujoulat, N.; Coye, N. The Cave Art Paintings of the Lascaux Cave http://www.bradshawfoundation.com/lascaux/.

(49) Niederberger, M.; Pinna, N. *Metal Oxide Nanoparticles in Organic Solvents*; 2009.

(50) Shen, P. C.; Lin, Y.; Wang, H.; Park, J. H.; Leong, W. S.; Lu, A. Y.; Palacios, T.; Kong, J. CVD Technology for 2-D Materials. *IEEE Trans. Electron Devices* **2018**, *65* (10), 4040–4052.

(51) Liu, M.; Rong, Z.; Malik, R.; Canepa, P.; Jain, A.; Ceder, G.; Persson, K. A.; Liu, M. Spinel Compounds as Multivalent Battery Cathodes: A Systematic Evaluation Based on Ab Initio Calculations. *Energy Environ. Sci* **2015**, *8* (3), 964–974.

(52) Kim, C.; Adil, A. A.; Bayliss, R. D.; Kinnibrugh, T. L.; Lapidus, S. H.; Nolis, G. M.; Freeland, J. W.; Phillips, P. J.; Yi, T.; Yoo, H. D.; Kwon, B., Yu, Young-Sang, Y., Klie, R., Chupas, P.,

Chapman, K., and Cabana, J. Multivalent Electrochemistry of Spinel $Mg_xMn_{3-x}O_4$ Nanocrystals. *Chem. Mater.* **2018**, *30* (5), 1496–1504.

(53)   Aujoulat, N. *Lascaux: Movement, Space and Time*, 1st ed.; H. N. Abrams: New York, 2005.

(54)   Niederberger, M.; Pinna, N. *Metal Oxide Nanoparticles in Organic Solvents*; Springer: London, United Kingdom, 2009.

(55)   Kuno, M. *Introductory Nanoscience Physical and Chemical Concepts*, 1st ed.; Taylor and Francis Group: New York, 2012.

(56)   Yamaura, K.; Huang, Q.; Zhang, L.; Takada, K.; Baba, Y.; Nagai, T.; Matsui, Y.; Kosuda, K.; Takayama-Muromachi, E. Spinel-to-$CaFe_2O_4$-Type Structural Transformation in $LiMn_2O_4$ under High Pressure. *J. Am. Chem. Soc.* **2006**, *128* (29), 9448–9456.

(57)   Bard, A. J.; Faulkner, L. R. *Electrochemical Methods : Fundamentals and Applications*; 2001.

(58)   Skoog, D.; Holler, J.; Crouch, C. *Principles of Instrumental Analysis*, 6th ed.; Cengage: New York, 2006.

(59)   Wolfman, M. GSAS-II Introduction - Basic Profile Refinement https://magicacid.com/blog/basic-refinement/ (accessed Feb 7, 2019).

(60)   Road, M. Pawley; J. Appl. Cryst, 1981, 14, 357-361.Pdf. **1981**, 357–361.

(61)   Murphy, C. J.; Buriak, J. M. Best Practices for the Reporting of Colloidal Inorganic Nanomaterials. *Chem. Mater.* **2015**, *27* (14), 4911–4913.

(62)   Egerton, R. F. *Physical Principles of Electron Microscopy*; 2005.

(63)   de Groot, F.; Kotani, A. *Core Level Spectroscopy of Solids*; Taylor and Francis Group: Boca Raton, FL, USA, 2008.

(64)   Jahrman, E. P.; Holden, W. M.; Ditter, A. S.; Mortensen, D. R.; Seidler, G. T.; Fister, T. T.; Kozimor, S. A.; Piper, L. F. J.; Rana, J.; Hyatt, N. C.; and Stennett, M. An Improved Laboratory-Based x-Ray Absorption Fine Structure and x-Ray Emission Spectrometer for Analytical Applications in Materials Chemistry Research. *Rev. Sci. Instrum.* **2019**, *90* (2).

(65)   Seidler, G. T.; Mortensen, D. R.; Remesnik, A. J.; Pacold, J. I.; Ball, N. A.; Barry, N.; Styczinski,

M.; Hoidn, O. R. A Laboratory-Based Hard x-Ray Monochromator for High-Resolution x-Ray Emission Spectroscopy and x-Ray Absorption near Edge Structure Measurements. *Rev. Sci. Instrum.* **2014**, *85* (11).

(66) Mortensen, D. R.; Seidler, G. T.; Ditter, A. S.; Glatzel, P. Benchtop Nonresonant X-Ray Emission Spectroscopy: Coming Soon to Laboratories and XAS Beamlines Near You? *J. Phys. Conf. Ser.* **2016**, *712* (1).

(67) Ravel, B.; Newville, M. ATHENA, ARTEMIS, HEPHAESTUS: Data Analysis for X-Ray Absorption Spectroscopy Using IFEFFIT. *J. Synchrotron Radiat.* **2005**, *12* (4), 537–541.

(68) Brown, M. *Introduction to Thermal Analysis: Techniques and Applications*; Chapman and Hill: London, 1988.

(69) Shannon, R. Revised Effective Ionic Radii and Systematic Studies of Interatomic Distances in Halides and Chalcogenides. *Acta Crystallogr.* **1976**, *A32*, 751–767.

(70) Burda, C.; Chen, X.; Narayanan, R.; El-Sayed, M. A. Chemistry and Properties of Nanocrystals of Different Shapes. *Chem. Rev.* **2005**, *105* (4), 1025–1102.

(71) Liu, X.; Chen, C.; Zhao, Y.; Jia, B. A Review on the Synthesis of Manganese Oxide Nanomaterials and Their Applications on Lithium-Ion Batteries. *J. Nanomater.* **2013**, *2013*.

(72) Xing, R.; Liu, G.; Quan, Q.; Bhirde, A.; Zhang, G.; Jin, A.; Bryant, L. H.; Zhang, A.; Liang, A.; Eden, H. S.; Hou, Y., and Chen, X. Functional MnO Nanoclusters for Efficient SiRNA Delivery. *Chem. Commun.* **2011**, *47* (44), 12152–12154.

(73) Kwon, B. J.; Phillips, P. J.; Key, B.; Dogan, F.; Freeland, J. W.; Kim, C.; Klie, R. F.; Cabana, J. Nanocrystal Heterostructures of $LiCoO_2$ with Conformal Passivating Shells. *Nanoscale* **2018**, *10* (15), 6954–6961.

(74) Sun, Y.; Liu, N.; Cui, Y. Promises and Challenges of Nanomaterials for Lithium-Based Rechargeable Batteries. *Nat. Energy* **2016**, *1* (7), 1–12.

(75) Leite, E. R.; Ribeiro, C. *Crystallization and Growth of Colloidal Nanocrystals*; Springer: London, United Kingdom, 2012.

(76)   Yin, M.; O'Brien, S. Synthesis of Monodisperse Nanocrystals of Manganese Oxides. *J. Am. Chem. Soc.* **2003**, *125* (34), 10180–10181.

(77)   Jiao, F.; Harrison, A.; Bruce, P. G. Ordered Three-Dimensional Arrays of Monodispersed Mn_3O_4 Nanoparticles with a Core-Shell Structure and Spin-Glass Behavior. *Angew. Chemie - Int. Ed.* **2007**, *46* (21), 3946–3950.

(78)   Seo, W. S.; Jo, H. H.; Lee, K.; Kim, B.; Oh, S. J.; Park, J. T. Size-Dependent Magnetic Properties of Colloidal Mn_3O_4 and MnO Nanoparticles. *Angew. Chemie - Int. Ed.* **2004**, *43* (9), 1115–1117.

(79)   Zhang, H.; Jing, L.; Zeng, J.; Hou, Y.; Li, Z.; Gao, M. Revisiting the Coordination Chemistry for Preparing Manganese Oxide Nanocrystals in the Presence of Oleylamine and Oleic Acid. *Nanoscale* **2014**, *6* (11), 5918–5925.

(80)   Sun, X.; Zhang, Y. W.; Si, R.; Yan, C. H. Metal (Mn, Co, and Cu) Oxide Nanocrystals from Simple Formate Precursors. *Small* **2005**, *1* (11), 1081–1086.

(81)   Ould-Ely, T.; Prieto-Centurion, D.; Kumar, A.; Guo, W.; Knowles, W. V.; Asokan, S.; Wong, M. S.; Rusakova, I.; Lüttge, A.; Whitmire, K. H. Manganese(II) Oxide Nanohexapods: Insight into Controlling the Form of Nanocrystals. *Chem. Mater.* **2006**, *18* (7), 1821–1829.

(82)   Xie, S.; Zhou, X.; Han, X.; Kuang, Q.; Jin, M.; Jiang, Y.; Xie, Z.; Zheng, L. Supercrystals from Crystallization of Octahedral MnO Nanocrystals. *J. Phys. Chem. C* **2009**, *113* (44), 19107–19111.

(83)   Hyeon, T.; Su Seong Lee; Park, J.; Chung, Y.; Hyon Bin Na. Synthesis of Highly Crystalline and Monodisperse Maghemite Nanocrystallites without a Size-Selection Process. *J. Am. Chem. Soc.* **2001**, *123* (51), 12798–12801.

(84)   Mourdikoudis, S.; Liz-Marzán, L. M. Oleylamine in Nanoparticle Synthesis. *Chem. Mater.* **2013**, *25* (9), 1465–1476.

(85)   Siddiqi, M. A.; Siddiqui, R. A.; Atakan, B. Thermal Stability, Sublimation Pressures and Diffusion Coefficients of Some Metal Acetylacetonates. *Surf. Coatings Technol.* **2007**, *201* (22-23 SPEC. ISS.), 9055–9059.

(86)   Seo, W. S.; Shim, J. H.; Oh, S. J.; Lee, E. K.; Hur, N. H.; Park, J. T. Phase- and Size-Controlled

Synthesis of Hexagonal and Cubic CoO Nanocrystals. *J. Am. Chem. Soc.* **2005**, *127* (17), 6188–6189.

(87)   Hou, Y.; Xu, Z.; Sun, S. Controlled Synthesis and Chemical Conversions of FeO Nanoparticles. *Angew. Chemie - Int. Ed.* **2007**, *46* (33), 6329–6332.

(88)   Malavasi, L.; Tealdi, C.; Flor, G.; Amboage, M. High-Pressure Stability of the Tetragonal Spinel $MgMn_2O_4$: Role of Inversion. **2005**, 1–9.

(89)   Yin, J.; Brady, A. B.; Takeuchi, E. S.; Marschilok, A. C.; Takeuchi, K. J. Magnesium-Ion Battery-Relevant Electrochemistry of $MgMn_2O_4$: Crystallite Size Effects and the Notable Role of Electrolyte Water Content. *Chem. Commun.* **2017**, *53* (26), 3665–3668.

(90)   Nolis, G. M.; Bolotnikov, J. M.; Cabana, J. Control of Size and Composition of Colloidal Nanocrystals of Manganese Oxide. *Inorg. Chem.* **2018**, *57* (20), 12900–12907.

(91)   Patnaik, P.; York, N.; San, C.; Lisbon, F.; Madrid, L.; City, M.; New, M.; San, D.; Singapore, J. S.; Toronto, S. *Handbook of Inorganic Chemicals McGraw-Hill Library of Congress Cataloging-in-Publication Data*; 2003.

(92)   Kwon, B. J.; Dogan, F.; Jokisaari, J. R.; Key, B.; Kim, C.; Liu, Y. S.; Guo, J.; Klie, R. F.; Cabana, J. Effect of Passivating Shells on the Chemistry and Electrode Properties of $LiMn_2O_4$ Nanocrystal Heterostructures. *ACS Appl. Mater. Interfaces* **2019**, *11* (4), 3823–3833.

(93)   Miyai, Y.; Ooi, K.; Katoh, S. Preparation and Ion-Exchange Properties of Ion-Sieve Manganese Oxide Based on Mg_2MnO_4. *J. Colloid Interface Sci.* **1989**, *130* (2), 535–541.

(94)   Qiao, R.; Chin, T.; Harris, S. J.; Yan, S.; Yang, W. Spectroscopic Fingerprints of Valence and Spin States in Manganese Oxides and Fluorides. *Curr. Appl. Phys.* **2013**, *13* (3), 544–548.

(95)   Zhao, H.; Liu, L.; Xiao, L.; Hu, Z.; Han, S.; Liu, Y.; Chen, D.; Liu, X. The Effects of Co Doping on the Crystal Structure and Electrochemical Performance of $Mg(Mn_{2-x}Co_x)O_4$ Negative Materials for Lithium Ion Battery. *Solid State Sci.* **2015**, *39*, 23–28.

(96)   Tang, D.; Sun, Y.; Yang, Z.; Ben, L.; Gu, L.; Huang, X. Surface Structure Evolution of $LiMn_2O_4$ Cathode Material upon Charge/Discharge. *Chem. Mater.* **2014**, *26* (11), 3535–3543.

(97)   Nolis, G. M.; Adil, A.; Yoo, H. D.; Hu, L.; Bayliss, R. D.; Lapidus, S. H.; Berkland, L.; Phillips, P. J.; Freeland, J. W.; Kim, C.; Klie, R., and Cabana, J. Electrochemical Reduction of a Spinel-Type Manganese Oxide Cathode in Aqueous Electrolytes with Ca^{2+} or Zn^{2+}. *J. Phys. Chem. C* **2018**, *122* (8), 4182–4188.

(98)   Irifune, T.; Fujino, K.; Ohtani, E. A New High-Pressure Form of $MgAl_2O_4$. *Nature* **1991**, *349* (1), 409–411.

(99)   Mamiya, M.; Tokiwa, K.; Akimoto, J. Soft Chemical Synthesis and Electrochemical Properties of Calcium Ferrite-Type $Li_xMn_2O_4$. *J. Power Sources* **2016**, *244*, 382–388.

(100) Liu, X.; Wang, X.; Iyo, A.; Yu, H.; Li, D.; Zhou, H. High Stable Post-Spinel $NaMn_2O_4$ Cathode of Sodium Ion Battery. *J. Mater. Chem. A* **2014**, *2* (36), 14822–14826.

(101) Tokiwa, K.; Matsukura, K.; Kasahara, S.; Tsuda, S.; Mikusu, S.; Takeuchi, K.; Iyo, A.; Tanaka, Y.; Akimoto, J.; Awaka, J.; Kijima, N., Takahashi, Y., and Watanabe, T. High Pressure Synthesis and Magnetic Properties of $CaFe_2O_4$ -Type $NaMn_2O_4$ and $LiMn_2O_4$. *J. Phys. Conf. Ser.* **2009**, *150* (4), 042210.

(102) Akimoto, J.; Awaka, J.; Kijima, N.; Takahashi, Y.; Maruta, Y.; Tokiwa, K.; Watanabe, T. High-Pressure Synthesis and Crystal Structure Analysis of $NaMn_2O_4$ with the Calcium Ferrite-Type Structure. *J. Solid State Chem.* **2006**, *179* (1), 169–174.

(103) Hirai, S.; Santos, A. M. Dos; Shapiro, M. C.; Molaison, J. J.; Pradhan, N.; Guthrie, M.; Tulk, C. a.; Fisher, I. R.; Mao, W. L. Giant Atomic Displacement Induced by Built-in Strain in Metastable Mn_3O_4. **2012**, 4–8.

(104) Qiao, R.; Chin, T.; Harris, S. J.; Yan, S.; Yang, W. Spectroscopic Fingerprints of Valence and Spin States in Manganese Oxides and Fluorides. **2013**, *13*, 544–548.

(105) Cockayne, E.; Levin, I.; Wu, H.; Llobet, A. Magnetic Structure of Bixbyite α-Mn_2O_3: A Combined DFT+U and Neutron Diffraction Study. *Phys. Rev. B - Condens. Matter Mater. Phys.* **2013**, *87* (18), 1–11.

(106) Yamanaka, K.; Nakanishi, K.; Watanabe, I.; OHTA, T. *Operando* Soft X-Ray Absorption

Spectroscopic Study of an All-Solid-State Lithium-Ion Battery Using a NASICON-Type Lithium Conductive Glass Ceramic Sheet. *Electrochemistry* **2018**, *86* (3), 128–133.

EDUCATION

Doctor of Philosophy in Chemistry

> University of Illinois at Chicago
> Chicago, Illinois
> July 2019
> Advisor: Professor Jordi Cabana
> Thesis title: Understanding divalent cation intercalation in manganese oxides

Master's in Science of Chemical Engineering and Materials Science

> Université de Picardie Jules Verne
> Amiens, France
> September 2014
> Advisors: Professors Marek Marcinek and Władysław Wieczorek
> Thesis title: New polymer electrolytes for sodium-ion batteries
> Thesis project completed at Warsaw University of Technology
> Warsaw, Poland

Bachelor's in Science of Chemistry, concentration in Materials Science

> Binghamton University
> Binghamton, New York
> May 2012

Research Experience

Research Assistant

> University of Illinois at Chicago
> 2015 – present

Research Assistant

> Warsaw University of Technology
> 2014 (6 months)

Research Assistant

> Binghamton University
> 2010 – 2012
> Advisor: Professor M. Stanley Whittingham

Research Assistant

    Lawrence Berkeley National Laboratory
    Berkeley, California
    2011 (2 months)
    Advisor: Professor Jordi Cabana

Teaching Experience

Teaching Assistant

    Binghamton University
    2010 (6 months)

Professional Experience

Program Representative

    Early Career Network
    Joint Center for Chemical Energy Storage Research
    Argonne National Laboratory
    Argonne, Illinois
    Advisor: Professor George Crabtree
    2017 – 2018

Co-founder and member

    Association for Student And Postdocs
    Joint Center for Chemical Energy Storage Research
    2018 – present

Co-organizer of international conference

    Lithium Sulfur Batteries: Mechanisms, Modeling, and Materials
    Joint Center for Chemical Energy Storage Research
    Chicago, Illinois
    Organizing Committee: George Crabtree, Bradley Ullrich, Lee Zachos, Sue Marconi, Kristen
        Manke, and Ben Schiltz
    2018

Chemical Hygiene Officer

    University of Illinois at Chicago
    Advisor: Professor Jordi Cabana
    2015 – 2017

Board Member

       Committee on Gender, Discrimination and Inclusion
       Erasmus Mundus Student and Alumni Association
       Warsaw, Poland and Chicago, Illinois
       2014 – 2016

President

       Lesbian, Gay, Bisexual and Transgender (LGBT) Network
       Erasmus Mundus Student and Alumni Association
       Warsaw, Poland and Chicago, Illinois
       2014 – 2016
       Member since 2013

Program Representative

       Materials for Energy Storage and Conversion, Master's program
       Erasmus Mundus Student and Alumni Association
       Warsaw, Poland and Cordoba, Spain
       2013 – 2014

Editor

       Frontiers in Energy Newsletter
       United States of America Department of Energy
       Editor-in-chief: Kristen Manke
       2011 – 2012

Materials Analyst Intern

       Northeast Organic Farming Association
       Supervisor: Sherrie Hastings
       Binghamton, New York
       2009 - 2011

Publications

Intercalation of Magnesium into a Layered Vanadium Oxide with High Capacity. H. D. Yoo, J. R.

Jokisaari, Y.-S. Yu, B. J. Kwon, L. Hu, S. Kim, S.-D. Han, M. Lopez, S. H. Lapidus, **G. M.**

Nolis, B. J. Ingram, I. Bolotin, S. Ahmed, R. F. Klie, J. T. Vaughey, T. T. Fister, J. Cabana. *ACS*

Energy Lett., 2019. DOI: 10.1021/acsenergylett.9b00788

Tailoring the Electrochemical Activity of Magnesium Chromium Oxide Towards Mg Batteries Through

Control of Size and Crystal Structure. L. Hu, I. D. Johnson, S. Kim, **G. M. Nolis,** J. Freeland, H.

D. Yoo, T. T. Fister, L. McCafferty, T. E. Ashton, J. A. Darr, and J. Cabana. *Nanoscale*, 2018.

DOI: 10.1039/C8NR08347A

Control of Size and Composition of Colloidal Nanocrystals of Manganese Oxide. **G. M. Nolis,** J. M.

Bolotnikov, and J. Cabana. *Inorganic Chemistry*, 2018. DOI: 10.1021/acs.inorgchem.8b02124

Multivalent electrochemistry of spinel $Mg_xMn_{3-x}O_4$ nanocrystals. C. Kim, A. A. Adil, R. D. Bayliss, T. L.

Kinnibrugh, S. H. Lapidus, **G. M. Nolis**, J. W. Freeland, P. J. Phillips, T. Yi, H. D. Yoo, B. J.

Kwon, Y.-S. Yu, R. Klie, P. J. Chupas, K. W. Chapman, and J. Cabana. *Chemistry of Materials*.

2018, DOI: 10.1021/acs.chemmater.7b03640

Electrochemical reduction of a spinel-type manganese oxide cathode in aqueous electrolytes with Ca^{2+} or

Zn^{2+}. **G. M. Nolis,** A. Adil, H. Deog Yoo, L. Hu, R. D. Bayliss, S. H. Lapidus, L. Berkland, P. J.

Phillips, J. W. Freeland, C. Kim, R. F. Klie and J. Cabana. *Journal of Physical Chemistry C,*

2018, DOI: 10.1021/acs.jpcc.7b12084

$NaV_{1.25}Ti_{0.75}O_4$: A potential post-spinel cathode material for Mg batteries. X. Sun, L. Blanc, **G. M. Nolis,**

P. Bonnick, J. Cabana and L. F. Nazar. *Chemistry of Materials*. 2018, 30,

DOI:10.1021/acs.chemmater.7b03383

Degradation mechanisms of magnesium metal anodes in electrolytes based on $(CF_3SO_2)_2N^-$ at high

current densities. H. D. Yoo, S. D. Han, I. Bolotin, **G. M. Nolis,** R. D. Bayliss, A. K. Burrell, J.

T. Vaughey, and J. Cabana. *Langmuir*, 2017, DOI:10.1021/acs.langmuir.7b01051

Fluorine-free electrolytes for all-solid sodium-ion batteries based on percyano-substituted organic salts.

A. Bitner-Michalska, **G. M. Nolis,** G. Żukowska, A. Zalewska, M. Poterała, T. Trzeciak, M.

Dranka, M. Kalita, P. Jankowski, L. Niedzicki, J. Zachara, M. Marcinek, and W. Wieczorek.

Nature Scientific Reports, 2016. DOI:10.1038/srep40036

Surface chemistry consequences of Mg-based coatings on $LiNi_{0.5}Mn_{1.5}O_4$ electrode materials upon

operation at high voltage. G. Alva, C. Kim, T. Yi, J. Cook, L. Xu, **G. M. Nolis,** and J. Cabana.

Journal of Physical Chemistry C, 2014. DOI: 10.1021/jp5003148

Structure, defects and thermal stability of delithiated olivine phosphates. **G. M. Nolis,** F. Omenya, R.

Zhang, B. Fang, S. Upreti, N. A. Chernova, F. Wang, J. Graetz, Y. Hu, C. P. Grey, and M. S.

Whittingham. *Journal of Materials Chemistry,* 2012. DOI:10.1039/c2jm33183g

Structure and stability of olivine phase $FePO_4$. **G. M. Nolis,** S. Upreti, N. A. Chernova, and M. S.

Whittingham. *Materials Research Society Proceedings,* 2011. DOI:10.1557/opl.2011.1339

What can we learn about battery materials from their magnetic properties? N. A. Chernova, **G. M. Nolis,**

F. Omenya, H. Zhou, L. Zheng, and M. S. Whittingham. *Journal of Materials Chemistry*, 2011.

DOI: 10.1039/C1JM00024A

Intellectual Property

"Electrolyte for Metal-ion Batteries," Publication number: WO/2016/203390, International Application

Number: PCT/IB2016/053531. December 2016, Warsaw, Poland

General Articles

G. M. Nolis, "Crossing paths conference in Bologna, Italy," *Field Reporter, Erasmus Mundus Student*

and Alumni Association, July, 2014

G. M. Nolis, "Crossing paths intersectionality conference, day 1," *International Lesbian, Gay, Bisexual,*

Transgender and Queer Youth and Student Organisation, July, 2014

G. M. Nolis, "An interview with Irene Beyerlein," *DOE EFRC Newsletter,* July, 2012

G. M. Nolis, "Three-dimensional modeling takes on solar device challenges," *DOE EFRC Newsletter,*

September 2011

G. M. Nolis, "Batteries go viral," *DOE EFRC Newsletter,* May 2011

Oral Presentations

G. M. Nolis, "Understanding divalent cation intercalation in manganese oxides with the spinel structure." Argonne National Laboratory Visiting Researcher seminer, 2019, Argonne, Illinois.

G. M. Nolis, J. Bolotnikov and J. Cabana. "Colloidal Mn-O phase space as a function of temperature and oxidizing agent." 256th American Chemical Society Meeting, 2018, Boston, Massachusetts

A. Bitner-Michalska, **G. M. Nolis,** T. Trzeciak, Z. Żukowska, L. Niedzicki, W. Wieczorek, and M. Marcinek. "Compatibility studies of new Hückel type based electrolytes with electrodes materials," 227th *Electrochemical Society Meeting*, 2015, Chicago, Illinois

G. M. Nolis, "Intercalation materials for secondary batteries," *Warsaw University of Technology, Solid-State Ionics Seminar,* 2013, Warsaw, Poland

G. M. Nolis, F. Omenya, N. A. Chernova, S. Upreti, and M. S. Whittingham. "Structure, defects and thermal stability of delithiated olivine phosphates," *Materials Research Society Fall Meeting and Exhibit,* 2011, Boston, Massachusetts

G. M. Nolis, L. Xu, C. Kim, and J. Cabana, "Optimization of $LiNi_{0.5}Mn_{1.5}O_4$ spinels as high-power cathodes in lithium-ion batteries," *Batteries for Advance Transportation Technologies Seminar,* 2011, Berkeley, California

G. M. Nolis, N. A. Chernova, S. Upreti, and M. S. Whittingham. "Structure, defects and thermal stability of delithiated olivine phosphates," *Batteries for Advance Transportation Technologies Seminar,* 2011, Berkeley, California

G. M. Nolis, N. A. Chernova, S. Upreti, and M. S. Whittingham. "Structure, defects and thermal stability of olivine phase $FePO_4$," *Western New York American Chemical Society Chapter Annual Student Symposia,* 2011, Buffalo, New York

Poster Presentations

G. M. Nolis, J. Bolotnikov and J. Cabana. "Colloidal synthesis: a route towards nanometric cathode materials for multivalent batteries." North American Solid-State Chemistry Conference, 2019, Golden, Colorado.

G. M. Nolis and J. Cabana, "Post-spinel cathode for rechargeable magnesium batteries," *Joint Center for Energy Storage Research All-Hands Meeting*, 2018, Argonne, Illinois

G. M. Nolis, J. Bolotnikov, and J. Cabana, "Mn-O nanocrystal phase space as a function of temperature and oxidizing agent," *American Chemical Society Meeting*, 2017, San Francisco, California

J. Bolotnikov, **G. M. Nolis,** and J. Cabana, "Colloidal synthesis: a route towards nanometric cathode materials for multivalent batteries," *American Chemical Society Meeting*, 2017, San Francisco, California

J. Bolotnikov, **G. M. Nolis,** and J. Cabana, "Colloidal synthesis: a route towards nanometric cathode materials for multivalent batteries," *Joint Center for Energy Storage Research All-Hands Meeting*, 2016, Argonne, Illinois

A. Adil, **G. M. Nolis,** P. Phillips, H. D. Yoo, C. Kim, R. D. Bayliss, R. F. Klie, and J. Cabana, "Understanding divalent cation intercalation into a spinel-type Mn2O4 host framework," *Joint Center for Energy Storage Research All-Hands Meeting*, 2016, Argonne, Illinois

G. M. Nolis, A. Adil, P. Phillips, H. D. Yoo, C. Kim, R. D. Bayliss, R. F. Klie, and J. Cabana, "Understanding divalent cation intercalation into a spinel-type Mn2O4 host framework," *International Meeting on Lithium-ion batteries,* 2016, Chicago, Illinois

G. M. Nolis, L. Xu, C. Kim, and J. Cabana. "Optimization of $LiNi_{0.5}Mn_{1.5}O_4$ spinels as high-power cathodes in lithium-ion batteries," *DOE SULI Poster Presentation Session,* 2011, Berkeley, California

G. M. Nolis, H. Yang, N. A. Chernova, S. Upreti, and M. S. Whittingham. "Structure, defects and thermal stability of delithiated olivine phosphates," *219th Electrochemical Society Meeting,* 2010, Montreal, Quebec, Canada

G. M. Nolis, J. K. Miller, N. A. Chernova, S. Upreti, and M. S. Whittingham. "Energetics and stability of

Fe$_{1-y}$Mn$_y$PO$_4$," *Materials Research Society Fall Meeting and Exhibit,* 2010, Boston,

Massachusetts

Promotional Video

G. M. Nolis and B. Horn. "Give energy to your studies," *Erasmus Mundus Master's of Materials for*

Energy Storage and Conversion, May 2014 (https://www.youtube.com/watch?v=z_-1YKc3ud0)

Awards

Pacesetter Award, *Argonne National Laboratory*

Provost's Award for Graduate Research, *University of Illinois at Chicago*

Provost's Award for Excellence in Undergraduate Research, *Binghamton University*

ERASMUS MUNDUS Scholar, *Université de Picardie Jules Verne*

Harpur College Research Grant, *Binghamton University*

US Department of Energy, Science Undergraduate Laboratory Internship, *Lawrence Berkeley National*

Laboratory

10 APPENDIX

July 1, 2019

Dear Dr. Chen,

I am writing to request permission to use the following material from your publication (*Understanding Electrode Materials of Rechargeable Lithium Batteries via DFT Calculations, 2013, Prog. Nat. Sci.*) in my thesis.
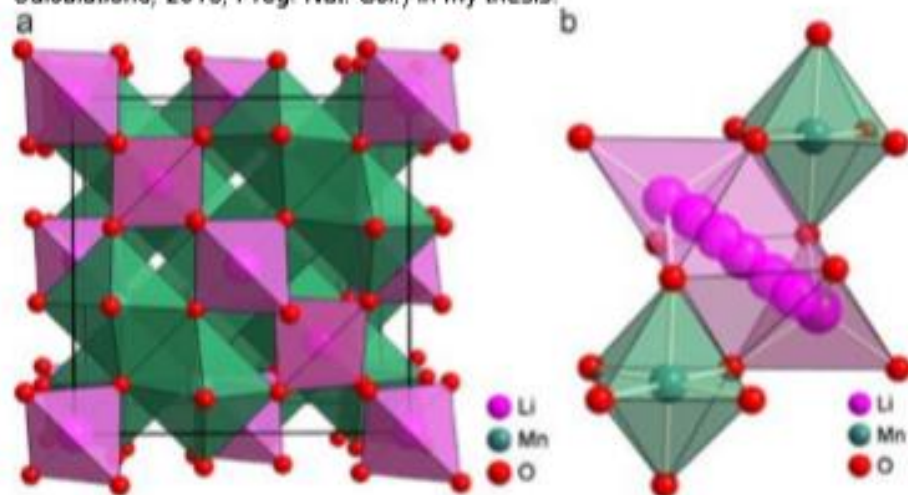
This material will appear as originally published Unless you request otherwise, I will use the conventional style of the Graduate
College of the University of Illinois at Chicago as acknowledgment.
A copy of this letter is included for your records. Thank you for your kind consideration of this request.
Sincerely,

Gene Nolis
University of Illinois at Chicago

_____

The above request is approved.

Approved by: _____ Date: 2 July 2019

ELSEVIER LICENSE
TERMS AND CONDITIONS

Jul 03, 2019

This Agreement between Univ. Illinois at Chicago – Gene Nolis ("You") and Elsevier ("Elsevier") consists of your license details and the terms and conditions provided by Elsevier and Copyright Clearance Center.

License Number	4621481355014
License date	Jul 03, 2019
Licensed Content Publisher	Elsevier
Licensed Content Publication	Progress in Natural Science
Licensed Content Title	Understanding electrode materials of rechargeable lithium batteries via DFT calculations
Licensed Content Author	Tianran Zhang,Daixin Li,Zhanliang Tao,Jun Chen
Licensed Content Date	Jun 1, 2013
Licensed Content Volume	23
Licensed Content Issue	3
Licensed Content Pages	17
Start Page	256
End Page	272
Type of Use	reuse in a thesis/dissertation
Portion	figures/tables/illustrations
Number of figures/tables/illustrations	1
Format	both print and electronic
Are you the author of this Elsevier article?	No
Will you be translating?	No
Original figure numbers	figures 2a and 2b
Title of your thesis/dissertation	Understanding divalent cation intercalation in manganese oxides
Expected completion date	Jul 2019
Estimated size (number of pages)	170
Requestor Location	Univ. Illinois at Chicago 845 W. Taylor St. UIC Chemistry, Room 4500 SES CHICAGO, IL 60607 United States Attn: Univ. Illinois at Chicago
Publisher Tax ID	98-0397604
Total	0.00 USD
Terms and Conditions	

175

July 1, 2019

Dear Dr. Persson,

I am writing to request permission to use the following material from your publication (Spinel compounds as multivalent battery cathodes: a systematic evaluation based on ab initio calculations in Energy and Environmental Science.) in my thesis.
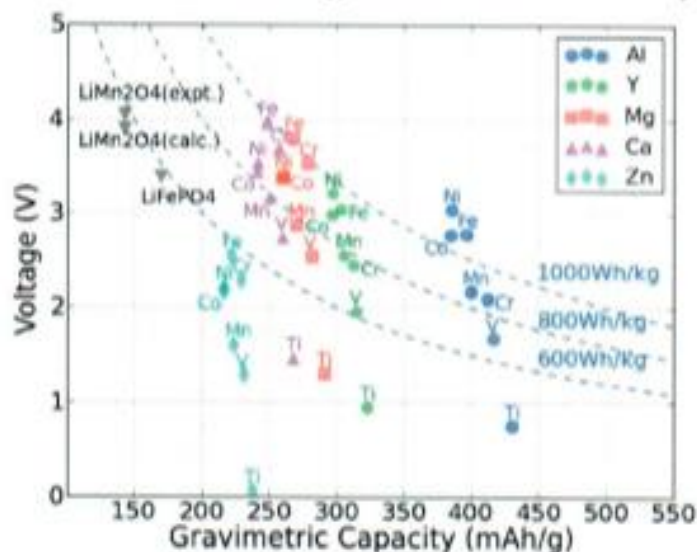
This material will appear as originally published Unless you request otherwise, I will use the conventional style of the Graduate
College of the University of Illinois at Chicago as acknowledgment.
A copy of this letter is included for your records. Thank you for your kind consideration of this request.
Sincerely,

Gene Nolis
University of Illinois at Chicago

The above request is approved.
Approved by _____ Date: July 2, 2019

ACS Publications
Most Trusted. Most Cited. Most Read.

Title: Phase Stability of Post-spinel Compound AMn2O4 (A = Li, Na, or Mg) and Its Application as a Rechargeable Battery Cathode

Author: Chen Ling, Fuminori Mizuno

Publication: Chemistry of Materials

Publisher: American Chemical Society

Date: Aug 1, 2013

Copyright © 2013, American Chemical Society

PERMISSION/LICENSE IS GRANTED FOR YOUR ORDER AT NO CHARGE

BACK

CLOSE WINDOW

UIC

Gene Nolis <gnolis2@uic.edu>

Permission Request Form: Gene Nolis
2 messages

noreply@rsc.org <noreply@rsc.org>   Wed, Jul 3, 2019 at 1:50 PM
To: contracts-copyright@rsc.org
Cc: gnolis2@uic.edu

Name : Gene Nolis
Address :

845 W. Taylor St.
UIC Chemistry, Room 4500 SES

Tel : 6077653417
Fax :
Email : gnolis2@uic.edu

I am preparing the following work for publication:

Article/Chapter Title : Understanding divalent cation intercalation in manganese oxides
Journal/Book Title   : Doctoral dissertation
Editor/Author(s)   : Gene Nolis
Publisher   : University of Illinois at Chicago

I would very much appreciate your permission to use the following material:

Journal/Book Title   : Spinel compounds as multivalent battery cathodes: a systematic evaluation based on ab initio calculations in Energy and Environmental Science
Editor/Author(s)   : Miao Liu,a Ziqin Rong,b Rahul Malik,b Pieremanuele Canepa,b Anubhav Jain,a Gerbrand Cederb and Kristin A. Persson*a
Volume Number   : 8
Year of Publication   : 2015
Description of Material : figure 2
Page(s)   : 966

Any Additional Comments   :

I would like to use figure 2 in my doctoral thesis.

CONTRACTS-COPYRIGHT (shared) <Contracts-Copyright@rsc.org>   Thu, Jul 4, 2019 at 10:20 AM
To: "gnolis2@uic.edu" <gnolis2@uic.edu>

Many thanks for sending the permissions request below. The Royal Society of Chemistry hereby grants permission for the use of the material specified below in your thesis.

Please note that if the material specified below or any part of it appears with credit or acknowledgement to a third party then you must also secure permission from that third party before reproducing that material.

Please ensure that the published article carries a credit to The Royal Society of Chemistry in the following format:

[Original citation] – Reproduced by permission of The Royal Society of Chemistry

and that any electronic version of the work includes a hyperlink to the article on the Royal Society of Chemistry website.

Best wishes,

Chloe Szebrat
Contracts and Copyright Executive
Royal Society of Chemistry
Thomas Graham House
Science Park, Milton Road
Cambridge, CB4 0WF, UK
Tel: +44 (0) 1223 438329

www.rsc.org

[Quoted text hidden]

[Quoted text hidden]

Copyright Clearance Center

RightsLink®

ACS Publications
Most Trusted. Most Cited. Most Read.

Title: Electrochemical Reduction of a Spinel-Type Manganese Oxide Cathode in Aqueous Electrolytes with Ca2 or Zn2

Author: Gene M. Nolis, Abdullah Adil, Hyun Deog Yoo, et al

Publication: The Journal of Physical Chemistry C

Publisher: American Chemical Society

Date: Mar 1, 2018

Copyright © 2018, American Chemical Society

PERMISSION/LICENSE IS GRANTED FOR YOUR ORDER AT NO CHARGE

This type of permission/license, instead of the standard Terms & Conditions, is sent to you because no fee is being charged for your order. Please note the following:

- Permission is granted for your request in both print and electronic formats, and translations.
- If figures and/or tables were requested, they may be adapted or used in part.
- Please print this page for your records and send a copy of it to your publisher/graduate school.
- Appropriate credit for the requested material should be given as follows: "Reprinted (adapted) with permission from (COMPLETE REFERENCE CITATION). Copyright (YEAR) American Chemical Society." Insert appropriate information in place of the capitalized words.
- One-time permission is granted only for the use specified in your request. No additional uses are granted (such as derivative works or other editions). For any other uses, please submit a new request.

BACK   CLOSE WINDOW

Copyright Clearance Center

RightsLink®

Home   Create Account   Help   LIVE CHAT

ACS Publications
Most Trusted. Most Cited. Most Read.

Title:	Control of Size and Composition of Colloidal Nanocrystals of Manganese Oxide
Author:	Gene M. Nolis, Jannie M. Bolotnikov, Jordi Cabana
Publication:	Inorganic Chemistry
Publisher:	American Chemical Society
Date:	Oct 1, 2018

Copyright © 2018, American Chemical Society

PERMISSION/LICENSE IS GRANTED FOR YOUR ORDER AT NO CHARGE

This type of permission/license, instead of the standard Terms & Conditions, is sent to you because no fee is being charged for your order. Please note the following:

- Permission is granted for your request in both print and electronic formats, and translations.
- If figures and/or tables were requested, they may be adapted or used in part.
- Please print this page for your records and send a copy of it to your publisher/graduate school.
- Appropriate credit for the requested material should be given as follows: "Reprinted (adapted) with permission from (COMPLETE REFERENCE CITATION). Copyright (YEAR) American Chemical Society." Insert appropriate information in place of the capitalized words.
- One-time permission is granted only for the use specified in your request. No additional uses are granted (such as derivative works or other editions). For any other uses, please submit a new request.

BACK   CLOSE WINDOW